

DESIGN, CONSTRUCTION, AND OPERATION OF AN  
APPARATUS FOR DETECTING SHORT-LENGTH-SCALE  
DEVIATIONS FROM NEWTONIAN GRAVITY

A DISSERTATION  
SUBMITTED TO THE DEPARTMENT OF PHYSICS  
AND THE COMMITTEE ON GRADUATE STUDIES  
OF STANFORD UNIVERSITY  
IN PARTIAL FULFILLMENT OF THE REQUIREMENTS  
FOR THE DEGREE OF  
DOCTOR OF PHILOSOPHY

David Minot Weld

March 2007

© Copyright by David Minot Weld 2007  
All Rights Reserved

I certify that I have read this dissertation and that, in my opinion, it is fully adequate in scope and quality as a dissertation for the degree of Doctor of Philosophy.

---

Aharon Kapitulnik  
(Principal Adviser)

I certify that I have read this dissertation and that, in my opinion, it is fully adequate in scope and quality as a dissertation for the degree of Doctor of Philosophy.

---

Blas Cabrera

I certify that I have read this dissertation and that, in my opinion, it is fully adequate in scope and quality as a dissertation for the degree of Doctor of Philosophy.

---

Steve Shenker

Approved for the University Committee on Graduate Studies.

# Abstract

A variety of recent theoretical ideas about physics beyond the standard model would, if true, lead to deviations from Newtonian gravity on experimentally accessible length scales. A few of the most important theoretical proposals along these lines are large extra spatial dimensions, string theoretic dilatons and moduli, and scalar particles in hidden supersymmetric sectors. This list is not exhaustive—there are many reasons to investigate the behavior of gravity at small length scales, perhaps the most compelling of which is the fact that it is largely unexplored territory.

To detect or constrain deviations from Newtonian gravity, we have constructed a second-generation cantilever-based probe to directly measure the force between two masses separated by tens of microns. It improves upon the first-generation experiment in several important ways: the area of both test mass and drive mass is substantially increased, time-consuming alignment procedures are eliminated, and the force modulation at the given harmonic is maximized.

The drive mass in our experiment consists of a metal disc with trenches machined in its face. The trenches are filled with a lighter material and covered with gold so that only the density (and not the conductivity or height) is modulated with the proper periodicity. This mass is rotated by a cryogenic helium gas bearing, producing an AC force on a gold test mass. The test mass sits on a silicon nitride cantilever enclosed in a sealed micromachined cavity maintained at low pressure by an integrated cryopump. The cantilever's displacement is recorded by a focused fiber interferometer and correlated with the rotation of the drive mass. This signal can be averaged over many drive mass rotations and used as a direct measurement of the force between the drive mass and the test mass. This measured force can be compared to calculations

of the predicted force signal from various Yukawa-type interactions.

This dissertation will describe the design and construction of the apparatus, present some preliminary data from it, and discuss the prospects for increased precision in constraint or detection of non-Newtonian effects using this probe.

# Acknowledgements

I have many people to thank. Firstly, my dissertation committee. My advisor Aharon Kapitulnik provided constant experimental boldness, motivation in the form of numerous exhortations to serve Mankind, a number of excellent meals, and an inspiring example of a professor with a good and full life outside of physics. All these things were indispensable to me at various times. Blas Cabrera's calmness in the face of all difficulties and his vast storehouse of detailed experimental knowledge are equally invaluable. Steve Shenker taught the best graduate course I took at Stanford and was kind enough to agree to be the third member of my reading committee. Dan Rugar knows more about measuring weak forces than anyone else in the world; it was wonderful to be able to benefit from his advice on many different aspects of the experiment. Michael Peskin agreed on short notice to chair my defense; he told me that the role of a chair is to defend the student against the baser instincts of the other committee members, and then did so ably.

I feel very lucky to have been able to work in the KGB group, an institution that it takes at least five years to start to understand. Although I am not really a condensed matter physicist, I benefited enormously and in many ways from the accumulated KGB experience and atmosphere. Ted Geballe's wisdom and optimism are of course the essential ingredient of the group. Mac Beasley always provided a welcome and cheerful broad perspective on physics and life beyond physics. And Aharon, as mentioned above, supplies a large dose of the energy (and possibly also the entropy) on which the group thrives.

My fellow frogs are the KGB students with whom I worked most closely. Sylvia Smullin's integrity and dedication are unmatched in my experience; as if that weren't

enough, it was Sylvia who invited me on the fateful hiking trip to Big Sur where I met my fiancée. I owe her for that and many other things. John Chiaverini was the patient, cheerfully saturnine (somehow), and all-around excellent leader of the first KGB gravity project. The always-calm Andy Geraci and I were for a long while the Last of the Frogs; a bond not to be taken lightly. And Jing Xia made the most of his brief tenure on the gravity experiment, fabricating our cantilevers with amazing rapidity and precision.

The Lubyanka headquarters of this California KGB, at least during my time at Stanford, was McCullough 001, and its Dzerzhinsky was unquestionably Mike Rozler. In addition to providing a lot of badly needed experimental advice, Mike taught me how to play hockey and poker (sort of) and tell soviet jokes, elucidated with many examples the groundbreaking political concept of micro-sanction known as “the ban,”<sup>1</sup> and listened to me complain about graduate school over coffee rather more times than could reasonably be required of him. I suspect we may have had 1000 cups of coffee together. Mike is also the co-inventor (with me) of a new cryptographic language of limited applicability but dazzling sophistication. Paul SanGiorgio (also up there on the coffee-meter) came to the group at a moment of crisis after the departure of several key free agents, and totally rejuvenated it. Paul helps out his fellow KGBers way more than any other group member. His good cheer and group spirit are both electronic *and* supersonic. I am confident that one day we will realize his dream of mandatory crimson KGB jumpsuits. Craig Howald was the grand old man of KGB when I arrived, and the repository of much of the group’s experimental knowledge; he held this position with distinction and élan. Alan Fang, who pwnz the bots and succeeded Craig on the STM, has a similarly oracular disposition. Alan gave me a lot of good advice on subjects ranging from FLCL to what he would call <technical stuff>. Rafael Dinner is the most reasonable member of KGB, and a reliable source of interesting conversation and experimental ideas. Myles Steiner’s friendly and level-headed presence was another integral component of the KGB atmosphere; happily, his spirit

---

<sup>1</sup>It is perhaps worth noting here that the 2006 Nobel peace prize was awarded to Muhammad Yunus and the Grameen bank for pioneering the use of “micro-loans.” Scandalously, Mike’s path-breaking contributions to micro-scale politics and economics went uncited in Yunus’ acceptance speech.

lives on in the enormous Myles/Canada shrine of the shielded room (may the harpies deoculate any future defilers thereof). Serge Reymond makes excellent fondue and knows how to enjoy life. Yana Matsushita, a fellow user of the sacred thermal evaporator, did me one very important favor among others by helping me take a SQUID scan of the brass we used for the drive mass. Nadya Mason and I only overlapped for a little while, but she very kindly helped me out with some much-needed advice when I was applying for jobs. Nick Breznay, Zhanybek Alpichshev, and Liz Schemm are the three tiniest students in the lab as of my departure; their particular mixture of sure-handedness, urbanity and Khlebnikovianism reassures me that the future of KGB is bright. Bob Hammond, Gert Koster, Jeong Huh, Walter Siemons, William Jo, and all the guys in Moore cheerfully provided lots of great advice on deposition techniques and other experimental matters, and kindly lent us many indispensable bits of equipment. Jeroen Huijben, one of several excellent visiting Dutchmen, was a particular standout for his friendliness and his piratical nature. Leonid Litvak provided KGB with a very useful and exhaustively annotated list of world cultural resources.

I have heard from visitors that Stanford is unusually good at promoting intra-university cooperation and interaction among lab groups. I can easily believe it. Many groups here were very helpful to the gravity project in general and to me in particular. I would like to express particular gratitude to the students and PIs in the groups of Kam Moler, David Goldhaber-Gordon, Ian Fisher, Blas Cabrera, Hari Manoharan, Giorgio Gratta, Mark Kasevich, and David Miller for many loans of good equipment and gifts of good advice. I must also thank here some people I never met: Janet Tate, Sue Felch, and George Hess. They were some of the scientists who helped build and run the beautiful fused quartz gas bearing probe; I was lucky to be able to make use of their excellent craftsmanship.

The technical staff at Stanford are a hugely important part of any experimentalist's work; I in particular have a lot to thank them for. I spent many enjoyable hours with Tim Brand and Ryan at the Ginzton crystal shop. Their dedication and inventiveness made impossible fabrication tasks merely difficult, and Tim's advice on more important matters than physics was always excellent. There would be more happy

graduate students at Stanford (but perhaps fewer happy crystal shop proprietors) if more of us dropped by the northwest corner of Ginzton every few days. Karlheinz Merkle, foreman of the Varian machine shop, can make almost anything. Karlheinz, Mehmet, John, and the other machinists are always willing to give advice, answer dumb questions, and help find solutions to seemingly insurmountable machining problems. Their patience is as admirable as their technical virtuosity. Tom Carver, at the Ginzton microfab facility, may know more than anyone on earth about metal deposition. His advice too was always good and always readily given. Mike Hennessy and Jim Perales (our neighbors in the HEPL endstation for many years) were also very helpful on many occasions, in particular with advice on vacuum technology and assistance with experimental construction projects. It is my strong belief that guys like Tim, Karlheinz, Tom, and Mike are the foundation and the *sine qua non* of a great research university.

The administrative staff, of course, are the people without whom none of this would get done. The KGB group was blessed with great admins during my time at Stanford. Judy Clark loved NASCAR in a classy way, making her unique among humans on earth. Cyndi Mata ably replaced her, and then gave the KGB group a spy on the inside when she became the GLAM accounting associate. Angela Edwards now carries on their tradition of cheerful competence. The physics department admins in Varian were also a joy to work with. Dawn was (and is) always ready to talk baseball, Kathleen kindly endured my attempts to speak Chinese, and Maria was unfailingly friendly and ready with endless advice on negotiating the bureaucratic hurdles facing an aspirant to graduation. Droni Chiu, a fellow Cantabrigian, helped me out in many ways, most concretely once when she and Maria noticed that some of my direct-deposited paycheck was missing and helped me reclaim it. Mark Gibson handled McCullough receiving and many other issues with unfailing good cheer; it was and is always a pleasure to bump into Mark. And Stewart Kramer, the building manager in Varian, ameliorates the many aches and pains of that no-longer-young building with the aid of an unusually philosophical disposition.

I would also like to thank a few important inanimate or incorporeal entities that helped shape my time at Stanford. I have a great fondness for the NRC thermal

evaporator in McCullough, despite its several betrayals. I spent many long days early in grad school sitting at its side boiling gold “like some Inca king,” as John would say, and since then I have used it for a surprisingly large and disparate group of Frogstar-related tasks. I believe I have replaced, repaired, or refurbished every single part of it except for the foreline valve, so look for that to go soon. The sturdy and easily anthropomorphized Welch belt-drive pumps that run both the main experiment and that evaporator continue to amaze me with their gurgly longevity. And of course the gas bearing probe herself, whom I inherited, is an inspiring marvel of engineering. Finally, the Dave Roberts Boston Red Sox and the Troy Brown New England Patriots have made it very easy to be an expatriate New England sports fan for the past several years; I am grateful to them as well.

I have had a string of excellent roommates since high school. The people I had the good fortune to live with during graduate school are, in order of appearance: Sam Waldman, Puneet Batra, Etienne Benson, Haider Shirazi, Noah Helman, Jerel Davis, Edward Fenster, Melanie Robinson, Steve Gertsch, and Paco Robinson-Gertsch. All of them made my time here much more fun. I love having roommates. Sam (my longest-serving cohabitor), Puneet, and Noah were both fellow physicists *and* roommates; take away any of those three guys and my experience at Stanford would be very different and much less good. Other people on campus and in the area who significantly bettered my lot in life include such luminaries as Onn Brandman, Peter Garran, Seth Sternglanz, Caitlin Shaw Henig, Joe Hennawi, Vlatko Balic, Josh Henig, Anna Chai, Mike Crawford, Relly Brandman, Edith Chan, Haley Steele, Jerry Smith, Sarah Heim, Heather Wax, Alicia Kavelaars, Christian Bauer, Sameer Bhalaria, Randy Grow, Jim Freeman, Shayna Cunningham, Raphael de Balmann, Chana Palmer, Caolionn O’Connell, Eli Grigsby, Rachel Sommovilla, Katherine Rochlin, Gerry Slean, Chienlan Hsu, Jadd Cheng, Ginny Buckingham, the Netscape hockey players, and all Sports Day participants. I am also grateful to many pre-Californian friends, most of whom who seemed to believe I would indeed one day graduate from school, or at least were discreet about believing the opposite. Some among them are Sean Westmoreland, Patrick Keefe, Jonathan Kohler, Noah Freeman, Matthew Lubin, Marty Ouimet, Andrew Bonney, Spencer Dickinson, Nat Kreamer, and Michael

Feferman. If I recorded here what I owed each of the people mentioned in this paragraph, this acknowledgements section would balloon even farther beyond the limits of sense and good taste than it already has, so I must content myself with these somewhat barren enumerative thanks and the hope that many good things will happen to all of them.

I have the best family in the world, which is nice for me but too bad for all of you who by implication don't. When I was about nine, my mother explained to me the cause of washboarding in dirt roads, and my father caught a flying popsicle for me at a football game. Aunties Anna and Sandy have the bright eyes and darting souls of true scientists. Along with me, the exclusive DEMQF club comprises my sisters and brother Ethel, Mary, Quentin, and Fran. During the darkest days of my time in graduate school, I received seven packages in one week from different family members who had been mysteriously alerted to my plight. It was the turning point of my long graduate career.

Finally, and not unrelatedly, endless thanks are due to Sara, the small sputnik with whom I have traveled through the last seven years and hope to travel through the next seventy. Her understanding, humor and ferocity are without compare; I find them indispensable to civilized existence.

# Contents

<b>Abstract</b>	<b>iv</b>
<b>Acknowledgements</b>	<b>vi</b>
<b>1 Introduction</b>	<b>1</b>
<b>2 Motivation and Existing Bounds</b>	<b>3</b>
2.1 Motivation . . . . .	3
2.2 Existing bounds . . . . .	4
<b>3 Experimental Apparatus</b>	<b>9</b>
3.1 Design Considerations . . . . .	9
3.2 Overview of the Apparatus . . . . .	11
3.3 Drive Mass Actuation . . . . .	12
3.3.1 Advantages of the Gas Bearing . . . . .	14
3.3.2 Disadvantages of the Gas Bearing . . . . .	17
3.3.3 Flow meters and flow controllers . . . . .	18
3.3.4 The Optical Encoder . . . . .	19
3.3.5 Feedback Control of the Spin Frequency . . . . .	26
3.3.6 Temperature Control of the Gas Bearing . . . . .	27
3.4 Drive Masses . . . . .	30
3.4.1 Selection of Drive Mass Materials . . . . .	30
3.4.2 Drive Mass Fabrication . . . . .	34
3.4.3 Drive Mass Characteristics . . . . .	40

3.5	Test masses . . . . .	42
3.5.1	Test Mass Fabrication . . . . .	43
3.5.2	Test Mass Manipulation and Attachment . . . . .	47
3.6	Cantilevers . . . . .	49
3.6.1	Cantilever Design . . . . .	50
3.6.2	Cantilever Wafer Fabrication . . . . .	51
3.6.3	Cantilever Displacement Detection . . . . .	52
3.6.4	Integrated Cantilever Vacuum System . . . . .	54
3.6.5	Radiation Pressure Damping of the Cantilevers . . . . .	57
3.7	Force Detection . . . . .	68
3.7.1	Data Acquisition . . . . .	68
<b>4</b>	<b>Data Analysis</b>	<b>70</b>
4.1	Data Analysis . . . . .	70
4.1.1	Averaging procedure . . . . .	70
4.1.2	Phase determination . . . . .	72
<b>5</b>	<b>Uncertainties, Backgrounds, and Noise</b>	<b>76</b>
5.1	Experimental Uncertainties . . . . .	76
5.1.1	Uncertainties in mass separation distance . . . . .	76
5.1.2	Uncertainties in the force calibration . . . . .	77
5.1.3	Uncertainties in the mass dimensions and densities . . . . .	78
5.1.4	Uncertainties in the determination of $\alpha$ . . . . .	78
5.2	Sources of Background Forces . . . . .	79
5.2.1	Non-magnetic forces . . . . .	80
5.2.2	Magnetic forces . . . . .	80
5.3	Sources of Noise . . . . .	83
5.3.1	Thermal noise . . . . .	83
5.3.2	Vibrational noise . . . . .	84
5.3.3	Other noise sources . . . . .	87

<b>6</b>	<b>Results</b>	<b>89</b>
6.1	Zeroth Cooldown . . . . .	89
6.2	First Cooldown . . . . .	90
6.3	Second cooldown . . . . .	92
6.3.1	General properties of data . . . . .	99
6.4	Limits on non-Newtonian interactions . . . . .	99
<b>7</b>	<b>Conclusions</b>	<b>102</b>
<b>A</b>	<b>Other Experimental Approaches</b>	<b>103</b>
<b>B</b>	<b>Thermal Analysis of the Cantilevers</b>	<b>105</b>
<b>C</b>	<b>Care and Feeding of the Probe</b>	<b>111</b>
<b>D</b>	<b>Cryogenic Setup</b>	<b>115</b>
<b>E</b>	<b>Future Work</b>	<b>120</b>
<b>F</b>	<b>Catalog of Data Files</b>	<b>123</b>
	<b>Bibliography</b>	<b>127</b>

# List of Tables

5.1	Estimated uncertainties in the mass separation . . . . .	77
5.2	Estimated uncertainties in the force calibration . . . . .	78
5.3	Estimated uncertainties in properties of the masses . . . . .	78
5.4	Estimated uncertainties in calculation of $\alpha$ . . . . .	79
B.1	Unit definitions for thermal calculations . . . . .	106
F.1	Catalog of important off-resonance data files . . . . .	125
F.2	Catalog of important on-resonance data files . . . . .	126

# List of Figures

2.1	Theoretical predictions and some previous experimental results in $\alpha$ - $\lambda$ parameter space . . . . .	8
3.1	Schematic of the experiment . . . . .	12
3.2	Assembled probe . . . . .	13
3.3	Schematic of the gas bearing . . . . .	14
3.4	Photograph of the gas bearing . . . . .	15
3.5	Typical encoder signal . . . . .	21
3.6	Determination of the distance between the masses . . . . .	24
3.7	Adjusting flows for $z$ -distance control. . . . .	25
3.8	Rotor frequency feedback loop . . . . .	26
3.9	Rotor frequency feedback in action . . . . .	28
3.10	Drive mass fabrication . . . . .	30
3.11	Linear contraction of selected drive mass materials . . . . .	32
3.12	Brass drive mass with and without a shield . . . . .	40
3.13	Profilometer scans of drive masses . . . . .	42
3.14	SQUID scan of brass drive mass . . . . .	43
3.15	Test mass fabrication . . . . .	44
3.16	Test mass weighing . . . . .	46
3.17	Photographs of the cantilevers . . . . .	50
3.18	Photographs of cantilever wafer . . . . .	51
3.19	Fiber interferometer . . . . .	53
3.20	Microfabricated cryopump . . . . .	56
3.21	Cryopump effectiveness . . . . .	58

3.22	Difficulty of controlling spin frequency . . . . .	59
3.23	Radiation pressure damping setup . . . . .	63
3.24	Measuring the cantilever’s spring constant . . . . .	66
3.25	Radiation pressure damping results . . . . .	67
4.1	Encoder-mass phase alignment setup . . . . .	72
4.2	Reading data plots. . . . .	73
4.3	Procedure for determining phase of measured force. . . . .	75
5.1	Schematic of possible magnetic coupling mechanism . . . . .	81
5.2	Noise data from runs under different conditions . . . . .	84
5.3	Improving noise in data runs . . . . .	87
6.1	Data from the first few experimental runs . . . . .	91
6.2	Data from multiple runs taken during the November cooldown. . . . .	94
6.3	Raw data from a single run . . . . .	96
6.4	Averaged data from a single run . . . . .	97
6.5	Data from multiple runs at different $z$ -positions . . . . .	98
6.6	Limits in $\alpha - -\lambda$ space . . . . .	101
B.1	Theory and simulation of cantilever thermal response . . . . .	107
B.2	Simulation of thermal response of a cantilever with glue layer . . . . .	109

# Chapter 1

## Introduction

The study of gravity is hardly a new field. Theories of the mechanism of the gravitational interaction have been around at least since Aristotle, and in the hands of Galileo, Newton, and Einstein, gravitation has played a major part in at least two scientific revolutions. Although it is arguably the most immediately perceptible of the four fundamental forces, the force of gravity is still the least well understood, especially from a quantum mechanical point of view. Quantum mechanically, the Newtonian description of gravity is expected to break down at very small distances. Recent theories (such as the idea that “large extra dimensions” to spacetime might exist [1, 2]) suggest the possibility that this breakdown could occur at experimentally accessible length scales. These open questions regarding the nature of gravity are the motivation for the present work, which is an experimental investigation of short-distance gravitation.

One of several mysterious properties of gravity is its extreme weakness relative to other forces. The assertion that gravity is very weak tends initially to strike people as odd, given that we spend our lives under its omnipresent tug and that gravity is responsible for ordering the visible universe on astronomical scales. However, the *relative* weakness of gravity is easily demonstrated by the commonplace fact that a small refrigerator magnet can pick up a paperclip. To perform this feat, the magnet’s upward force, which is of course electromagnetic in nature, must be so much stronger than gravity that it can overcome the downward gravitational force of an entire planet.

The fact that gravity plays the dominant role in the binding of solar systems and galaxies is entirely due to the fact that there seems to be only one sign of gravitational charge (positive mass), and opposite-sign charges of all other forces cancel out at large scales.

This extreme weakness makes gravity both difficult to explain and difficult to measure. In order to make the best possible measurements of gravity at a given length scale, one would like to get two masses very near each other and measure the force between them very precisely. Several years ago, our group designed and constructed just such an experiment (called Frogland), which used micromechanical cantilevers to sensitively measure the force between two small gold masses [3]. This experiment provided the best limits on non-Newtonian interactions at length scales around 10  $\mu\text{m}$ . The lessons from the operation of that probe have now been applied to the design of a next-generation experiment with the same goal: precision measurement of gravity or gravity-like forces at short distances. The new probe incorporates large-area masses, rotary actuation, and innovative optical detection and control of custom-built cantilevers. It is this new experiment, called Frogstar, that is the subject of this dissertation.

The new probe uses a cryogenic helium gas bearing for actuation of a disc-shaped metallic drive mass. Force signals due to the motion of the drive mass are converted in to displacement signals by test-mass-bearing cantilevers inside micro-cryopumped vacuum cavities set in the lid of the bearing. The motion of the cantilevers is detected and controlled with laser light in a fiber-optic interferometer. The entire experiment is operated at or near the boiling point of liquid helium to reduce thermal noise. We have designed and built the Frogstar probe, and used it to take some preliminary data. The bounds on non-Newtonian interactions extracted from those data are already comparable to the best existing limits, and are better in some regimes. When it is operated at the thermal noise limit, this probe has the capability to expand the boundaries of known phase space by two orders of magnitude.

# Chapter 2

## Motivation and Existing Bounds

### 2.1 Motivation

In spite of the success of the Newtonian and Einsteinian theories of the gravitational interaction, gravity remains the most mysterious of the four fundamental forces. No renormalizable quantum field theory of gravity has been found, and gravity plays a central role in two of the greatest outstanding questions in physics: the cosmological constant problem [4, 5] and the gauge hierarchy problem [6]. It is generally believed that a classical description of gravity must fail at or before the Planck length  $\sqrt{\hbar G/c^3}$  (about  $10^{-35}$  meters). However, many of the proposed solutions to these problems predict modifications to Newtonian gravity at much longer length scales, up to 1 millimeter. A few of the most important theoretical proposals along these lines are “large” extra spatial dimensions [1, 2], string theoretic dilatons and moduli [7], and scalar particles in “hidden” supersymmetric sectors [6]. Additionally, it has been pointed out [5] that the observed value of the cosmological constant, when expressed as a length scale  $(\hbar c/\Lambda)^{1/4}$ , is about  $100 \mu\text{m}$ . A useful and complete discussion of theories of physics beyond the standard model that are relevant to our experiments is presented in chapter 2 of reference [8]. There are many reasons to investigate the behavior of gravity at small length scales, perhaps the most compelling of which is the fact that it is largely unexplored territory.

Until recently, Newtonian gravity had only been experimentally tested down to

millimeter length scales; the extreme weakness of gravity that poses such a puzzle for theorists is an equally daunting problem for experimentalists. In recent years, however, there have been several experiments designed to detect or constrain deviations from Newtonian gravity below 1 millimeter [3, 9, 10, 11, 12]. Typically, the results of such experiments have been reported as bounds on a hypothetical Yukawa coupling added to the Newtonian potential. This modified potential takes the form

$$V = -\frac{Gm_1m_2}{r} \left(1 + \alpha e^{-r/\lambda}\right), \quad (2.1)$$

where  $\alpha$  represents the strength (relative to gravity) of the Yukawa coupling, and  $\lambda$  represents its length scale. Such Yukawa couplings arise naturally from interactions due to exotic massive scalar particles; tests of gravity at or near the length scale of any extra dimensions would also see corrections to Newtonian gravity of this form [2]. The finite force sensitivity of any measurement will (if no non-Newtonian effects are detected) result in an upper bound for the strength of any such effect, which can be expressed as an upper bound for  $\alpha$ . Any given experiment of this type has a geometry-dependent range of  $\lambda$  to which it is most sensitive. Thus, each experiment carves out an area of “ $\alpha$ - $\lambda$ ” space within which it would be able to detect deviations from Newtonian gravity.

## 2.2 Existing bounds

### The Cavendish experiment

The difficulty of measuring the force of gravity between two lab-scale masses has prompted a large number of ingenious experimental solutions. The earliest and most well-known experiment investigating gravitational forces at short range was the one performed by Henry Cavendish in 1798 using an apparatus designed by the Reverend John Michell [13]. The apparatus consisted of a long-period torsional oscillator which was excited into oscillation by the motion of external weights. The stated aim of this experiment was to measure the density of the earth; it achieved this by determining the ratio between the force exerted by the earth on the test mass and the force

exerted by the drive mass on the test mass (the radius of the earth was already fairly well known at that time).<sup>1</sup> Almost incidentally, the results also furnished a measurement of Newton's universal constant  $G$  which connects gravitational force to mass and distance, although Cavendish did not initially emphasize this aspect. The paper presenting his results (Ref. [13]), a model for future efforts, is written in a wonderfully conversational style and includes a frank and practical discussion of the many possible sources of error that must be addressed in measurements of weak forces. At the very end of the paper, Cavendish addresses the possibility of a deviation from normal gravitational attraction at short distances:

*Another objection, perhaps, may be made to these experiments, namely, that it is uncertain whether, in these small distances, the force of gravity follows exactly the same law as in greater distances. There is no reason, however, to think that any irregularity of this kind takes place, until the bodies come within the action of what is called the attraction of cohesion,<sup>2</sup> and which seems to extend only to very minute distances. With a view to see whether the result could be affected by this attraction, I made the 9th, 10th, 11th, and 15th experiments, in which the balls were made to rest as close to the sides of the case as they could; but there is no difference to be depended on, between the results under that circumstance, and when the balls are placed in any other part of the case. (Ref. [13], page 522)*

This brief addendum represents the first attempt at detecting or constraining deviations from Newtonian gravity at short length scales. Modern experiments have achieved better force sensitivity and smaller separation distances, but the essential character of the measurements remains unchanged from that of the simple test reported above.

---

<sup>1</sup>Cavendish measured the mean density to be 5.48 times that of water, very close to the currently accepted value of 5.52. This is higher than the mean density of any other planet in our solar system.

<sup>2</sup>Cavendish is presumably referring here to Van der Waals forces.

### Dependence of bounds on experimental geometry

Each experiment is, by nature of its geometry, most sensitive to deviations from Newtonian gravity at a particular length scale  $\lambda_o$ , corresponding very roughly to the face-to-face separation  $d$  between drive mass and test mass. This is a result of the exponential  $\alpha$ - $\lambda$  parametrization of the deviations that was discussed above. Non-Newtonian effects at a length scale  $\lambda$  much smaller than  $d$  will lead to forces that are exponentially suppressed by a factor of  $\sim e^{\lambda/d}$  and are thus undetectable. Effects at a length scale much *greater* than the dimensions of the masses will of course be unsuppressed, but will in general be better constrained by experiments with larger masses that integrate more of the exponentially decaying force. Each experiment, then, if it does not observe any inverse-square-law deviations, takes a “bite” out of the  $\alpha$ - $\lambda$  phase space that has a “knee”<sup>3</sup> at a particular value of  $\lambda$ . Variations in the absolute force sensitivity of an experiment and the area and density of the masses have the effect of changing the detectable  $\alpha$ , which corresponds to moving the exclusion curve up or down in  $\alpha$ - $\lambda$  space.

In general, the border of “known phase space” in a log-log  $\alpha$ - $\lambda$  plot in the neighborhood of our experiment trends up and to the left with an average slope of around 4 (see figure 2.1). This can probably be explained by a simple dimensional argument. Most experiments in this area measure the force between two masses of similar size  $r$ , separated by a distance that is also roughly equal to  $r$ . In such a situation, the Newtonian force  $F_N = Gm_1m_2/r^2$  scales quadratically with mass  $m$  and as the inverse square of distance  $r$ . Since  $m \simeq \rho r^3$ , the overall scaling of the Newtonian force is quartic in the length scale  $r$  of the experiment. Smaller-scale experiments, then, though they are able to probe interesting lower- $\lambda$  areas of  $\alpha$ - $\lambda$  space, are limited in their  $\alpha$ -sensitivity by the steep quartic scaling of the force they are trying to constrain or measure. This is the likely reason for the fact that the exclusion curves of many very different experiments at different length scales all seem to fall on a line with a slope near 4.

---

<sup>3</sup>“And then, to mix a metaphor, the hand of fate stepped in....”

### Existing bounds from recent experiments

Since the eighteenth-century work of Cavendish, several different experimental techniques have been used to measure short-distance gravity. Here I will mention a few of the most recent and notable experiments in this field.

At very long length scales ( $\lambda \simeq 10^8$  meters), lunar ranging to the retroreflectors left behind by the Apollo astronauts has provided quite sensitive constraints on the strength  $\alpha$  of any non-inverse-square-law force [14]. Several of the experiments at length scales significantly below this make use of torsional oscillators similar to that used by Cavendish. One example is the experiment done in the mid-eighties at the University of California Irvine [15], which used copper masses at a minimum separation of 5 cm to measure Newtonian gravity to about one part in  $10^4$ . Similar experiments were done at length scales around 5 mm by Mitrofanov and Ponomareva in Moscow [16]. The University of Washington has produced good constraints on non-Newtonian effects across a broad range of length scales  $\lambda$  near  $10^{-3}$  meters using torsion pendula that contain arrays of holes and are driven by similarly shaped drive masses. For one example of this ongoing work, see Ref. [9].

At even lower length scales, micromechanical cantilever-type oscillators are typically used as force sensors instead of torsion pendula. The experiment done at the University of Colorado [10] uses a silicon cantilever as a drive mass to excite a micromachined torsional oscillator. The length scale of this experiment, set by the face-to-face mass separation, is around  $100 \mu\text{m}$ . At very short length scales, the best limits on non-Newtonian interactions typically come from experiments investigating the behavior of the Casimir force. One such experiment done by Lamoreaux [17, 12] measured the Casimir force between a small plate and a sphere (a geometry which minimizes alignment difficulty) and resulted in good  $\alpha$ - $\lambda$  bounds below about  $1 \mu\text{m}$ . More recent work using an atomic force microscope cantilever has confirmed the expected value of the Casimir force to within 1%, resulting in the most stringent current bounds on non-Newtonian interactions between 10 and  $100 \text{ nm}$  [18].

The ‘‘Frogland’’ experiment [3, 19] was the first short-length-scale gravity experiment constructed by our group at Stanford, and it is discussed at great and fascinating length in references [20] and [8]. That experiment measures the force between a small

gold test mass mounted on a microcantilever and a gold-and-silicon comb-patterned drive mass that is oscillated by a piezoelectric bimorph. The face-to-face separation of the masses is around  $30 \mu\text{m}$ ; as a result, the experiment is most sensitive near that theoretically interesting range of  $\lambda$  and already provided the best limits on non-Newtonian interaction there after its first published run.

Figure 2.1 presents a picture of the current state of exploration of the micron-to-millimeter range of  $\alpha$ - $\lambda$  space and of the areas where theory predicts deviations.

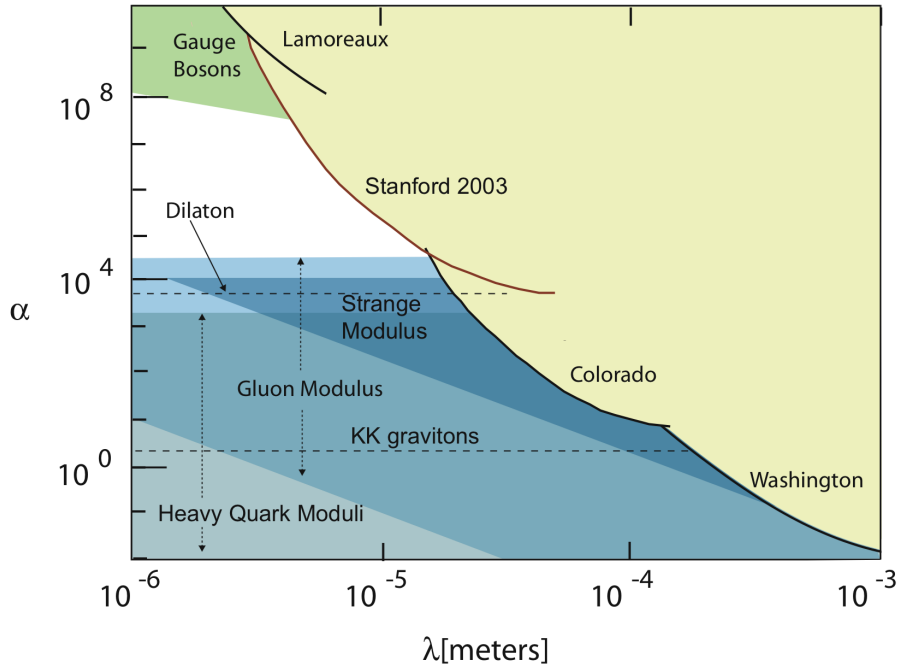


Figure 2.1: Previous experimental results (solid lines) and theoretical predictions shown in the micron-to-millimeter region of  $\alpha$ - $\lambda$  space. The area to the upper right of the experimental lines (from Refs. [3, 9, 10, 12]) shows where Yukawa-type deviations from Newtonian gravity have been excluded. Dashed lines show roughly the predictions for the dilaton[7] and the first Kaluza-Klein mode of two extra dimensions as described in Ref. [2]. Shaded regions to the left of the experimental lines show predictions for moduli and gauge bosons from Ref. [21].

# Chapter 3

## Experimental Apparatus

The work described in this dissertation is a second-generation gravity experiment which we informally refer to as “Frogstar.” We conceived and designed it based on our experience constructing and operating the “Frogland” experiment,<sup>1</sup> our group’s first probe of gravity at short distances.[3, 19] Starting a new experiment gave us the freedom to consider many different possible approaches to the problem of measuring weak mass-dependent forces between small objects. In this chapter I will outline the experimental goals which informed our design decisions and then give a detailed description of the experimental apparatus that we ultimately settled upon, constructed, and ran.

### 3.1 Design Considerations

The basic idea of our experiment is similar to that of the famous experiment by Cavendish [13] in the sense that we seek to measure or constrain a mass-dependent force between two close-together objects, neither one of which is a planet. To maximize the signal from Newtonian or Yukawa forces, one would like to use masses that are as dense and as close together as possible (the latter requirement being of particular importance for detection of exponentially decaying Yukawa forces). The

---

<sup>1</sup>The origins of this name are lost in the mists of time, but it may have arisen as a mash-up of the KamLAND neutrino detector with an animal the author has long admired. The second experiment was named “Frogstar” both by analogy and as an homage to the late Douglas Adams.

Newtonian interaction between sub-millimeter-scale masses is so weak that DC detection of the force is basically impossible; AC techniques must therefore be used to maximize the signal to noise ratio. The need for AC detection leads to the additional requirement that the separation between the two masses can be varied periodically. There are thus three basic requirements when designing an experiment of this type:

1. The density of the masses should be as large as possible.
2. The separation between the masses should be as small as possible.
3. The experimenter should be able to modulate the separation between the masses in a controlled way.

The first requirement can be easily met by making the masses out of gold, tungsten, or some similarly dense substance. The need for small separation suggests a parallel-plate geometry, since that concentrates the mass as close together as possible, maximizing any mass-dependent force. The requirement that the masses be able to be easily moved relative to each other in a way that does not produce spurious forces is the trickiest, especially if the experiment is to be done at low temperatures to minimize thermal noise. In general, there are many possible experimental schemes that are reasonably consistent with optimization of these three factors. Some of the ones we considered for this experiment are listed in appendix A.

After considering all of these schemes, we decided on a setup that uses a helium gas bearing as a drive mass actuator and mounts the test masses on cantilevers inside the lid of the gas bearing. A rough schematic is presented in figure 3.1, and the setup is discussed in detail later in this chapter.

This scheme has several advantages. First, the rotary geometry gives effectively infinite travel range of the drive mass. In the Frogland experiment, the lateral size of the drive mass was limited by the small range of motion of the piezoelectric bimorph at low temperatures. The rotary gas bearing thus allows us to use much larger area drive masses, leading to a large increase in the expected signal from any mass-dependent forces. Another advantage of this setup is that it allows us to pattern many drive mass periods in the disc, leading to a large separation between the angular frequency of the

drive mass  $\omega_{\text{dm}}$  and the resonant frequency of the cantilever  $\omega_0$ . This frequency separation cuts down on the need for vibration isolation and minimizes non-gravitational crosstalk between the drive mass and the test mass. Rotary actuation also maximizes the force that goes into the chosen harmonic; in the Frogland experiment, because of the relatively low-amplitude sinusoidal drive mass actuation, as much as 80% of the force was put into harmonics other than the one matched with the cantilever’s resonant frequency. Another very significant upside to the present scheme is the fact that it is essentially self-aligning. One of the most difficult and time-consuming aspects of the Frogland experiment was the need to align two small masses very precisely at low temperatures; the elimination of this step greatly simplifies our experimental procedure. A final practical advantage of using this experimental scheme is that we had access to a low temperature helium gas bearing, precisely machined out of fused silica by the Cabrera group here at Stanford. This bearing was originally used to precisely determine the flux quantization in superconducting niobium; we were very lucky to be able to adapt it for the purpose of measuring gravity [22, 23, 24, 25, 26].

## 3.2 Overview of the Apparatus

Figure 3.1 presents a schematic, and figure 3.2 a photograph, of the experimental apparatus. It is fundamentally a Cavendish-type [13] experiment in the sense that its purpose is to directly measure the force between two masses. A cryogenic helium gas bearing [24] is used to rotate a disc containing a “drive mass” pattern of alternating density under a small “test mass” mounted on a micromachined cantilever. Any mass-dependent force between the two will produce an AC force on the test mass, and consequently an AC displacement of the cantilever. This displacement is read out with a laser interferometer, and the position of the drive mass is simultaneously recorded using a purpose-built optical encoder [22]. The displacement is then averaged over many cycles and converted to a force using measured properties of the cantilever. This AC “lock-in” type measurement enables significant noise rejection and allows us to operate on resonance to take advantage of the cantilever’s high quality factor. Conceptually, then, the experiment can be divided into five parts: the drive mass

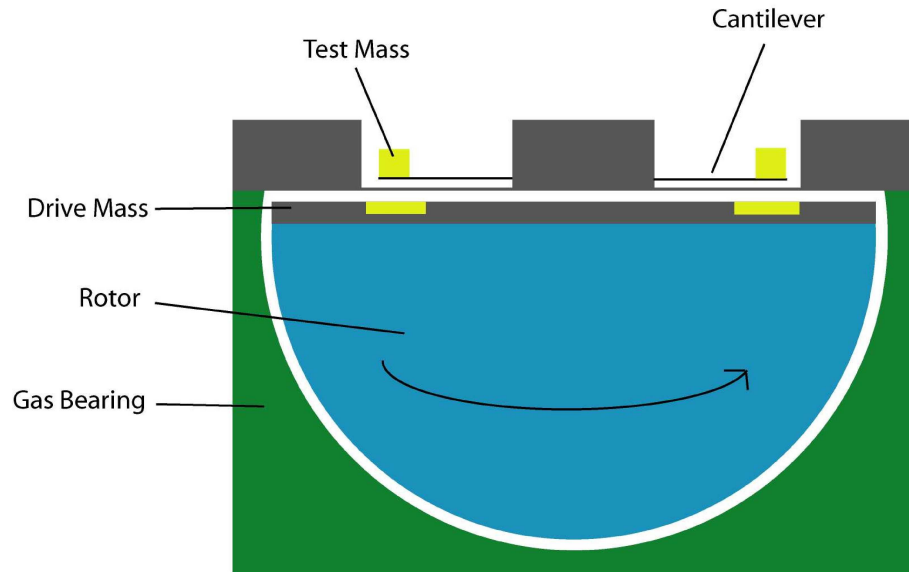


Figure 3.1: A schematic drawing (not to scale) of the heart of the experimental apparatus.

actuation system, the drive mass, the test mass, the cantilever, and the force detection system. The remainder of this chapter will be devoted to discussing each of these subsystems in detail.

### 3.3 Drive Mass Actuation

The mass actuation system (schematically depicted in Figure 3.3) consists of a rotary helium gas bearing, which is a two-inch-diameter hemispherical cavity with six gas inlets—two for the bearing and four for spin control. A hemispherical rotor sits within the cavity; it can be levitated and continuously rotated by adjusting the flow of gas among the inlets. Computer-interfaced mass flow controllers are combined with the spin-speed detection system (discussed below) into a feedback loop to keep the rotor spinning at a set frequency. At low temperature, the gas flow is laminar in all of the bearing except for the spin-up channels and the exhaust [22]. The wafer containing the cantilevers is clamped under the flat of the hemispherical cavity, and the drive

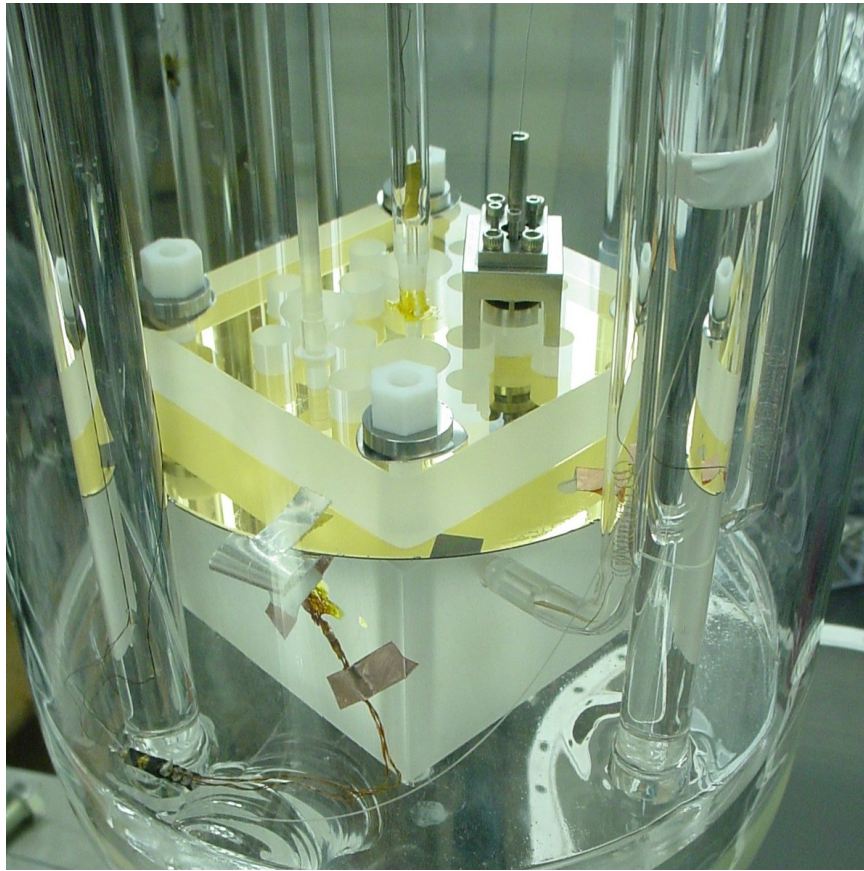


Figure 3.2: A photograph of the assembled probe. The gold-coated cantilever wafer is visible between the lid and housing of the gas bearing. The stainless steel structure protruding from the lid is the fiber holder that maintains the alignment of the interferometer. The optical fiber is barely visible emerging from the top of that structure. The fiber bundle for the encoder and two of the gas bearing inlets are also visible here.

mass is mounted on the flat of the rotor. Both the cavity and the rotor are machined from single blocks of fused silica (used for its very low thermal expansion). Figure 3.4 shows a photograph of the disassembled gas bearing. This type of motor/bearing assembly has many advantages for this experiment; we discuss some of them below.

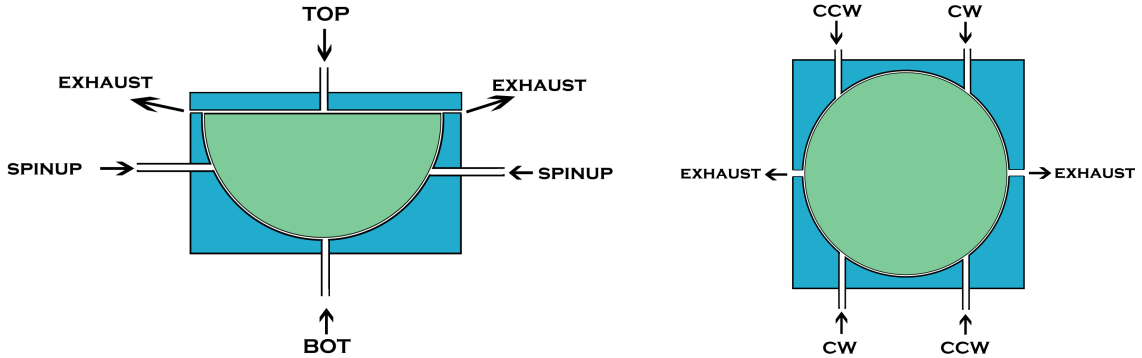


Figure 3.3: A schematic drawing of the helium gas bearing, showing the six gas inlet ports. **Left:** Side view. **Right:** Top view. The ports labeled “TOP” and “BOT” provide the gas that the rotor floats on. The clockwise and counter-clockwise spin-up ports are labeled “CW” and “CCW” respectively. Exhaust ports are also indicated.

### 3.3.1 Advantages of the Gas Bearing

The most practical of the advantages of the cryogenic fused quartz helium gas bearing was that it already existed, having been built and used by the Cabrera group here at Stanford to measure the Cooper pair mass in niobium [22, 23, 24, 25, 26]. That measurement measured the zeros of the London moment flux through a superconducting niobium ring deposited around the equator of the slightly-more-than-hemispherical rotor.<sup>2</sup> Obviously, such an experiment required extremely precise and stable control and readout of the rotor’s rotation frequency—it was the fact that the proposed Frogstar experiment shared these requirements that led us to investigate the possibility of using this probe for actuation of our drive mass.

Two other important virtues of the bearing are its tight distance tolerances and its stiffness; run in the correct regime, it can be substantially stiffer than a bearing made of steel. In an experiment designed to detect mass-dependent forces (particularly exponentially decaying Yukawa forces) it is critically important to know and control exactly how far apart the test mass and drive mass are. In the configuration of our

<sup>2</sup>The rotors that were actually used in this experiment could not be located, despite much diligent searching. Luckily, one “backup” rotor was found, with no niobium ring or encoder pattern, and a slightly smaller diameter. That one proved to work quite well in the bearing.

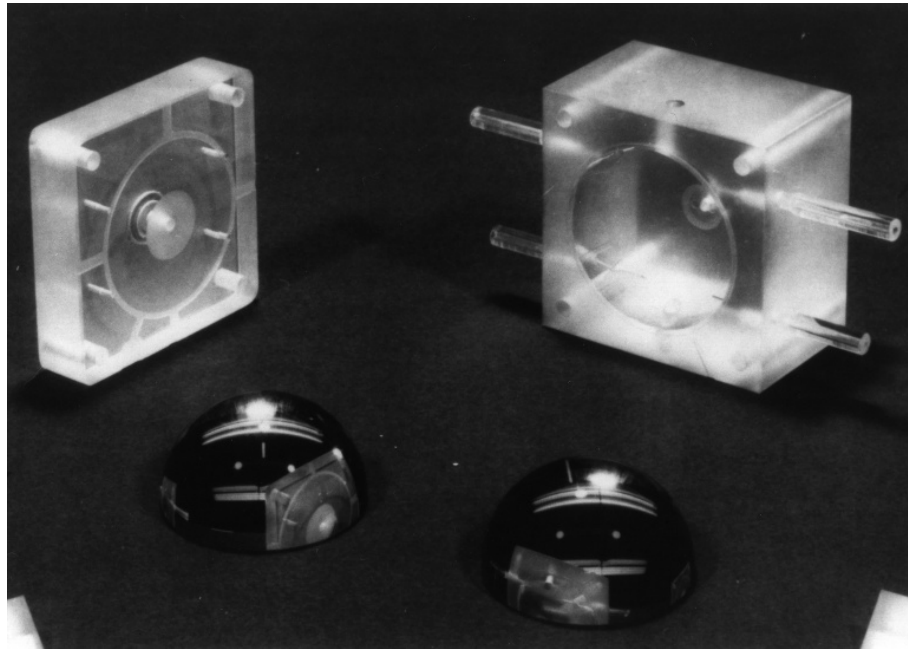


Figure 3.4: A beautiful photograph of the helium gas bearing, taken by Don Davidson (its fabricator). On the left is the lid of the bearing, which contains the top gas inlet port. In the foreground are two rotors. At right is the bearing housing, featuring a hemispherical cavity with four spin gas inlet lines and the bottom gas inlet port.

experiment, that corresponds to knowing and controlling the separation between the top flat surface of the rotor and the bottom surface of the bearing’s lid (which in our case is a silicon cantilever wafer). The gas bearing performs very well in this regard, in that if the gas flows are correctly adjusted it strongly resists any attempts to compress the gas layer between rotor and lid below about  $12\ \mu\text{m}$  in thickness.<sup>3</sup> This is due to the fact that pressure is inversely proportional to the thickness of this gas layer, assuming a constant mass flow rate. The restoring force thus diverges as the separation gets very small, which results in a high stiffness in the relevant direction. This stiffness means that not only is it relatively immune to noise-producing “rattling” displacements, it also is capable of robust and repeatable operation in a distance regime that is

<sup>3</sup>We have not done systematic studies of this “critical separation”; those are left for a future Frogstar operator. But in general our experience operating the bearing agrees with the more extensive experience of the Cabrera group, in that we both have found it possible to reduce this distance to a minimum of about  $12\ \mu\text{m}$  but difficult to reduce it further.

very interesting from the point of view of theoretical predictions of deviations from Newtonian gravity (see figure 2.1).

Other advantages of using the cryogenic helium gas bearing as a drive mass actuator stem from what it is not. It is totally non-magnetic, a characteristic which distinguishes it from most of the low-temperature electric motors we considered using. Since the command signals that control drive mass motion are sent in the form of slowly-varying gas flows rather than AC voltages, it is also completely immune to in-probe electrical cross-talk, a common annoyance we faced in the Frogland experiment. Because of its unique system of gaseous lubrication and actuation, the bearing can be easily operated at any temperature above the boiling point of liquid helium; other types of bearings tend to run into serious lubrication problems at very low temperatures.

The rotary geometry of the gas bearing is also important for our experiment. By far the most important benefit of rotary actuation is that its large range of motion (compared to linear piezoelectric actuators) allows us to use very large area masses in a parallel-plate configuration. Since the force due to any mass-dependent interaction scales with the area of the masses, this apparatus has an excellent intrinsic sensitivity to such interactions. This factor is responsible for the bulk of the improvement in thermal-noise-limited sensitivity that prompted the construction of this experiment.

Finally, the self-aligning nature of the gas bearing greatly simplifies the experimental procedure. When building and running the Frogland experiment, at least half of our time and effort was spent characterizing and adjusting the relative position of the drive mass and the test mass. In the Frogstar experiment, the tight clearances and stiffness of the bearing (and, secondarily, the large extent of the drive mass trenches in the radial direction) make it auto-aligning— if the bearing is spinning, the the drive masses are guaranteed to be directly below the test masses. This auto-alignment is more than an experimental convenience; it enables long averaging times and thus improved force sensitivity.

### 3.3.2 Disadvantages of the Gas Bearing

No other practically achievable drive mass actuation method has all the advantages discussed above. However, the unique nature of the cryogenic gas bearing did pose some important experimental challenges not posed by other actuation methods. The most important of these was the fact that it requires gas to operate, while the cantilevers require vacuum to maintain a high quality factor and thus a good force sensitivity. This problem was solved by hermetically sealing the cantilevers inside a cryopumped cavity, as discussed in section 3.6.4.

Another potential downside of the gas bearing is that it can produce substantial vibrational noise. This noise is important because of the limitations on possible vibrational isolation imposed by our experimental geometry. Indeed, vibrational noise (and not thermal noise) is currently the limiting factor that determines the performance of the experiment. However, the portion of this noise that is due to the gas flow in the bearing can be drastically reduced by reducing the gas flows in the top and bottom bearing inlets. This reduction is presumably due to increasing laminarity of the flow at lower rates. The experiments characterizing this dependence on flow rate will be discussed in more detail in chapter 4. This disadvantage, then, appears to be surmountable.

The final difficulty posed by the use of the gas bearing for actuation is mainly practical: the bearing and most of its support structure are made of fused silica and glass, and are thus somewhat fragile. In particular, the gas lines leading into the bearing are easy to break when assembling or disassembling the bearing. Luckily, they are also relatively easy to fix. A low-thermal-expansion epoxy made for sealing the quartz bulbs of halogen lamps<sup>4</sup> can be used to re-set the lines; it survives being cooled down to 4 degrees. The mechanical support structure of the bearing, which consists of a thick quartz disc supported by four long quartz rods, also looks as if it is very fragile. This does not however seem to be the case; a chip on the bottom of the disc, which can still be seen, was the only result of a long-ago implosion of the copper-to-glass Housekeeper seal on the inner vacuum can. There is thus cause for

---

<sup>4</sup>Resbond 940LE, made by Cotronics Corp., Brooklyn NY

considerable confidence in the structural integrity of the bearing supports.

### 3.3.3 Flow meters and flow controllers

As depicted in figure 3.3, there are four independent gas lines running into the probe: one each for the top and bottom bearing inlets, and two others that are each split and fed to the two clockwise and two counter-clockwise spin-up inlets. The flow rate of the helium gas in each of these four lines can be independently adjusted to optimize bearing performance and control spin frequency. Our method of controlling the spin of the bearing with gas flow was somewhat different from that used by the Cabrera group in the  $h/m$  experiments. In our initial cooldown, the flow in all four gas lines was regulated by manually adjustable needle valves in series with rotameter-type flowmeters. These flowmeters measure the flow of gas by feeding it through a gradually widening vertical tube containing one or more small balls which are borne aloft by the flow—the height of the balls is linearly proportional to the flow rate. This setup proved capable of spinning the gas bearing at room temperature and liquid helium temperature. However, since the flow rate is set by providing a static flow impedance with the needle valve, it is affected by temperature fluctuations in the room and pressure fluctuations in the gas supply. The inability to automatically adjust the impedance in response to these and other fluctuations means that a graduate student must be inserted into any feedback loop designed to keep the spin frequency of the rotor constant. Even if the very finest graduate students are used, this tends to severely compromise the reliability and performance of the feedback. See figure 3.22 for an example of inadequate PID response using this technique. Section 3.6.5 discusses the adverse consequences of poor frequency control.

In order to solve this problem, we replaced the four needle-valve controlled flowmeters with digital mass flow controllers.<sup>5</sup> These instruments measure the mass flow (rather than the volume flow) of gas using a thermal technique, and contain internal

---

<sup>5</sup>Sierra Instruments, model 840.

feedback systems that are capable of dynamically adjusting their impedance to maintain a given flow rate. The desired flow rate can be set with an externally applied analog voltage. In combination with a GPIB-to-analog interface,<sup>6</sup> these remotely adjustable flow controllers can be used as part of a digital feedback loop to maintain any desired spin frequency. The structure and operation of that feedback loop is discussed below in section 3.3.5, after a description of another important element in it.

### 3.3.4 The Optical Encoder

Accurately and precisely controlling the rotor spin frequency, of course, requires accurate and precise measurement of that frequency. This measurement is done using a purpose-built optical encoder, which was part of the original experiment done with this apparatus by the Cabrera group [22]. The optical encoder is used to measure the angular frequency and position of the drive mass so that it can be phase-correlated with the force signal observed by the interferometer.

#### Structure and uses of the optical encoder

The encoder is roughly diagrammed in figure 3.8. It consists of a fiber-optic bundle displacement sensor [27], fit into the lid of the gas bearing, that is aimed at the gold pattern deposited at the edge of the drive mass (see Figure 3.10 for a good photograph of this pattern). The displacement sensor comprises a bundle of several thousand fiber optic light guides running from the drive mass up the length of the probe and out of the dewar. The light guides are randomly split into two bunches after they exit the dewar— one bunch leads to the incandescent lamp that serves as a light source for the sensor, and the other leads to a buffered and amplified photodetector. The light guide splitting, the lamp, and the photodiode are all inside the Fotonix sensor instrument.<sup>7</sup> That instrument outputs a voltage proportional to the power impinging on the photodetector.

The signal from the fiber bundle sensor can be used to measure three quantities:

---

<sup>6</sup>Stanford Research Systems, model SR245.

<sup>7</sup>MTI KD320 Fotonix Sensor.

the angular frequency, angular phase, and vertical position of the drive mass rotor. The angular frequency and phase determine the force applied to the cantilever, and the vertical position of the rotor sets the distance between test mass and drive mass—knowledge of all three of these parameters is thus crucial to the experiment. Here follows a description of the method by which they can be measured with this sensor.

### **Measuring the rotational frequency and phase**

The light from the lamp travels down half of the light guides into the probe and strikes the drive mass. The reflected light re-enters the fiber bundle. The portion of the light that enters light guides leading to the photodetector then produces a signal proportional to its power. This power will vary with the reflectivity of the drive mass surface; since the encoder pattern consists of a series of alternating high and low reflectivity areas, rotation of the rotor will modulate the measured reflected power and produce a signal like that depicted in figure 3.5. This modulated signal is fed to a data acquisition board,<sup>8</sup> read into a computer, and analyzed using a zero-crossing technique to precisely determine the rotational frequency and phase. In this technique, the time between zero-crossings is measured for an integer number of revolutions, in order to minimize the effects of non-uniformity in the encoder pattern. The sense of rotation (clockwise or counter-clockwise) can also be determined, due to the asymmetry of the encoder pattern.

### **Measuring the mass separation**

In addition to depending on the reflectivity, the measured reflected power also depends in a non-monotonic but well-characterized way on the absolute distance between the end of the fiber bundle and the reflecting surface. This distance-dependence is not an interferometric effect; it is simply due to the geometry of the light path. When the fiber bundle is butted up against the drive mass, all the light from the lamp is reflected directly back into light guides that lead back to the lamp, and the photodetector measures zero reflected power. Similarly, when the fiber bundle is

---

<sup>8</sup>National Instruments PCI-6036E.

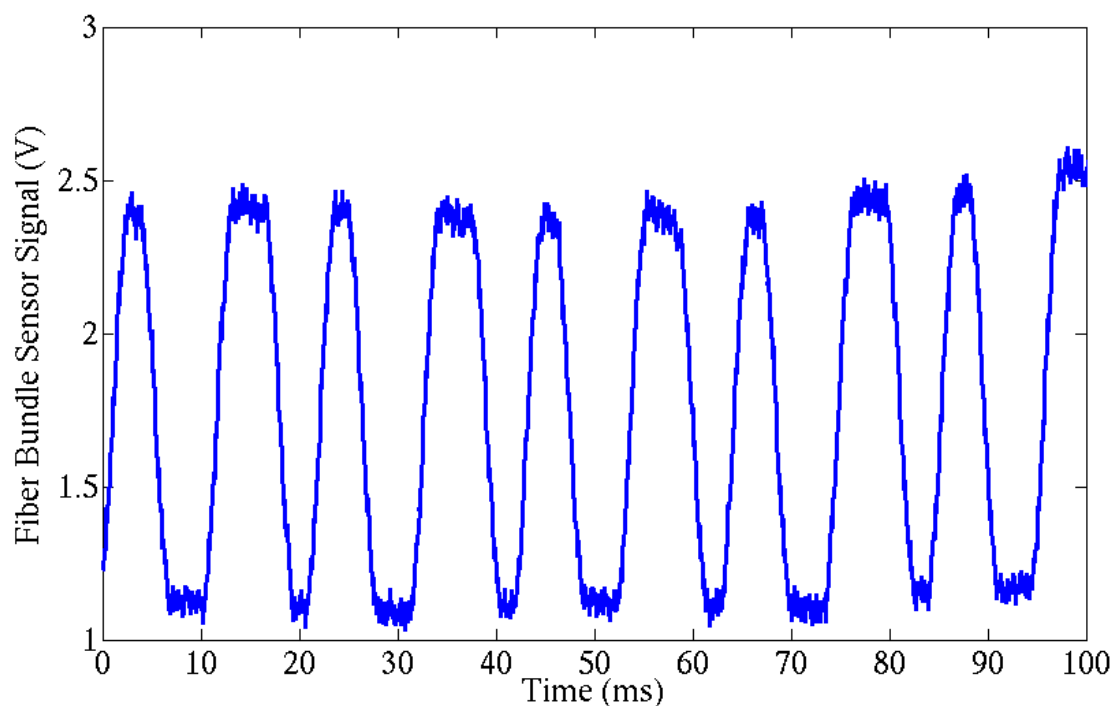


Figure 3.5: A typical signal from the optical encoder. This signal was produced by the rotor spinning clockwise at about 5 Hz.

withdrawn a great distance from the drive mass, almost all of the light produced by the lamp diverges and does not reflect back into the fiber at all; this again results in nearly zero reflected power. At intermediate distances, however, a substantial fraction of the light is reflected into light guides that lead to the photodetector. The signal from the fiber bundle sensor will thus be maximized at some finite drive mass-fiber distance  $d_{\max}$  (typically a few millimeters). If the actual distance between drive mass and fiber is set to a value of about half of  $d_{\max}$ , the photodetector signal will be very sensitive to small variations in separation. This position sensitivity allows the fiber bundle sensor to be used to detect the vertical position of the rotor. In practice, the sensor is amazingly sensitive—displacements of a few tenths of a micron are easy to detect.

To measure the distance between the drive mass and the cantilever wafer, then, one can simply compare the encoder signal when the rotor is spinning to the encoder

signal when the rotor is pressed against the lid of the bearing. The difference between these two signals, converted to a distance, is the separation between the bottom of the wafer and the top of the drive mass when the rotor is spinning. Since the distance between the cantilever and the bottom of the wafer is fixed by construction and known,<sup>9</sup> this provides an exact and absolute measurement of the all-important face-to-face separation between the drive and test masses. There are, however, some other important details one must take into account in order to achieve a precise and accurate measurement of the separation. These factors, and the exact procedure for measuring the separation, are discussed below. I give quite a detailed description here, not because these issues are particularly interesting, but because of the great importance of this measurement to the experiment.

Since different elements of the encoder pattern can have slightly different apparent reflectivities,<sup>10</sup> it is important to be sure to compare two measurements of the same single gold patch for the distance determination. In order to do this, the following procedure is used. The gas flow to the top bearing inlet is turned off while the rotor is spinning slowly. If the other gas flows are high enough, this results in the rotor gently coming to a stop, and being pressed up against the lid of the bearing by the force of the gas from the bottom bearing inlet and the spin inlets. Since the fiber bundle running down into the probe is image-preserving, it is possible to disconnect the Fotonix sensor, look directly down the fiber bundle (with a flashlight) and clearly see what part of the pattern the fiber bundle is looking at. The effect is that of having a small round window directly in the top of the bearing housing. If the fiber bundle is looking at either a non-gold-covered part of the pattern or the border of a gold patch, the top flow is turned back on and then off again after several tens of seconds. This pulsed flow causes the bearing to rotate further and then stop again. This procedure can be repeated until the bearing comes to rest in such a way that the area imaged

---

<sup>9</sup>The base of the cantilever is 14  $\mu\text{m}$  above the shield, the shield is 4.4  $\mu\text{m}$  thick, and the mass-loaded cantilever typically droops 4  $\mu\text{m}$  due to Earth's gravity.

<sup>10</sup>This differing reflectivity is believed to be largely due to imperfectly uniform deposition of the gold, since only the *maxima* of the encoder signal vary significantly in this way. If this effect were due to bending of the drive mass or a variation in roughness, one would expect the minima (the non-gold areas) to vary in the same way. If the drive mass is rotated during the gold deposition, this effect is greatly reduced.

by the fiber bundle is entirely within one gold patch in the encoder pattern (ideally one of the *large* gold patches, since the small patches are barely wider than the fiber bundle). Achieving successful alignment in this way generally takes between 5 and 50 tries.

At this point, a calibration of distance versus encoder signal is performed. First, the Fotonix sensor is rigidly re-attached to the fiber bundle with a custom-made collet. An *xyz* micrometer attached to the top of the dewar can then be used to push on the collet and precisely translate the whole fiber bundle in the  $z$ -direction. The feedthrough in the top of the probe that the fiber bundle goes through must allow the bundle to slide freely for this to work— a not-very-tight Wilson seal with plenty of vacuum grease on the o-ring was found to provide adequately low resistance to translation without introducing any noticeable leaks. Since the micrometer provides a calibrated displacement, this setup can then be used to take readings of the voltage output by the Fotonix sensor versus the  $z$ -distance between the fiber bundle and the gold patch on the drive mass. After several such readings have been taken, the micrometer is readjusted so that the fiber bundle is in the middle of the range of calibration positions at which readings were taken. Because of the calibration, the dependence of sensor voltage on displacement is known in the neighborhood of this point. A downward displacement of the rotor will have the same effect on the separation, and thus on the encoder signal, as an upward displacement of the fiber bundle. While the voltage from the Fotonix sensor is being constantly recorded, the top gas flow is then turned on again, and the rotor moves down to an equilibrium  $z$ -position and begins to spin. The sensor signal changes from a constant value to a waveform characteristic of spinning, like that shown in figure 3.5. Since the signal is being constantly recorded, it is simple to determine which gold patch the fiber bundle was pointing at while the rotor was stopped, and to sample the spinning signal only when that same patch is passing underneath the fiber bundle. This procedure corresponds to measuring the value of every 20th maximum in the spinning signal, since there are 20 gold patches around the circumference of the drive mass. The difference in voltage between the spinning value and the still value of this maximum in the signal can then be combined with the calibration of voltage versus separation to

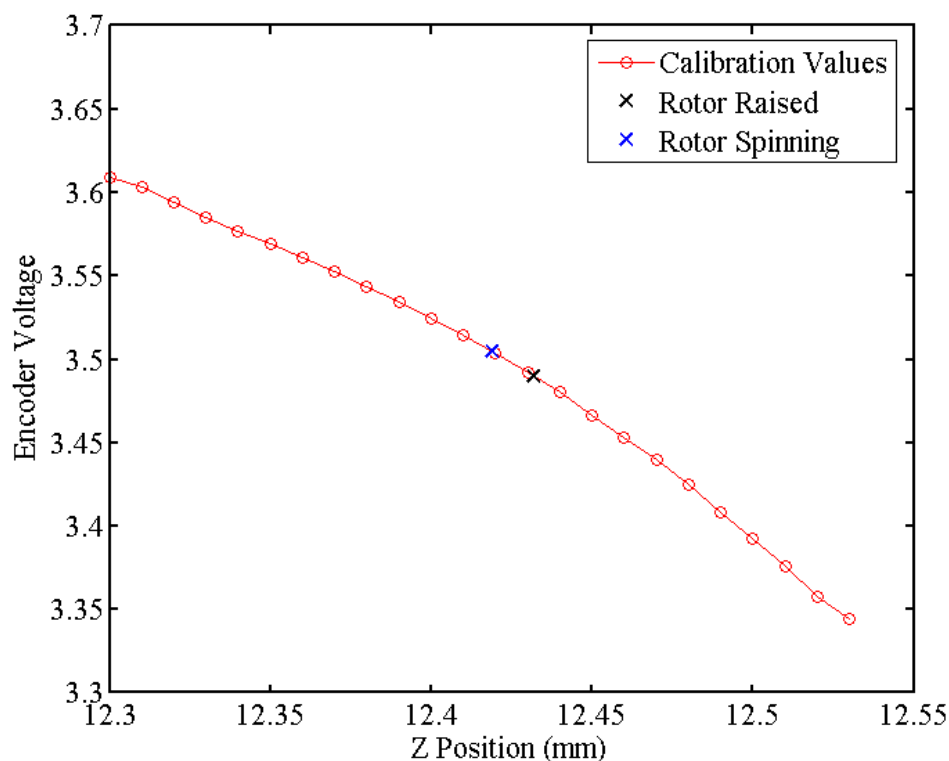


Figure 3.6: Graph used to determine the equilibrium distance between the top of the housing and the rotor when it is spinning. The calibration values were taken by moving the fiber bundle with a micrometer. The “rotor raised” reading was taken with the rotor pressed against the lid of the bearing and the fiber bundle aimed at a particular piece of the gold pattern. The “rotor spinning” reading was taken while the bundle was pointing at that same gold patch and the rotor was rotating. The distance between housing and rotor thus determined is  $12.8 \mu\text{m}$  for this particular measurement.

provide an absolute measurement of the separation between the cantilever wafer and the drive mass while the rotor is spinning. A graph of such a  $z$ -distance measurement is shown in figure 3.6. The separation, if the gas flows are properly adjusted, can easily be made as low as  $12 \mu\text{m}$  (sometimes even lower). This wafer-to-drive-mass separation corresponds to about a  $29\text{-}\mu\text{m}$  face-to-face separation between the test mass and the drive mass. The  $z$ -distance when the rotor is spinning does depend slightly on the

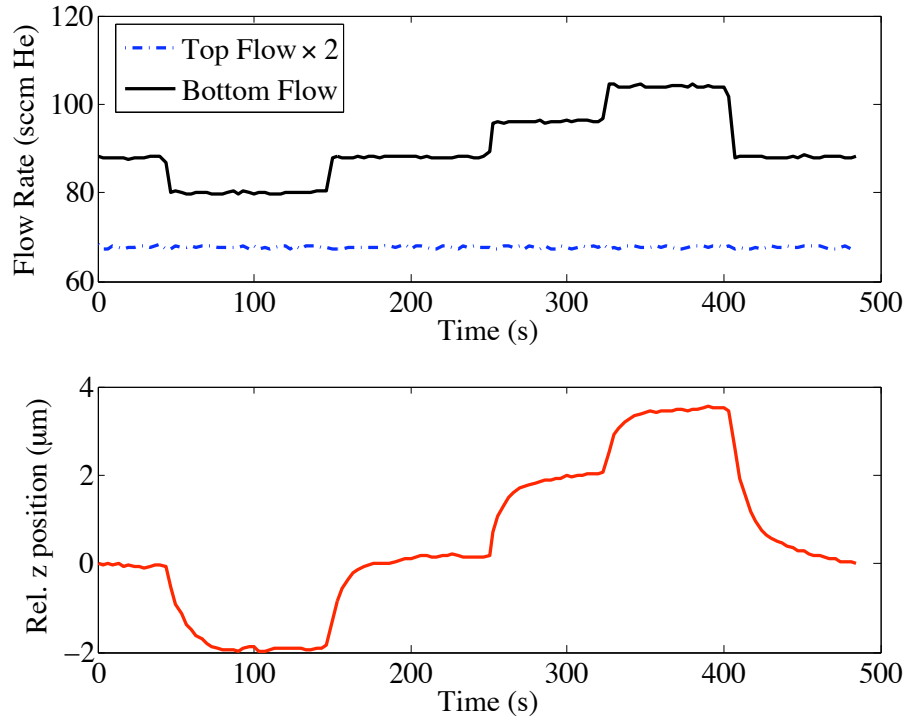


Figure 3.7: This graph demonstrates the ability to control the  $z$ -separation over a small range by adjusting the flows in the top and bottom inlets of the gas bearing. **Top:** Flow rates versus time, for the top and bottom inlets of the gas bearing. **Bottom:**  $z$ -position versus time, as measured by the calibrated optical encoder. An overall linear drift, due to thermal contraction of the long rigid fiber, has been removed from the  $z$ -position data.

flow rates in the gas bearing (particularly at the top and bottom inlets). This fact gives the experimenter the ability to move the rotor up and down in the cavity by a few microns while it is spinning, just by adjusting the flow controllers. Of course, the flow rates are coupled to other aspects of the experiment, particularly noise. That and geometrical effects constrain the range of possible  $z$ -distance modulation. The largest distance by which we have raised or lowered the rotor while spinning is about  $5 \mu\text{m}$ . An example of this technique is shown in figure 3.7.

### 3.3.5 Feedback Control of the Spin Frequency

The fiber-bundle-based encoder described above allows very accurate and precise measurement of the rotational frequency of the drive mass. In order for the experiment to have the maximum possible sensitivity to mass-dependent forces, however, that rotational frequency must also be very tightly *controlled* (not just very well *measured*).<sup>11</sup> Achievement of an adequate level of frequency control requires a feedback loop. A frequency control feedback loop has therefore been implemented, and is

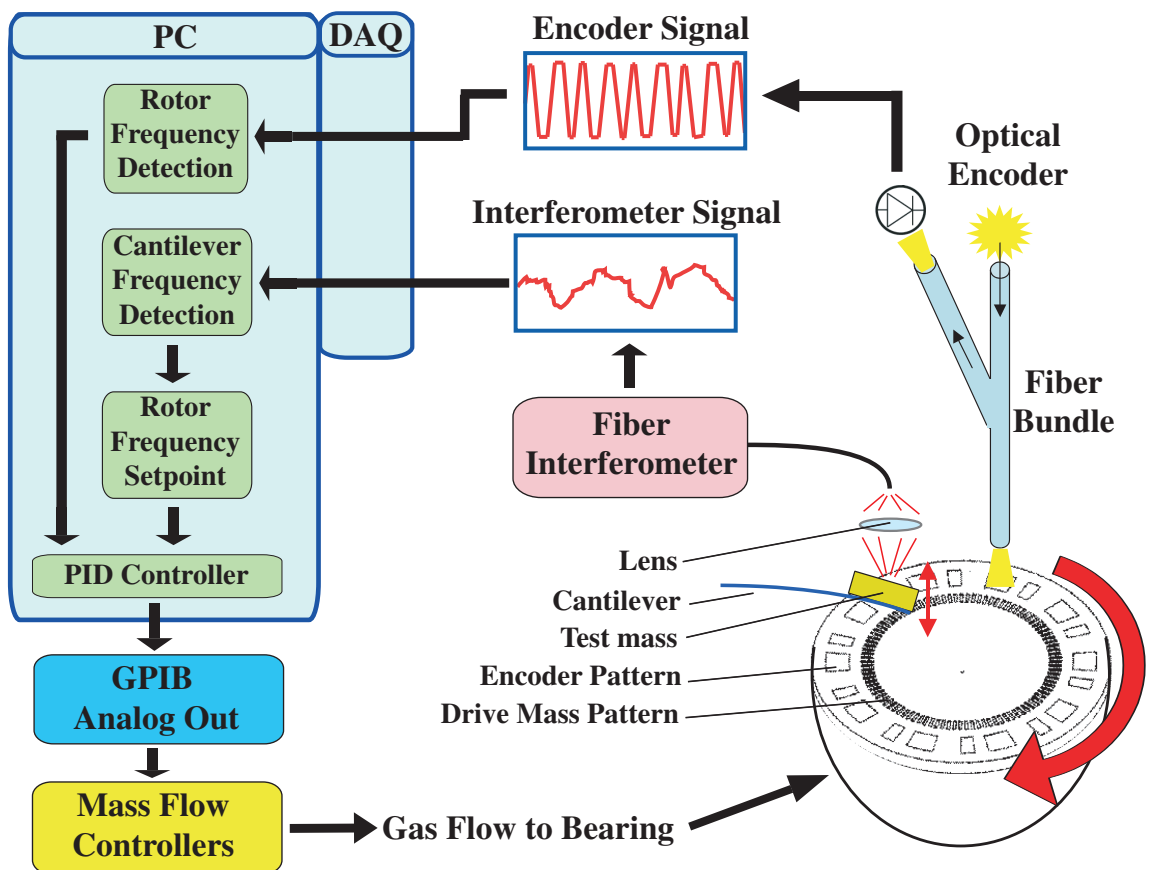


Figure 3.8: A diagram of the feedback loop that controls the spin frequency of the rotor. The system is described in the text.

<sup>11</sup>The reasons for this (chief among them the requirement that the cantilever be excited on its very narrow resonance) are discussed in section 3.6.5 and graphically illustrated in figure 3.22.

schematically represented in figure 3.8. A data acquisition (DAQ) board attached to a PC acquires two signals simultaneously: the signal from the optical encoder (section 3.3.4), and the signal from the fiber interferometer which is proportional to the cantilever's displacement (section 3.6.3). The DAQ board is controlled, and both signals are acquired, by a custom-built MATLAB script with a rudimentary graphical user interface (see figure 3.9 for a screenshot). The script calls subroutines that determine both the rotational frequency of the rotor (essentially by measuring the average time between zero-crossings of the mean-subtracted encoder signal for an integer number of complete rotations) and the resonant frequency of the cantilever (by fitting the fourier-transformed resonance peak with a Lorentzian). These values are both sent to a digital PID<sup>12</sup> controller, which is implemented in another subroutine in the same MATLAB script. The rotor frequency provides the process variable for the PID loop, and the cantilever frequency (divided by 100) provides the setpoint. The proportional, integral, and differential gains are set by the user using the graphical user interface—once the loop is tuned it is not typically necessary to adjust them unless conditions change. The PID controller calculates an error signal based on these gains and the difference between the setpoint and the current frequency. The calculated error is added to the current control output, and the new control output is sent to the GPIB-to-analog interface, which passes it on to the mass flow controllers feeding the clockwise and counter-clockwise spin gas inlets. The control is done in such a way that the total gas flow remains constant while the proportion of the gas going to each spin inlet changes depending on the controller output. This feedback loop, once tuned, performs very well. As shown in figure 3.9, the feedback is capable of keeping the spin frequency constant to within 0.5 mHz for several hours (with occasional excursions beyond 0.5 mHz being quickly damped out).

### 3.3.6 Temperature Control of the Gas Bearing

In addition to controlling the spin frequency of the gas bearing, it is also sometimes convenient to be able to control its temperature. Temperature control is not always

---

<sup>12</sup>PID stands for Proportional Integral Differential, which are the three types of linear feedback used by such a loop.

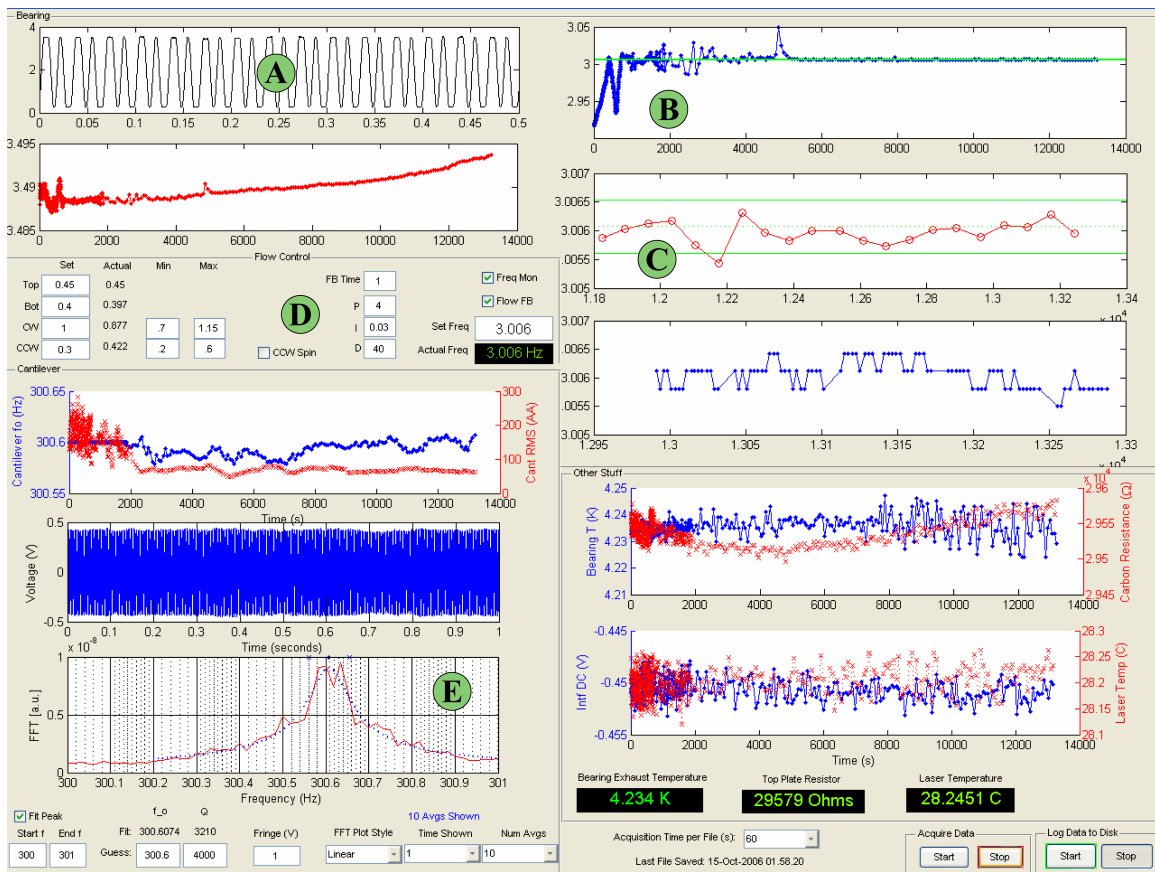


Figure 3.9: A screenshot of the data acquisition script that implements the software portion of the spin frequency feedback loop. Labeled parts are as follows. **A**: The most recent signal from the optical encoder. **B**: The rotational frequency of the bearing over 3.5 hours. The large variations in frequency in the first 1.5 hours are due to tuning of the PID loop. **C**: The rotational frequency of the bearing over the most recent 20 minutes. The feedback is keeping the frequency stable to within 0.5 mHz of the setpoint. **D**: The user-adjustable PID gains and limits. **E**: The fourier transform of the cantilever signal near the resonance. The blue dotted line is the Lorentzian fit used to extract the cantilever's  $Q$  and resonant frequency.

required, since the bearing can run stably at base temperature, but the ability to heat the bearing is useful both for the clearing of cryodeposits in the gas lines and for the investigation of thermal dependence of any systematic errors. In particular, the ability to heat the bearing above the  $T_c$  of lead ( $\sim 7^\circ\text{K}$ ) provides a powerful discriminator

of any effects due to superconductivity in the brass drive mass (see section 3.4.3).

The implementation of temperature control of the bearing is largely unchanged from the original London moment experiments [22, 23, 24, 25, 26]. All six gas lines contain heaters. These inline heaters, which sit near the top of the inner vacuum can, consist of wire wound around quartz rods. The resistance of the heaters in the top and bottom gas inlets is  $200\ \Omega$ , and the resistance of each spin gas heater is  $400\ \Omega$ . When connected all in parallel, the heaters then have a total resistance of  $50\ \Omega$ , which is a convenient value for driving with a regular temperature controller.<sup>13</sup> The thermometer used for temperature control is not the same one used in the London moment experiments— it is now a negative-temperature-coefficient carbon-glass resistor (CGR), which is suspended at the mouth of one of the spin gas exhaust ports of the bearing. It is the gold-colored cylinder visible in the photograph in figure 3.10. The thermometer thus measures the temperature of the gas exiting the bearing; at thermal equilibrium this should be the same as the temperature of the spinning rotor, since the rotor is not in contact with anything other than that gas. Since we are typically interested in the temperature of the drive mass (not the rotor), it might be better to put this thermometer in the exhaust flow of the top bearing gas rather than the exhaust flow of the spin gas. Currently the top inlet exhausts gas all around the circumference of the bearing, but this could be changed with a custom-made washer, as discussed in appendix E— such a change would enable a thermometer to be placed in the exhaust of the top gas fairly easily.

Operation of the temperature control is in theory straightforward; the exhaust gas temperature is measured and compared to a setpoint, and the heater currents are adjusted accordingly to increase or decrease the thermal power delivered to the inlet gas. In practice, this technique does not always work; in our first cooldown that produced data, we were unable to raise the temperature of the bearing above  $4.5\ \text{°K}$ , even with a heater power of 4 Watts. Lowering the pressure in the outer vacuum can alleviated this problem to the extent that we were able to heat the bearing to about  $8.4\ \text{°K}$  in the second cooldown.

---

<sup>13</sup>Lakeshore model DRC-93C.

### 3.4 Drive Masses

The drive mass consists of an alternating density pattern in a metal disc. The pattern is “buried” in the sense described below; to avoid systematic errors, no variation in the conductivity or height should coincide with the density variation. We have developed drive mass fabrication procedures for masses made from both brass and tungsten; the brass drive mass was used in our first cooldown.

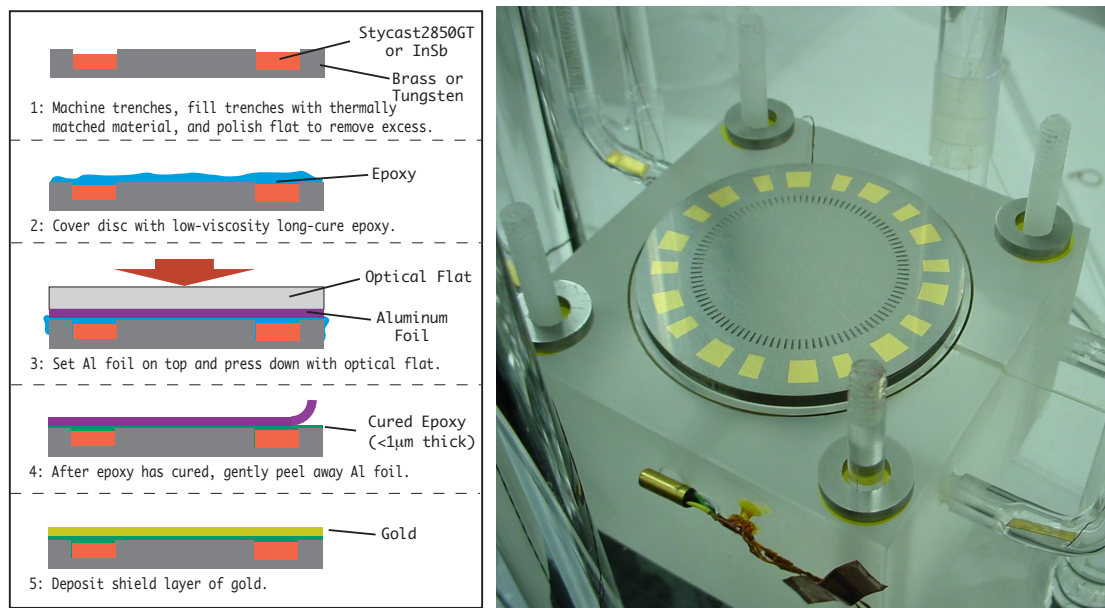


Figure 3.10: An outline (left) of the drive mass planarization process discussed in the text, and a photograph (right) of a drive mass attached to a rotor and installed in the gas bearing. The drive mass in the photo has not yet been planarized, so the mass trenches are still visible. Also visible is the gold pattern used by the spin speed detector.

#### 3.4.1 Selection of Drive Mass Materials

Design of drive masses for any experiment that hopes to sense mass-dependent forces must be centered around two goals: maximizing the mass-dependent force, and minimizing the sources of other (mainly electromagnetic) forces. The first goal can be

achieved by using the densest possible material. Attainment of the second goal, in experiments at this length scale, generally requires the elimination of variations in conductivity, height, and roughness.

In experiments of this sort, it is highly desirable to have more than one kind of drive mass. One practical reason for this is the difficulty of the fabrication of the drive masses— if more than one approach is pursued, the likelihood of getting a usable mass is higher. More importantly, an experiment with multiple mass types that can be used is far more robust: since masses can be switched relatively easily, the different predicted signals from drive masses with different densities provides a powerful check on any gravity-like signals that might be observed.

In this experiment our approach has been to use pairs of materials to make the drive mass: a disc made of one dense material, and trenches etched or machined in the disc and filled with another, less-dense material for purposes of planarization. Since the experiment is designed to be operated at low temperatures, any planarization technique must take account of the fact that most materials contract by a substantial amount when cooled from 300 °K to 4 °K. If the two materials used to make a drive mass have substantially different linear contractions when cooled, even perfect planarization at room temperature will not result in a mass that is flat at low temperatures. The requirement is thus for pairs of materials with high density contrast but low thermal expansion contrast. Figure 3.11 shows some relevant data.

In the Frogland experiment, the drive masses were made of gold and silicon. That pair of materials is a poor thermal match, and thus not suited to the larger drive masses used in the Frogstar experiment. Even if that were not the case, the many difficulties we had polishing gold for the Frogland experiment<sup>14</sup> would have been magnified on the much-larger-area Frogstar mass discs.

Tungsten immediately suggested itself as an alternative candidate material— it is very dense, it is much harder than gold (which eases polishing), it is refractory (which enables some processing steps that require high heat) and it has an anomalously low thermal expansion coefficient for a metal. The last virtue also poses a challenge,

---

<sup>14</sup>Gold is a horribly gummy and highly overrated metal. If you can avoid having to polish it precisely, do so.

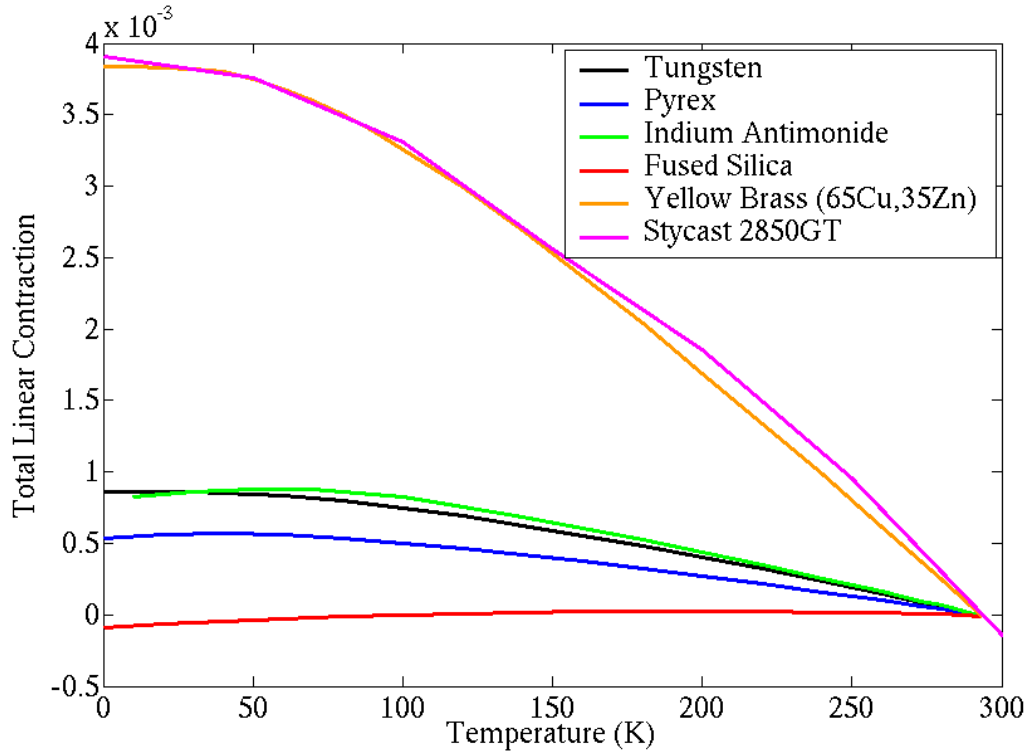


Figure 3.11: The total linear contraction (defined as  $\frac{L_{293}-L_T}{L_{293}}$ ) versus temperature, plotted for selected drive mass candidate materials. The data are from two heroic and indispensable publications which catalog the low-temperature behavior of a large range of technical solids [28, 29].

since there are no filled epoxies with thermal expansions low enough to match that of tungsten.<sup>15</sup> However, when consulting the National Bureau of Standards’ deathless monograph “Thermal Expansion of Technical Solids at Low Temperatures,” we noticed a peculiar fact that is also illustrated in figure 3.11— indium antimonide has an almost identical thermal expansion coefficient to that of tungsten, all the way down to 4 °K. This coincidence is peculiar because the two materials have almost nothing else in common. Indium antimonide is a III-V semiconductor with a low melting

<sup>15</sup>The thermal expansion coefficient of a filled epoxy is generally tailored by adding fused silica powder, which has essentially zero thermal expansion, to the mixture. However, there is a limit to the percentage of fused silica powder that an epoxy matrix will support before it ceases to cohere. This limit does not allow an epoxy like Stycast 1266 to be filled with enough fused silica to thermally match it to tungsten (we tried).

point (500 °C) and an extremely high natural electron mobility; its chief use seems to be as an infrared photodetector in very sensitive (typically military) thermal imaging systems. The low melting point, at least, was convenient, as it allowed for the possibility of filling the trenches in the tungsten disc with liquid indium antimonide and allowing it to solidify. The fabrication of the W-InSb drive mass (and its current status) is discussed below, in section 3.4.2.

The other drive mass material we have put significant effort into is free-cutting brass. This material, while substantially less dense than tungsten, has two important advantages: it is vastly more machinable, and its higher coefficient of expansion can be easily matched with commercially available epoxies. These advantages make it far easier to fabricate a drive mass from brass than from tungsten; indeed, the mass we used in our first cooldown was made with brass and Stycast 2850GT (the epoxy whose linear contraction is graphed in figure 3.11). Its fabrication is discussed below. One important feature of the free-cutting brass that we did not at first anticipate is a result of the fact that it contains about 2.5% lead (used to enhance machinability). It appears that this lead is not soluble in the copper-zinc bulk of the brass, and aggregates into macroscopic particles. This aggregation is important because bulk lead is a superconductor below 7.2 °K. SQUID measurements we have done on our drive masses (see figure 3.14) show unambiguously that the brass undergoes a superconducting transition near that temperature.

Other dense drive mass materials that we considered or that were suggested to us included silver, an alloy of tungsten with rhenium, platinum, osmium, and (fancifully) neutronium. The last three elements in that list are impractical in varying degree. The alloy of tungsten with rhenium has many of the properties of tungsten but with better machinability— this is probably not enough of an advantage to justify making a new drive mass with it, since the fabrication problems associated with tungsten’s low machinability have largely been solved. Silver is perhaps the most promising of the bunch— surprisingly cheap and somewhat denser than brass but with almost exactly the same linear thermal contraction, it could be substituted for the brass in the recipe described below without added difficulty. It would of course also differ from brass in that it lacks superconductivity at 4 °K.

Possible studies of the Casimir effect [30] using this apparatus would require the drive mass to be replaced by an insulating disc upon which one could deposit conductive material in a pattern similar to that of the trenches in the normal drive mass. Drive mass discs made of fused quartz with matching washers were designed and fabricated for this purpose, as were shadow-masks for the deposition of the gold pattern. They have not yet been used, but could in the future prove useful for experiments to measure or constrain systematic errors in the gravity measurement, as well as for Casimir force measurements.

### 3.4.2 Drive Mass Fabrication

The fabrication of the drive masses was by far the most time-consuming aspect of this experiment, due to the combined requirements of near-perfect planarization, isoelectronic construction, and high density contrast. With a great deal of trial and error, we developed fabrication procedures for two material pairs: tungsten with indium antimonide, and free-cutting brass with Stycast 2850GT epoxy. For the possible benefit of future operators of this experiment, I have included here many details of the fabrication procedures, including some discussion of unsuccessful strategies we tried. Readers uninterested in actually making a drive mass themselves may want to skim....

#### **Tungsten drive mass fabrication**

Here we discuss the method of fabrication of the tungsten drive mass. First, the disc is cut from a plate and a pattern of trenches is machined into it using electrical discharge machining (EDM)—tungsten is too hard and brittle for precise conventional machining. Since the trenches do not pass entirely through the disc, a “sinker” EDM technique using a custom-machined graphite electrode must be applied. Typically several graphite electrodes are required for each drive mass, since they wear away quickly at the very high local temperatures necessary for machining tungsten in this way. In addition to the main radial trenches in the top of the drive mass, a small annular trench is cut into the back side of the disc. This trench is used for attaching the disc to the quartz rotor of the gas bearing with epoxy—the trench acts as

a “moat” that keeps the area of epoxy small, minimizing stresses due to thermal contraction. Because of the long time necessary for the machining and the small tolerance for alignment error, care must be taken by the machinists to take account of thermal expansion of the parts and of the machine itself. Our first batch of tungsten drive masses was afflicted with a misaligned trench pattern due to a slow heating of the EDM machine that moved the electrode out of alignment.

After the trench machining, the drive mass disc is double-lapped. In contrast to a normal lapping machine, which holds the part rigidly and moves it with respect to a single lapping tool, a double-lapping machine allows the part to move freely between two counter-rotating lapping tools. This setup allows the lapping of both sides of a flat part simultaneously, which greatly reduces non-planarity problems due to released stress. Single-sided lapping of the tungsten masses was attempted more than once, but nearly always resulted in bowl- or pringle-shaped deformations of the disc that were time-consuming to remove. Double-lapping the drive masses requires sending them off campus, but (at least for tungsten) gives much better results. The results of any lapping procedure can be checked with an optical flat and a source of reasonably monochromatic light; the interference fringes produced between the flat and the drive mass provide a measure of the flatness that is accurate to better than half a micron. Our goal, which we were able to achieve with help from Tim and Ryan at the Ginzton crystal shop, was to make any flatness errors result in height deviations of less than one micron across the 2-inch drive mass disc.

After polishing and characterizing the flatness of the disc, the trenches must be filled with the thermally-matched companion material indium antimonide. Several different techniques for this were attempted, all based on heating chunks of indium antimonide placed on the drive mass so that they melted, flowed into the trenches and filled them. This melting generally had to be done in a vacuum or an inert atmosphere to avoid the formation of tungsten oxide (which is yellow-green, powdery, and water-soluble). A small vacuum furnace made of molybdenum foil with a tungsten heating filament was constructed to heat the drive mass from above, but the uneven radiant heating led to undesirably patchy results. Subsequently, an electron beam (from the reactive ion-beam etcher in the Moore building) was directed onto the center of

the tungsten disc and used to heat it above the melting temperature of the indium antimonide. This technique worked reasonably well, but the good vacuum necessary for the e-beam led to large temperature gradients between the disc and the InSb chunks, which again adversely affected the yield. Finally, a thermal evaporator was modified by the addition of a serpentine molybdenum heating element. The heating element, through which several hundred amps could be run by the evaporator's power supply, was electrically insulated by small sapphire pieces from a square plate (also made of molybdenum) upon which the drive mass could be rested. This apparatus allowed us to heat the drive mass evenly in several torr of continuously flowing nitrogen gas, which minimized the problems with thermal gradients and greatly improved the results of trench-filling.

Even with this last setup, though, the wetting of the indium antimonide to the tungsten was often unsatisfactory. Good wetting being essential for reliable trench-filling, we explored ways to promote adhesion and minimize the wetting angle between the two materials. Two techniques were found to improve the quality of the results. The first was to press down on the indium antimonide with a flat piece of graphite—this pushes the molten semiconductor into the trenches, overcoming the large surface tension of the droplets. The indium antimonide will not stick to the graphite. The other technique that promotes good wetting is to clean the tungsten disc thoroughly before the melting is performed. The best way to clean it seems to be to immerse it in a boiling solution of 25% potassium hydroxide for a few minutes. Ultrasonic cleaning in KOH can also help, but it sometimes dislodges indium antimonide that remains in the trenches from previous melting attempts.

After the melting step, the drive mass must be lapped to remove the excess indium antimonide that projects above the top surface of the disc. Single-sided lapping is OK for this step, since very little tungsten is removed. The result, ideally, is a tungsten disc with trenches that are filled up to a few microns below the surface of the disc by indium antimonide. The reason that the top surface of the filler ends up slightly below that of the tungsten is that the softer material is removed more rapidly by the lapping grit. Generally, one does not know the full results of the InSb melting step until after the excess has been polished away, since only then can the adhesion and

percentage of trench-filling be measured accurately. This problem contributes to the long turnaround times and general difficulty of the drive mass fabrication procedure.

When the trenches are satisfactorily filled, the final step of planarization is performed. This step (illustrated on the left side of figure 3.10) is the same for both brass and tungsten drive masses, and has been tested more extensively on brass drive masses. For that reason, I discuss it in the next section, on brass drive mass fabrication.

### **Brass drive mass fabrication**

The fabrication of the brass drive masses follows essentially the same pattern as that of the tungsten drive masses: initial machining, lapping, trench filling, and planarization. Brass masses are, however, substantially easier and cheaper to make than tungsten ones. This ease of fabrication is due partly to considerations of machinability and low stress, but more importantly to the much easier task of matching its thermal expansion coefficient. The particular brass alloy used for the drive masses is “free-cutting brass” (UNS C36000). This alloy contains approximately 62% copper, 35% zinc, and 2.5% lead. Since this material is designed to have excellent machinability, the disc itself, the mass trenches on the top, and the gluing trench on the bottom can all be cut out with conventional machining. The brass is also easier to lap than tungsten, in part because it contains less intrinsic stress—this characteristic allows it to be successfully lapped with the single-sided lapping machines available in the Ginzton crystal shop.

After lapping the disc, the trenches are filled with Stycast 2850GT, mixed in the appropriate ratio with catalyst 11.<sup>16</sup> This epoxy is designed to be thermally matched with brass, as is evident in figure 3.11. The epoxy is degassed in a vacuum system both after mixing and after potting, to ensure a void-free filling of the trenches. It is then cured at 90 °C under a heat lamp for 24 hours. As with the indium antimonide, excess epoxy can then be removed by gentle lapping. After lapping, the top surface of the epoxy is typically one or two microns lower than the top surface of the brass;

---

<sup>16</sup>Both ingredients are made by Emerson & Cuming ([www.emersoncuming.com](http://www.emersoncuming.com)) and distributed by fine purveyors of technical adhesives everywhere.

this is again because of the faster lapping of the filler material.

The filled and lapped drive mass must then be planarized. The planarization procedure is illustrated in figure 3.10. The first planarization step consists of covering the whole top surface of the drive mass with Stycast 1266,<sup>17</sup> a very inviscid (650 cP) and slow-curing (8-16 hrs) epoxy. This epoxy must be made to cure in a very thin and flat layer, so that it will planarize the disc without increasing the distance between the metal of the drive mass and the test mass. This goal can be achieved by pressing hard on the epoxy while it cures with something that is very flat. Empirical and theoretical [31] analyses agree that the epoxy layer can be made less than a micron thick with a few pounds of pressure, given the stated viscosity and cure time. The pressure is typically supplied by a large lead brick atop an optical flat.

After the epoxy cures, though, one is left with a problem: the flat object that was used to press on the epoxy is now stuck very securely to the drive mass, and cannot be removed without destruction of the epoxy layer. This undesirable adherent represents an important practical hurdle that we tried several techniques to surmount. The first technique involved the use of a silicon wafer with a 4  $\mu\text{m}$ -thick layer of silicon nitride on it, which was pressed against the epoxy, nitride side down, by the lead-brick-bearing optical flat. After the curing, the silicon wafer was etched away with a 60  $^{\circ}\text{C}$  solution of 30 % potassium hydroxide, leaving the metal disc covered with a flat piece of silicon nitride 4  $\mu\text{m}$  thick. The epoxy had to be protected from the etchant with a layer of Apiezon W wax—the KOH does not seem to actually etch the epoxy, but it does very rapidly inhibit its adhesion. This process, although it produced some successful planarizations, turned out to be difficult and low-yield and was abandoned. The next technique we tried was to press on the epoxy with a thick piece of teflon that was machined as flat as possible. This procedure works, and the epoxy does not stick to the teflon, but it turns out to be very difficult to get the teflon flat enough in the first place, due to its malleability and high thermal expansion coefficient.<sup>18</sup> We tried both lathing and lapping of the teflon, but the results were unsatisfactory. This procedure too thus had to be abandoned. The trick that finally worked for us was to

---

<sup>17</sup>Also an Emerson & Cuming product.

<sup>18</sup>Here as elsewhere, by “flat enough” we mean flat to better than a micron across the piece—in general, we strove to bring all distance tolerances and errors in the experiment below a micron.

press on the epoxy with a very flat and smooth piece of aluminum foil (again, under an optical flat which itself is under a lead brick). The epoxy does not adhere well to the aluminum, and it is possible to carefully peel off the foil after curing without damaging the very thin epoxy layer. Normal kitchen-grade aluminum foil tends to have a graininess to its surface topography that gets transferred to the epoxy, so we ordered a technical foil<sup>19</sup> with a finer finish that worked very well.

The result of the final planarization procedure is a flat drive mass disc with a thin ( $< 1\mu\text{m}$ ) layer of Stycast 1266 covering the top surface and smoothing out the slight corrugation that remained after the trench-filling. A 100-Angstrom layer of titanium (for wetting) and a several-thousand-Angstrom layer of gold are then deposited on the disc in a circle that covers the trench pattern. This layer is what makes the drive mass “isoelectronic”— along with the similar layer of gold on the bottom surface of the cantilever wafer, it provides essential shielding against electrostatic and Casimir [30] effects. The effectiveness of a shield layer of a given thickness can be estimated using the fact [11] that the ratio of the Casimir force  $C_\infty$  between two semi-infinite conducting plates and the Casimir force  $C_d$  between two plates of finite thickness  $d$  is roughly given by:

$$\frac{C_d}{C_\infty} \simeq 1 - e^{-4\pi d/\lambda_p}, \quad (3.1)$$

where  $\lambda_p$  is the plasma wavelength ( $\sim 135$  nm for gold). For a shielding layer 3000 Angstroms thick, the exponential term is unmentionably tiny, corresponding to an essentially complete shielding of any differential Casimir force. The two equipotential surfaces provided by the layers of gold on the drive mass and shield also help minimize electrostatic effects, although the quantitative characterization of this effect is slightly tricky. The naively calculated skin depth of gold at the very low frequency of 300 Hz is actually fairly long ( $\sim 30 \mu\text{m}$  at helium temperatures). However, a skin-depth-type treatment may not be appropriate in a regime where the wavelength of the field excitation is  $\sim 10^{11}\times$  larger than the largest length scale in the system. Further investigations of the role of the gold layers in suppressing electrostatic coupling are warranted. The brass drive mass is pictured before and after the deposition of this

---

<sup>19</sup>The foil we used was 4-mil “Special Bright” aluminum from All Foils, Inc, ([www.allfoils.com](http://www.allfoils.com)).

shield layer in figure 3.12.

Each drive mass disc must also be accompanied by washers made of the same material and lapped to the same thickness. These washers support the lid of the gas bearing, and maintain the proper clearance between the drive mass and the lid. The washers for one of the tungsten drive masses can be seen installed in the probe in figure 3.10.

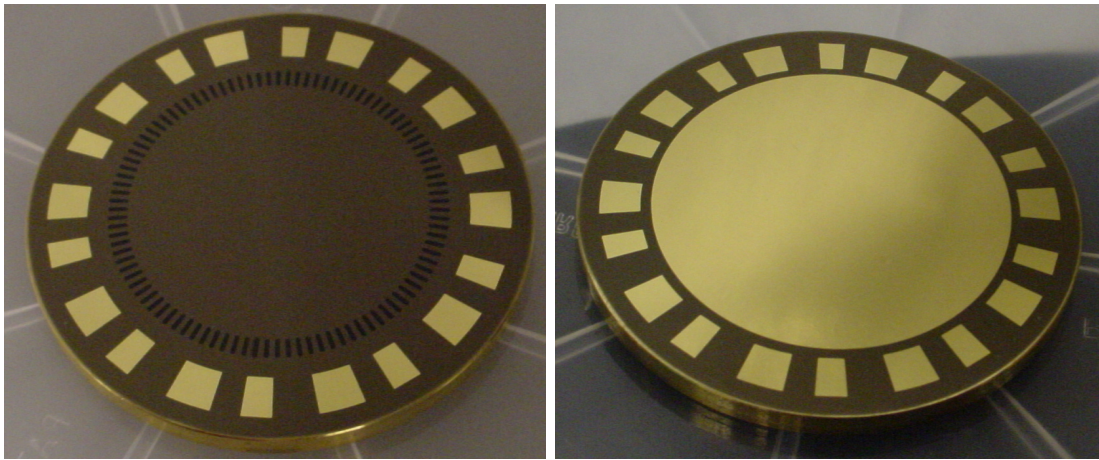


Figure 3.12: Left: The brass drive mass after final planarization with Stycast 1266. The black epoxy filling the trenches can still be seen, because the 1266 is optically transparent. Right: the same mass after deposition of the gold shielding layer. Note that the mass pattern is no longer visible. The patterned layer around the edge in both images is part of the optical encoder that detects the disc's rotation.

### 3.4.3 Drive Mass Characteristics

The end product of this fabrication process is a disc with a circumferential pattern of density variations (100 trenches total) but with no periodic variation in the height or conductivity that might give rise to non-mass-dependent forces. The density pattern is positioned so that when the drive mass is rotated in the gas bearing, the test mass on the cantilever is alternately above high-density and low-density areas. Any force that couples to mass will thus produce an oscillating deflection of the cantilever and an AC signal in the interferometer, at 100 times the rotational frequency of the drive

mass. This drive mass configuration, with no variation in the conductivity or height, is sometimes referred to as a “buried drive mass” [32] or “isoelectronic” [11] configuration. Such an arrangement is essential for precision gravity measurements, since the force from gravitational interactions is much smaller than typical electrostatic or even Casimir forces [30] at these length scales.

Once the planarized drive mass was constructed, its flatness was characterized by scanning it with an Alphastep profilometer. Ideally, all deviations from perfect flatness should be less than one micron in amplitude, and there should be no evidence of the periodicity of the buried mass pattern. Profilometer scans of our best drive masses (see figure 3.13) showed that they attained this ideal. The brass mass used for the first data-taking runs was flat to better than 1 micron across its 2-inch diameter, and had roughness of about 750 nm.

Since it is difficult to effectively shield the test mass against magnetic interactions, it was also important to characterize the low-temperature magnetic properties of the drive mass in order to place limits on the size of any possible magnetic coupling. The presence of lead (at the 2.5% level) in the brass drive mass made such a measurement even more important, since lead is a superconductor at 4°K. To measure the low-temperature magnetic properties, a small piece was cut off of one of the brass drive masses and placed in a commercial cryogenic SQUID magnetometer. The sample was cooled from room temperature to 2°K in a 100 Gauss magnetic field, and the measured magnetic moment was recorded as a function of temperature. The results are plotted in figure 3.14. The superconducting transition of the drive mass piece is clear, and occurs only slightly below the bulk critical temperature of lead. This surprising result must be due to aggregation of fairly large lead particles in the copper-zinc mixture that forms the rest of the brass, since one would expect the proximity effect to suppress superconductivity of very small lead grains. In any case, this superconducting transition, and any possible magnetic test-mass-drive-mass interactions that result from it, must be taken into account. This is the main reason for our efforts to operate the bearing at an equilibrium temperature above the  $T_c$  of bulk lead.

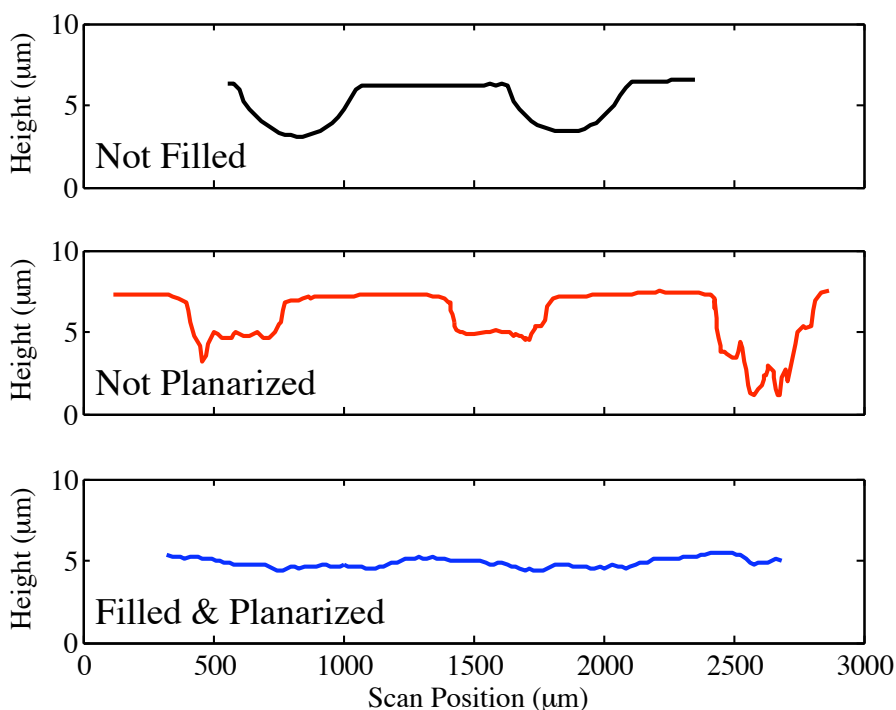


Figure 3.13: Profilometer scans of three different drive masses. **Top:** The trenches of this mass were filled with Stycast 1266. The large dips visible at the trenches are due to shrinkage in the 1266 during curing. **Middle:** The trenches of this drive mass were filled with Stycast 2850GT to a level above the top surface of the mass. The top surface was then ground and polished to remove excess epoxy. The dips visible at the trenches are due to faster removal of the epoxy than of the drive mass metal during grinding. **Bottom:** This drive mass (the one with which we ultimately took data) was filled, polished, and planarized, in the manner described in the text. Variations in the height are mainly due to the roughness of the aluminum foil used for press-curing the planarizing epoxy, and are about 750 nm peak-to-peak.

### 3.5 Test masses

The test mass is a small rectangular prism of solid gold a few tens of  $\mu\text{m}$  thick. It is surprisingly difficult to precisely fabricate metallic objects at this length scale, which falls in between the natural length scales of conventional machining and of micromachining. We have tried multiple techniques of making these masses. The best fabrication method for the Frogstar experiment, an electrochemical micro-casting

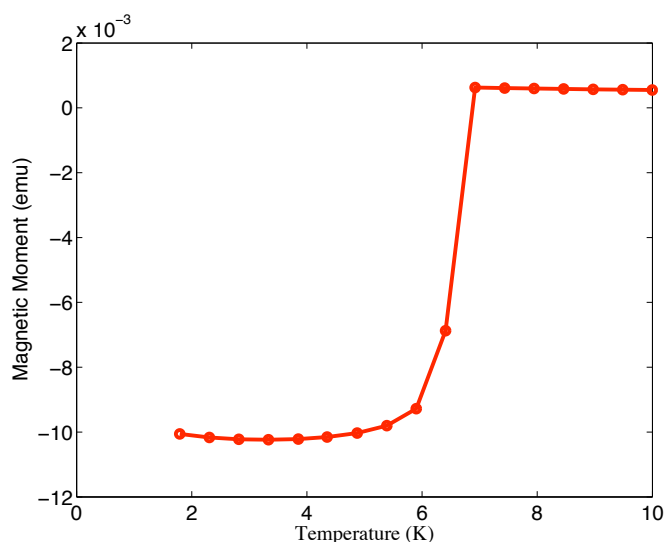


Figure 3.14: Magnetic moment versus temperature of a 0.267-gram piece of the free-cutting brass used to make the brass drive masses. The superconducting transition of the lead in the brass is obvious. The data were taken in a commercial SQUID magnetometer.

process, is illustrated in Figure 3.15.

### 3.5.1 Test Mass Fabrication

First, trenches are plasma-etched into a silicon wafer; the trench pattern consists of an array of small rectangles (200 or 400  $\mu\text{m}$  by 100  $\mu\text{m}$ ) connected by much smaller trenches 10  $\mu\text{m}$  wide, and is created by standard lithography using photoresist. A critical step not shown in figure 3.15 is the deposition of a silicon nitride layer before the trenches are etched. This step is important because the relatively low resistivity of the silicon wafer can spoil the electroplating process by introducing additional current paths that result in gold deposition in places other than the mass trenches. The silicon nitride layer has a high resistance and thus eliminates this problem. A seed layer of gold is deposited; the remaining photoresist is then lifted off, leaving only the bottoms of the trenches covered with gold, and the original wafer surface still covered with silicon nitride. Much more gold is then electroplated onto the wafer

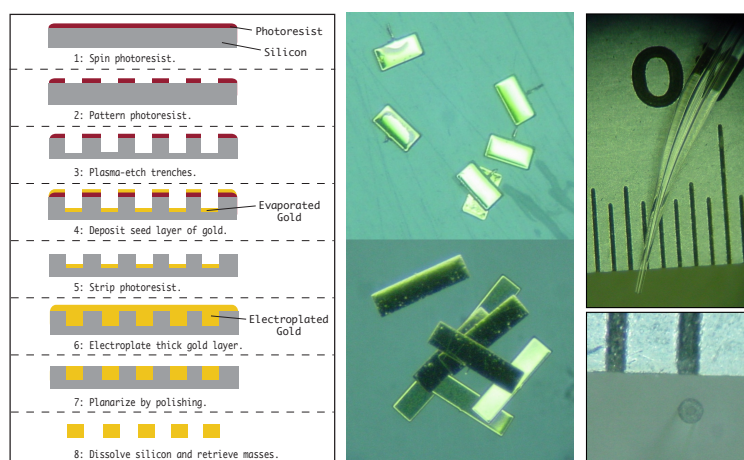


Figure 3.15: Left: an outline of the test mass fabrication process, as discussed in the text. Center: photographs of two different sizes of test mass— $200\mu\text{m}$  by  $100\mu\text{m}$  (top center) and  $400\mu\text{m}$  by  $100\mu\text{m}$  (bottom center). Stubs of the wires used for electroplating are visible on some of the masses. Right: photographs of the glass vacuum chuck used for test mass manipulation and attachment. The  $\sim 75\mu\text{m}$ -diameter inlet is visible in the bottom right-hand picture. The lines on the ruler are  $500\mu\text{m}$  apart.

up to a thickness of 40 or 50  $\mu\text{m}$ . The rectangular trenches will become the test masses, and the smaller trenches are used as wires to make electrical contact during the plating process. Extensive electroplating tests with homemade plating setups and various non-toxic sulfite-based plating solutions validated the general rule so often true in experimental physics: “the more toxic, the better.” Yield and quality of the test masses was *vastly* improved by doing the electroplating in a traditional cyanide-based solution at the SLAC plating shop— this is the procedure that we followed to make the 400- $\mu\text{m}$  test masses that were installed on cantilevers and used in the experiment. One problem with electroplating micro-scale items in certain regimes of current and geometry is the buildup of gas at the plating surface. This gas, a normal result of the plating process, can create a bubble inside the mass trench that blocks further plating and results in poor yield and uneven coverage. Similar problems can be caused by a local depletion of the ions in the plating solution at high current densities. The solution to these problems that we adopted is to use a pulsed current source for the plating. If the pulse duty cycle is properly adjusted, this allows the gas to dissipate

between pulses and allows diffusion of the gold ions to keep pace with the plating rate. The higher instantaneous current density can also improve the morphology of the resulting metal [33]. We achieved good results with a pulse duty cycle of 4:1 (20 ms with current on followed by 5 ms with current off) and a current density of about 8 milliamps per square centimeter. An even more interesting technique possibly applicable to this kind of micro-casting is reverse-pulse plating, which has the same advantages as normal pulse plating but adds an electropolishing step to the pulse cycle by including a brief negative spike in the current [33]. This technique has been shown to be capable of improving the quality of plated materials. Since the quality of our initial runs was good, we did not investigate the reverse-plating process in depth despite being somewhat tempted.<sup>20</sup> After the plating, the top surface of the wafer is polished flat and the silicon is dissolved in potassium hydroxide. What is left is a set of small rectangular solid gold prisms 200 or 400  $\mu\text{m}$  long, 100  $\mu\text{m}$  wide, and having a thickness determined by the polishing step.

This process works well, and is substantially higher-yield than previous evaporative techniques we used for making test masses for the Frogland experiment. One wrinkle of both these processes is that there can be fairly substantial thickness variation within a single batch of masses, which can lead to substantial mass variations. The variation is due to the fact that it is difficult to enforce perfect parallelism across the test mass die during the polishing phase of the process. If the polishing plane is not parallel to the plane of the trench bottoms, there will be thickness variation in the masses after they are released. In practice, we do see a range of test mass thicknesses— for example, our last batch of 400  $\mu\text{m}$  masses appears to range in thickness from 5  $\mu\text{m}$  to 10  $\mu\text{m}$ . Although we were initially aiming for thicker masses, this range of thicknesses can actually be convenient, since it enables us to put several of these thin masses on a single cantilever to achieve a desired resonant frequency.<sup>21</sup> The cantilever used in the first data run of the experiment had 4 masses piled on it, which drove the resonant frequency down to about 300 Hz. A cantilever with multiple 400

---

<sup>20</sup>This decision was made on the advice of Ted Geballe, who told me “you don’t want to become an electrochemist if you can possibly avoid it.”

<sup>21</sup>The thickness of the epoxy layer between individual masses is much less than a micron— negligible compared to the thickness of even our thinnest test masses.

$\mu\text{m}$  masses on it can be seen in figure 3.20.

To measure the thickness variation and check the density of the electroplated gold, an electrobalance was used to weigh a representative sample of test masses. Individual  $400\ \mu\text{m}$ -long test masses were added to the pan of the balance one by one, and the total mass was recorded after each addition. The mean slope of the resulting mass versus number graph then furnished an estimate of the mean mass value, and the standard deviation of the mass increase per step gave an estimate of the scatter in mass. The results of this mass weighing are shown in figure 3.16. The mean mass for this batch of  $400\ \mu\text{m}$  test masses was determined to be  $5.4\ \mu\text{g}$ , and the standard deviation was determined to be  $\sim 2\ \mu\text{g}$ . This standard deviation is at least twice the expected error of the electrobalance and thus probably is reflective of a polishing “wedge” causing varying mass thickness within the batch. The measured mean mass agrees well with the expected mass of solid gold rectangular prisms with a mean thickness of  $7\ \mu\text{m}$ .

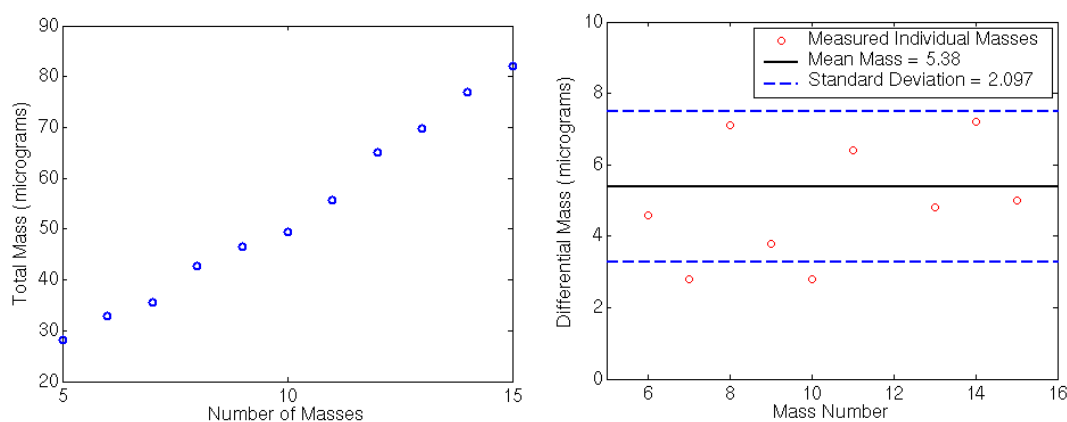


Figure 3.16: These graphs present the results of the test mass weighing procedure described in the text. Left: total mass measured by the electrobalance versus number of test masses in the pan. Right: individual masses, extracted by taking the derivative of the curve on the left. The mean value and standard deviation are also plotted. The standard deviation is larger than the error of the microbalance, indicating a spread in test mass thickness. The mean mass value, combined with the optically measured linear dimensions of the masses, supports the assumption that our test masses are solid gold prisms.

The range of thicknesses of our test masses means that it is difficult to precisely determine the total mass that has been put on any given cantilever. Once they are attached to a cantilever, though, the masses are on a much more sensitive scale than any electrobalance. The spring constant of the cantilever can either be predicted from knowledge of its dimensions or measured using radiation pressure (see section 3.6.5). Once the spring constant  $k$  of the cantilever is known, the mass  $m$  of the attached test masses can be easily determined by measuring the resonant frequency  $\omega_0$  of the cantilever:  $m = k/\omega_0^2$ , since the mass of the cantilever can be neglected.

### 3.5.2 Test Mass Manipulation and Attachment

Once the test masses are released from the silicon die, they must be handled with great care; an errant cough can scatter thousands of masses from an open container. In addition, the manipulation of the test masses presented a problem similar to the problem of fabricating them. Too small to hold with tweezers but too heavy to pick up with Van der Waals forces, they fall in between two natural length scales of micromanipulation. This was not the case for the much smaller Frogland masses, which we were able to pick up simply by bringing a probe tip close to them, presumably due to Van der Waals-type interactions.

The problem of manipulating the larger Frogstar test masses was solved by using a tiny handmade glass vacuum chuck. A glass micropipette with an inner diameter less than a millimeter was heated in the flame of a propane torch and gently pulled in order to stretch out the middle portion. It was then bent at 90 degrees, allowed to cool, and broken near the bend. The broken end was polished flat using optical-grade sandpaper. The result is a bent tube that tapers down to a flat annular end with a small inner diameter. A small vacuum pump is attached to the larger end of the tube via a small flexible hose so that the tube sucks in air through the small end. The tube is then mounted on one of the micrometer stages of a probe station microscope, which allows it to be translated in  $x$ ,  $y$ , and  $z$ . If the inner diameter of the small end is smaller than the width of the test masses (100  $\mu\text{m}$ ), the tube can then be used to pick up and move around the tiny masses like an ordinary vacuum chuck.

Disconnecting the vacuum pump causes the chuck to gently drop the test mass. This technique works very well, and allows reliable and accurate positioning of test masses. Two pictures of the business end of the chuck can be seen in figure 3.15.

Using the miniature vacuum chuck, the procedure of attaching test masses to the cantilevers is fairly straightforward although somewhat low-yield. We describe the process in detail here for the benefit of future users of similar mass-loaded cantilevers. The whole process takes place under a probe station microscope, since both test masses and cantilevers are difficult to see with the naked eye. First, a suitable test mass is selected, rotated to the proper orientation, and picked up with the vacuum chuck. Then some Torr-Seal epoxy<sup>22</sup> is mixed, a small amount is transferred to a spare silicon wafer piece in the probe station microscope, and a tiny dab is picked up off the wafer using a probe tip. Torr-Seal is used mainly for its convenient curing time of about 20 minutes. It should be noted that none of the solid white filler material of the Torr-Seal is picked up; only the clear liquid epoxy itself adheres to the probe tip. Typically the probe tip must then be “blotted” several times on the wafer surface to remove excess epoxy. This blotting step is perhaps the most important determinant of success in this procedure. If there is too little epoxy on the probe tip, the test mass will fall off; if there is too much epoxy, it can flow off the edge of the cantilever and stick it down to the silicon nitride shield. The amount of epoxy on the probe tip can be controlled by carefully observing the amount that comes off onto the wafer in each blotting step. Laden with the proper amount of epoxy, the probe tip can then be gently brought into contact with the tip of the selected cantilever to transfer a drop of epoxy to it. This transfer requires moving the probe all the way down to the bottom of the cantilever trench; great care must be exercised in order to avoid punching through the delicate silicon nitride shield at the bottom of the trench. After the application of the epoxy, the test mass can be slowly lowered into position by the vacuum chuck. The vacuum pump is then disconnected and the chuck withdrawn— if all goes well, the test mass is pulled against the cantilever by the wet epoxy and rests snugly on the end of the cantilever while the epoxy cures. Unless there is a piece of dust between the test mass and the cantilever, the thickness of the epoxy layer ends

---

<sup>22</sup>Also known as Hysol 1-C

up being much less than a micron. For this experimenter, the whole process had a yield of about 25%, in the sense that if test mass attachment was attempted on four cantilevers, one of them would be good enough for experimental use. As long as none of the shields are broken, a failed attachment does not ruin an entire eight-cantilever wafer, so it is generally possible to get at least one good mass-loaded cantilever on each wafer. One innovation that improved the yield of this process for cantilevers with multiple test masses was to pre-glue individual test masses to each other before attaching them all at once to the cantilever. This pre-gluing greatly reduces the chances of breaking or sticking down the cantilever, since only one excursion into the trench is required.

One somewhat surprising aspect of this method of test mass attachment was the discovery that the epoxy layer does not seem to cause significant damping of the cantilever's oscillations even at room temperature. Quality factors of cantilevers with epoxied test masses were not significantly different from those of bare cantilevers when both types were placed in a vacuum of  $10^{-6}$  torr. This behavior was observed both in these silicon nitride cantilevers and in the silicon cantilevers used in the Frogland experiment. This is likely due to the fairly complete curing of the torr-seal leaving not much viscous residue, and to the fact that the epoxy is located at the portion of the cantilever that bends least in the first flexural mode.

## 3.6 Cantilevers

The cantilever is a Hooke's law spring for the small displacements involved in these measurements—it linearly converts the force on the test mass to a displacement. Our cantilevers have spring constants of about  $10^{-2}$  N/m, and resonant frequencies (with the test mass attached) of about 350 Hz. Photographs of the cantilevers appear in Figure 3.17.

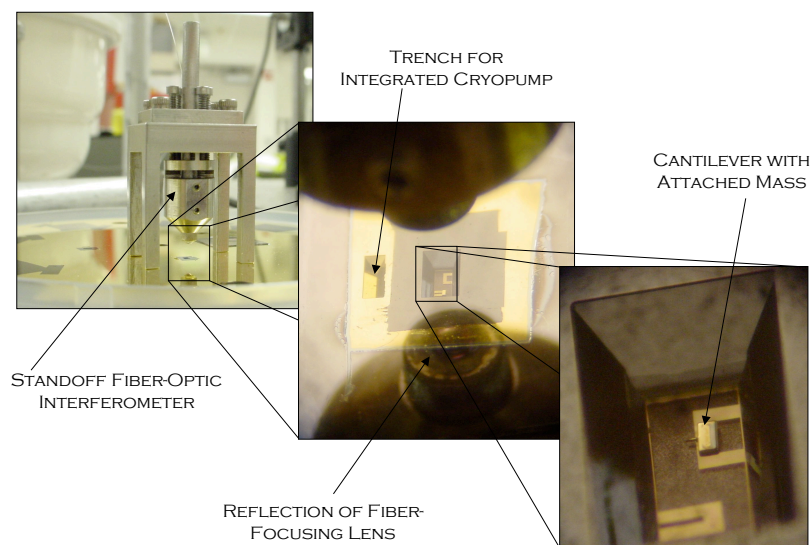


Figure 3.17: Photographs of the cantilevers taken at three different magnifications. Labeled parts are explained in the text.

### 3.6.1 Cantilever Design

The design of the cantilevers was the subject of a fairly extensive optimization process, due to the need to balance many competing factors to maximize the experimental sensitivity. Some of these factors included the spring constant (lower is more sensitive), the frequency (higher is better for averaging purposes), the width, the length, the quality factor (higher is better), the fabrication yield, and the amount that the mass-loaded cantilevers droop in the earth’s gravity (lower is better, for parallelism and to avoid stiction [34]). Ultimately we decided to use pairs of cantilevers in two different sizes. Both are two-legged cantilevers, rather than rectangular ones— this design allows a cantilever to take wider test masses while keeping the spring constant low. The main reason for not putting more than two cantilevers in each trench was our desire to keep the shield membrane beneath the cantilevers as small as possible, in order to minimize deflection of that membrane under pressure.

### 3.6.2 Cantilever Wafer Fabrication

We use an un-diced 4-inch cantilever wafer to form the top flat surface of the gas bearing. The cantilever wafers were fabricated using standard microfabrication techniques. Each wafer contains eight cantilevers, arranged in pairs about  $10\ \mu\text{m}$  above the bottom of four trenches around the wafer. Each trench is etched all the way through the silicon wafer to a  $4\text{-}\mu\text{m}$ -thick silicon nitride layer at the bottom of the wafer. This nitride layer, when coated with gold, forms the “shield membrane.” This membrane provides a second layer of electrical shielding between the drive and test masses and allows the cantilevers to be kept in vacuum while gas is flowing in the bearing. Six round through-holes are etched in the wafer during fabrication: one in the center for the top bearing gas inlet, one between two cantilever trenches for the optical encoder to look through, and four around the edges for the quartz bolts attaching the bearing lid to pass through. A photograph of a cantilever wafer is shown in figure 3.18.

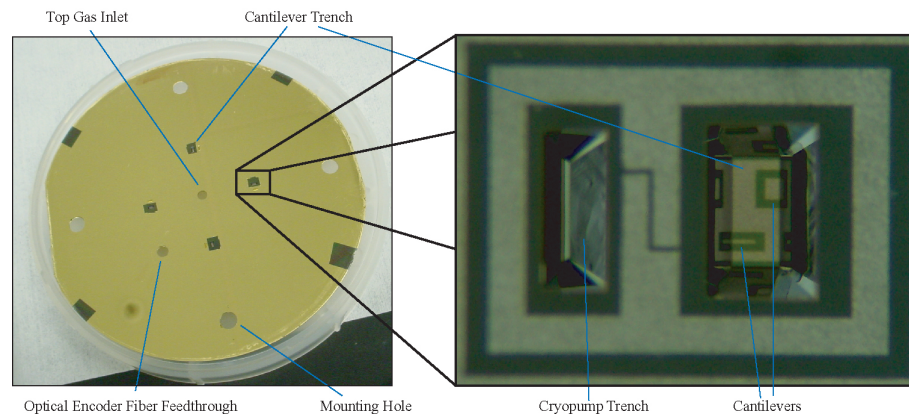


Figure 3.18: Left: a photograph of a whole cantilever wafer. All of it except the area inside the trenches has been coated with titanium-platinum-gold. Right: A close-up photograph of the cantilever trench and the cryopump trench. Reflections from the angled side wall of the cantilever trench, which are visible in the close-up, are of great help during precise positioning of test masses. Labeled parts are explained in the text.

### 3.6.3 Cantilever Displacement Detection

#### Fiber Interferometer

The cantilever's deflection is measured by a laser interferometer, based on a design by Dan Rugar's group at IBM [35]. The interferometer uses the optical cavity formed between the reflective surface of the gold and the end of the optical fiber used to inject the light. A lens inside this cavity focuses the light on the test mass; this allows the cavity to be several millimeters long, so that the optical elements can be positioned outside of the sealed cantilever trench. The sensitivity of an optical interferometer is a periodic function of  $d/\lambda$ , where  $d$  is the cavity length and  $\lambda$  is the wavelength of light being used. This long optical cavity thus also allows the interferometer to be kept at the point of maximal sensitivity by temperature controlling the laser instead of mechanically adjusting the cavity length. The necessity for a Frogland-style piezoelectric biasing element in the Fabry-Perot cavity is thus avoided; this both simplifies the design and greatly reduces susceptibility to electrical noise. This technique requires that the coherence length of the laser be long compared to the cavity. The Fabry-Perot lasers used in the Frogland experiment have coherence lengths that are too low for this purpose, so a high-coherence-length fiber-coupled distributed feedback (DFB) laser is used as a light source for the interferometer. DFB lasers increase the coherence length of emitted light by using a periodic modulation of the index of refraction in the gain medium itself to suppress extraneous modes in the lasing cavity.

Assuming the coherence length is longer than the cavity length, the optical power reflected from the Fabry-Perot cavity depends on the cantilever's position as  $P_{\text{out}} = P_{\text{o}}(1 - V \cos 4\pi d/\lambda)$ , where  $\lambda$  is the wavelength of the laser,  $d$  is the distance from the cleaved fiber end to the cantilever,  $P_{\text{o}}$  is the midpoint power, and  $V$  is the fringe visibility.[35] The laser light is injected through one arm of a fiber coupler, as shown in figure 3.23; a photodiode (UDT FCI-INGAAS-100L-FC) attached to another arm of the coupler produces a current proportional to the reflected power; this current is then converted to a voltage by a transimpedance amplifier with a 10 M $\Omega$  feedback resistor. This voltage is then acquired by the DAQ, and serves as a fast and accurate measurement of the position of the cantilever.

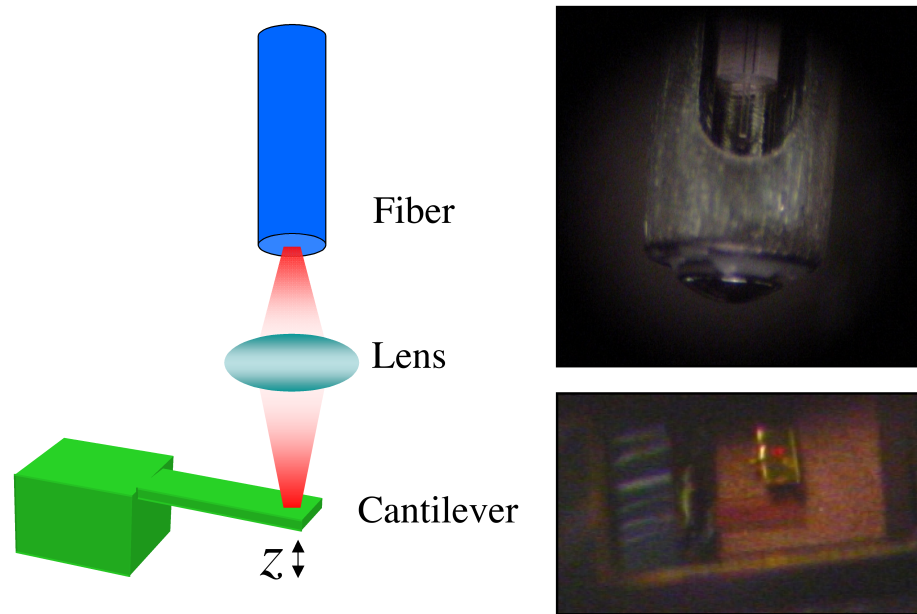


Figure 3.19: Left: a diagram of the Fabry-Perot cavity used to detect the displacement of the cantilever. Top Right: a photograph of the end of the interferometer ferrule assembly. The end of the cleaved optical fiber can be seen protruding from the glass ferrule; the fiber-focusing lens is epoxied to the end of the stainless ferrule at the bottom of the picture. Bottom Right: a view through a microscope of a visible (red) laser spot being focused through the fiber-lens system onto the test mass. Sending visible light through the fiber in this way greatly simplifies the alignment of the interferometer.

Physically, the fiber interferometer is a subset of the radiation pressure damping apparatus shown in figure 3.23. The non-free-space optical elements of the fiber interferometer are the coupler (essentially a fiber-optic beamsplitter), the photodiodes, and the wave division multiplexer used to split off the 1550 nm light used for damping. All those elements are discussed in section 3.6.5. The only free-space portion of the interferometer is the Fabry-Perot cavity itself. This cavity is pictured in figure 3.19. A stainless steel ferrule holder with four legs (not pictured) is glued to the cantilever wafer or to the glass lid of the cantilever trench. This piece maintains the perpendicularity and alignment of the fiber to the test mass as the probe is cooled to low temperatures. Clamped into the ferrule holder is a stainless steel ferrule which holds both the glass fiber ferrule and the aspheric lens used for focusing, and maintains their

relative coaxial alignment. The lens is epoxied to the end of the stainless ferrule using Torr-Seal. The glass fiber ferrule is indium-soldered to the stainless ferrule using the same Ti-Pt-Au fluxless vacuum soldering technique described in section 3.6.4.<sup>23</sup> The fiber itself is cleaved to the proper length with a commercial cleaver and then inserted into the glass ferrule, which holds the fiber so that it is coaxial with the lens. Per a suggestion from the Rugar group, small epoxy bridges between fiber and ferrule can be used to hold the fiber in the ferrule during cooldown— this may help to reduce the incidence of alignment loss at low temperatures due to fiber withdrawal.

### 3.6.4 Integrated Cantilever Vacuum System

An important design challenge in this experiment was that the gas bearing (used as a mass actuation system) and the cantilevers (used as force sensors) require radically different pressure ranges. The gas bearing exhausts helium gas into the probe space at a pressure as high as a few hundred torr, but the cantilevers in the gas bearing lid need to be in a vacuum substantially better than  $10^{-3}$  torr in order to make use of their high intrinsic quality factor. This latter condition is due to the fact that air viscosity dominates cantilever damping above about  $10^{-3}$  torr [36]. This design problem was solved by enclosing the cantilevers in a hermetically sealed cavity that was maintained at a much lower pressure than the surrounding environment of the gas bearing.

#### Sealing the Cavity

The gold-coated silicon nitride shield membrane described in section 3.6.2 forms the bottom of the sealed cavity. The sides of the cavity are the walls of the anisotropically etched trench in which the cantilevers sit. The lid of the sealed cavity must be added by hand after microfabrication; it needs to be optically transparent, in order to allow interferometric detection of the cantilever's motion. In order to provide a reasonable thermal expansion match with the silicon wafer, small discs of borosilicate

---

<sup>23</sup>The Rugar group at IBM attaches these two pieces more simply by depositing nickel and soldering normally, but we wanted to avoid using nickel or chromium films so near the cantilevers for magnetic reasons. This decision was probably excessively cautious.

glass (similar to Pyrex) were used as lids. Several techniques for hermetically sealing the lid to the wafer were tried, only one of which gave good results; a description of the successful technique follows.

Elemental indium is often used in low temperature experiments as both a gasket material and a solder, because of its low yield modulus (which mitigates thermal stresses) and low melting point (which enables simple nondestructive soldering of delicate parts). Indium-soldering the lid of the cavity thus seemed to be a good idea, especially if it could be done in vacuum to reduce residual gas in the cavity. With this in mind, a “vacuum hot plate” setup was constructed, which used a halogen bulb to heat a copper plate on which a cantilever wafer could be placed. The whole apparatus was placed in an old thermal evaporator bell jar and maintained at a pressure of  $10^{-6}$  torr by a diffusion pump. The idea was that a small gasket of indium wire would be placed around the cantilever trench, the glass lid would be pressed against the gasket with a small weight, and the whole setup would be heated above the melting point of indium ( $157^{\circ}\text{C}$ ) in order to complete the seal.

One further complication became apparent when this sealing technique was first tried. The titanium-gold coating on the wafer, which we had hoped would act as a wetting layer for the indium, was instead scavenged entirely off the surface of the wafer by the molten indium, presumably because of the formation of energetically favorable alloys like  $\text{AuIn}_2$ . This scavenging resulted in de-wetting of the indium from the exposed surface of the wafer and the lid and rendered it impossible to make a good vacuum seal. The solution to this problem was suggested by a technique proposed for use in the assembly of laser diodes [37]. Using an electron-beam evaporator with multiple targets, the wafer was coated with  $80 \text{ \AA}$  of titanium,  $100 \text{ \AA}$  of platinum, and  $1000 \text{ \AA}$  of gold, in that order.<sup>24</sup> The titanium, as before, acts as a standard wetting layer. The key to the process is the layer of platinum, which is relatively insoluble in molten indium and thus forms a barrier to the scavenging-dewetting process described above. The gold layer acts as a flux in this so-called “fluxless” process: it protects the vacuum-clean platinum surface from contamination until the

---

<sup>24</sup>To minimize expense and difficulty of evaporation, a thick layer of copper can possibly be used in place of the platinum layer. As usual, you get what you pay for: the results are noticeably better using platinum.

indium melts, at which point all the gold is quickly scavenged away and the indium is free to form a strong solder joint with the uncontaminated platinum. When a Ti-Pt-Au (or “tiptoe”) coating is applied both to the wafer and (in an annular pattern to leave a clear window) to the glass lid, the vacuum-hotplate soldering technique works perfectly and results in an excellent, robust vacuum seal.

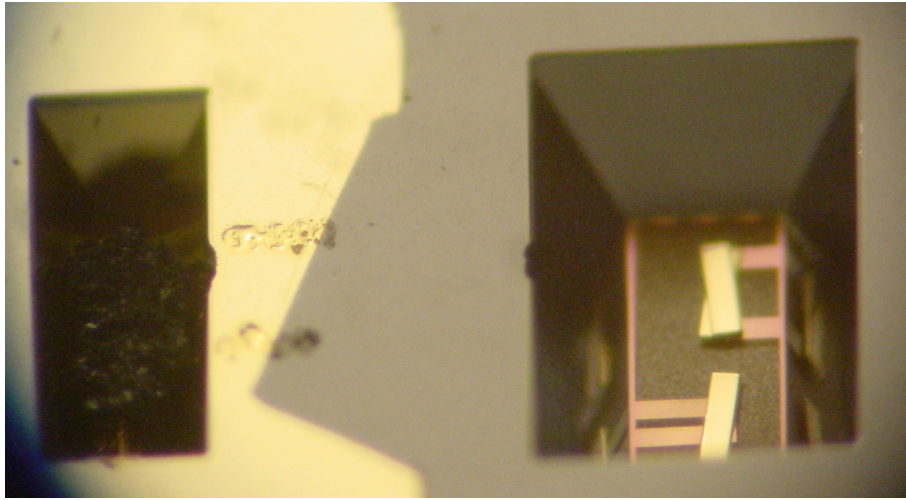


Figure 3.20: A photograph of the microfabricated cryopump. The charcoal piece is visible in the trench to the left. The two smears between the trenches are epoxy bumps, placed there to ensure that gas from the cantilever trench can get to the cryopump trench. Both cantilevers in the trench to the right have  $400\ \mu\text{m}$  masses on them.

### Pumping the Cavity

Even though the sealing of the cavity is performed at a reasonably high vacuum, the measured  $Q$  of the sealed-in cantilevers is still fairly low at room temperature (less than 100, as compared with an intrinsic  $Q$  of around 80,000). This low quality factor is a result of viscous damping by residual gases released during the soldering process that are trapped inside the cavity after the seal is made. This problem is fairly generic, and occurs to some extent with almost all sealing techniques that are commonly used for encapsulation of MEMS devices. To get around it, one needs to pump on the cavity after it is sealed. In order to do this, we built a simple

microfabricated cryopump that ensures that the residual gas pressure in the cavity will be negligible at low temperatures.

The miniature cryopump is visible in figure 3.20. A piece of activated coconut-shell charcoal is epoxied into an auxiliary trench connected to each main cantilever trench. Coconut charcoal is a wonderfully involuted substance; one gram of it has a surface area of nearly 1000 square meters, even higher than the area of an equivalent mass of molecular sieve or silica gel. This large area makes charcoal an excellent adsorbent for gas molecules; remarkably, a piece of charcoal can adsorb roughly one atom of nitrogen for every 4.5 atoms of carbon [38]. The charcoal is sealed in with the cantilevers, and the cryopump trench communicates with the cantilever trench either through a microfabricated pumping line (as in figure 3.18) or, more simply, via a gap between the lid and the wafer caused by small dabs of epoxy between the trenches (as in figure 3.20).

When the wafer is cooled to cryogenic temperatures, the charcoal, due to its vast area, cryopumps out virtually all residual gases left over from the sealing process. The cryopumping results in a very good vacuum inside the sealed cavity, and minimizes problems associated with cryodeposits forming on the cantilever itself. This encapsulated vacuum is important for maximizing the quality factor of the cantilevers and thus maximizing the overall force sensitivity of the experiment. The effectiveness of the microfabricated cryopump is illustrated in figure 3.21, which shows that the  $Q$  of the cantilever increases by nearly four orders of magnitude when the wafer is cooled to liquid helium temperatures. This increase is due largely to the removal by the cryopump of virtually all the gas that causes viscous damping of the cantilever's motion at room temperature.

### 3.6.5 Radiation Pressure Damping of the Cantilevers

#### **The Problem: High Intrinsic $Q$ Makes Resonant Excitation Difficult**

The sealed and cryopumped cantilever cavity described in the previous section led to a cantilever quality factor substantially higher than we had expected. This very high  $Q$  is good in the sense that it improves force sensitivity, but it causes an important

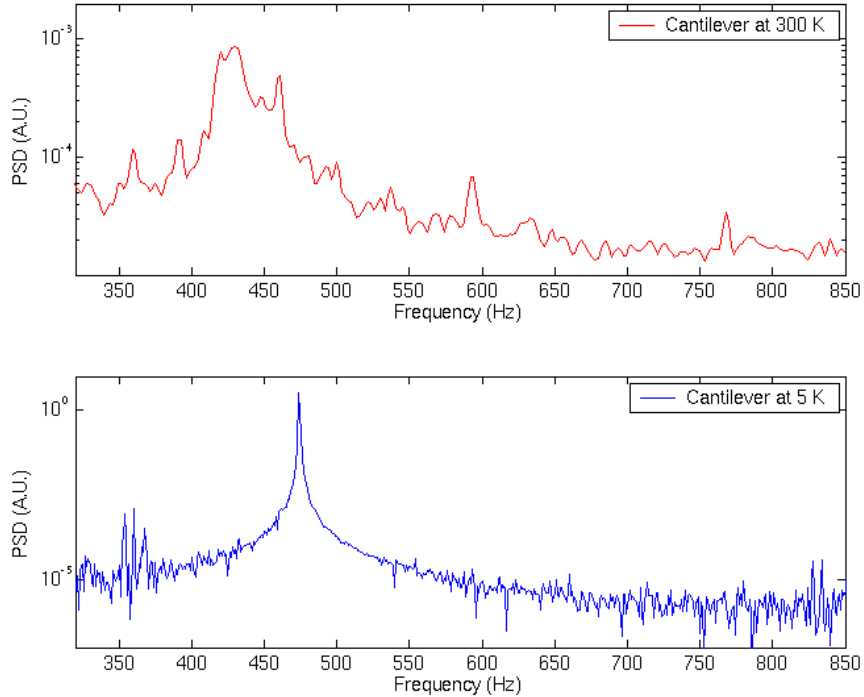


Figure 3.21: Top: thermal noise spectrum of a cantilever’s motion at room temperature. The cantilever is sealed in a cavity with a microfabricated cryopump, as described in the text. The width of this resonance corresponds to a quality factor of  $\sim 10$ . Bottom: thermal noise spectrum of the same cantilever at approximately 5 °K. The width of this much-sharper resonance corresponds to a quality factor of  $\sim 80,000$ . This very high  $Q$  illustrates the effectiveness of the cryopump, but makes it difficult to operate the rotor on resonance.

practical difficulty, which we address here. The problem is that the width of the resonance of a cantilever with a quality factor  $Q$  of 80,000 and a resonant frequency  $f_o$  of 350 Hz is equal to  $f_o/Q$ , or about 5 mHz. In order for the excitation of the cantilever due to the drive mass to take place on resonance, the excitation frequency must not wander from the resonant frequency by more than this width. Since there are 100 drive mass patterns per circumference of the drive mass disc, this means that the rotation frequency of the gas bearing rotor must be controlled to within  $(f_o/Q)/100$ , or about 50  $\mu$ Hz. Unfortunately, it is not practically possible to control

the rotation of the gas bearing with such precision. The problem is illustrated in figure 3.22, which shows both the required precision and the achievable precision of an attempt at manual control of the spin frequency, and makes it clear that it is not possible to stay on resonance with a cantilever  $Q$  of 80,000. This attempt was made before the installation of the computer-interfaced mass flow controllers, which improved the rotor frequency stability and control substantially. However, even with the mass flow controllers, spin stability of  $50 \mu\text{Hz}$  is out of reach by a factor of at least ten.

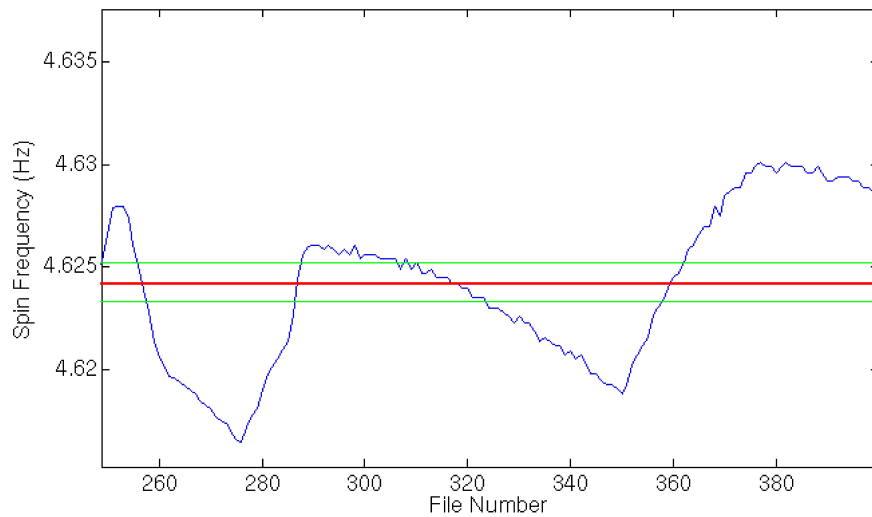


Figure 3.22: This graph represents an unsuccessful attempt to keep the rotational frequency of the rotor within the bounds imposed by the high cantilever  $Q$ . The blue line is the spin frequency, which was adjusted manually using needle valves in the spin gas flow path. The two green lines show the frequency range within which the spin would have to be controlled for a cantilever with a  $Q$  of 5,000, in order to stay on resonance. The two red lines (which look like one red line due to their close proximity) show the frequency range within which the spin would have to be controlled for a cantilever with a  $Q$  of 60,000. This latter task is not practically possible.

**The Solution: Use Feedback to Reduce  $Q$  Without Reducing Sensitivity**

The spin frequency feedback loop described in section 3.3.5 provides a necessary but not sufficient part of the solution to this problem— while it allows much finer and more accurate control of the frequency than the manual control represented in figure 3.22, it still cannot maintain or even reliably measure the frequency with an accuracy of  $50 \mu\text{Hz}$ . The second part of the solution to this problem, then, is to reduce the  $Q$  of the cantilever, ideally without compromising the good force sensitivity that is a result of the high intrinsic  $Q$ . This can be done by feeding back a phase-shifted version of the cantilever's displacement to the cantilever as a force. If the phase is properly chosen, the force emulates a viscous damping, and reduces the effective  $Q$  and the effective temperature  $T$  in such a way as to keep the signal to noise ratio constant (for measurements that are limited by thermal noise). This kind of feedback loop is sometimes implemented using a piezoelectric element, photothermal effects, or magnetic coatings to apply the force; in our case, none of those techniques were ideal. The integrated structure of the experiment, with the cantilever wafer being used as the lid of the gas bearing, prevented us from applying force by moving the wafer with a piezo. As for photothermal forces, they typically require addition of a metallic layer to the cantilever, which greatly reduces the intrinsic  $Q$ . Finally, magnetic coatings are both difficult to control and often highly undesirable in precision force measurements. In order to solve this problem, we developed a simple method for feedback-regulation of the response of a microcantilever using the radiation pressure of a laser [39]; in this method, the momentum of laser photons is used to apply the necessary force to the cantilever. That method is described in the following pages.

**The Apparatus: Radiation Pressure Damping Setup**

*This section is adapted from our paper on the same subject, which was published in Applied Physics Letters [39].*

In order to realize a setup for using radiation pressure to control the  $Q$  of the cantilever, the fiber-optic interferometer was modified so that it uses one laser to read out the position of the cantilever and another laser of a different wavelength to

apply a force that is a phase-shifted function of that position. The method does not require a high-finesse cavity, and the feedback force is due solely to the momentum of the photons in the second laser, not to photothermal effects. The feedback phase can be adjusted to increase or decrease the cantilever's effective quality factor  $Q_{\text{eff}}$  and effective temperature  $T_{\text{eff}}$ . At room temperature, we demonstrated a reduction of both  $Q_{\text{eff}}$  and  $T_{\text{eff}}$  of our silicon nitride cantilever by more than a factor of 15 using a root-mean-square optical power variation of  $\sim 2 \mu\text{W}$ . This work also suggested a method for determination of the spring constant of a cantilever using the known force exerted on it by radiation pressure that might be of interest for other cantilever-based force-detection experiments, like atomic force microscopes.

For our own application as well as many others, it is useful to be able to control the effective quality factor  $Q_{\text{eff}}$  and temperature  $T_{\text{eff}}$  of a micromachined cantilever. A system that phase-shifts the cantilever's own thermal fluctuations and feeds them back to the cantilever as force has been shown to be capable of both increasing [40] and decreasing [41] the effective quality factor and temperature, as well as modifying the effective spring constant.[42] For scanning probe force microscopes,  $Q$ -modification of both signs can be useful. For general cantilever-based force-detection experiments, reduction of  $Q_{\text{eff}}$  and  $T_{\text{eff}}$  can improve experimental convenience without sacrificing high force sensitivity.[19] The force that is fed back to the cantilever can be of any type; previously, this force has most often been applied using piezoelectric elements,[19] magnetic coatings,[40] or the photothermal forces that result from bimorph-type cantilevers being locally heated by a laser.[41]

Here we discuss a new method, that of using radiation pressure to apply the feedback force. This scheme is simple and robust; it has similar effectiveness to existing methods, but has the advantage of not requiring that the cantilever be modified by addition of a metallic coating or piezoelectric stack. It is especially easy to add this capability to systems that read out cantilever position optically, since it can make use of the same focusing and alignment optics. Radiation pressure has previously been used to actuate micromechanical oscillators in several experiments. Marti *et al.* performed an early experiment investigating the mechanical effects of radiation pressure on micromachined cantilevers.[43] A high-sensitivity atomic force microscope has

been developed for biological applications that uses optical radiation pressure to control the position (but not the quality factor) of a force-sensing cantilever in liquid.[42] Acoustic radiation pressure has been shown to be an effective tool for actuation and characterization of microcantilevers in fluids.[44] At larger length scales, an elegant proof-of-principle experiment designed to test the technology for gravity-wave interferometers showed that radiation pressure can be used to control the oscillations of a macroscopic mirror.[45] Our method modestly extends the results of those experiments by demonstrating a simple method of controlling the quality factor and temperature of a microcantilever using only optical radiation pressure.

In general, the displacement  $x$  of a damped harmonic oscillator as a function of frequency  $\omega$  is

$$x(\omega) = \frac{\omega_o^2/k}{\omega_o^2 - \omega^2 + i\Gamma\omega} [F_{\text{thermal}}(\omega) + F_{\text{ext}}(\omega)], \quad (3.2)$$

where  $k$  is the spring constant,  $\omega_o$  is the resonant frequency, and  $\Gamma = \omega_o/Q_o$  is the intrinsic damping of the oscillator. Here,  $F_{\text{thermal}}(\omega)$  represents the random thermal Langevin force and  $F_{\text{ext}}(\omega)$  an externally applied force, which in this case is due to radiation pressure. The applied force can be modulated by a feedback loop whose input is the measured displacement. Adjusting the phase of the feedback gain at the resonant frequency to  $\pi/2$  has the effect of producing a velocity-dependent force at the resonant frequency. In particular, if the gain is chosen so that the applied force near resonance is  $F_{\text{ext}} = -im\omega gx$ , where  $m$  is the mass of the oscillator and  $g$  is proportional to the magnitude of the feedback gain on resonance, then the displacement as a function of frequency becomes

$$x'(\omega) = \frac{\omega_o^2/k}{\omega_o^2 - \omega^2 + i[\Gamma + g]\omega} [F_{\text{thermal}}(\omega)]. \quad (3.3)$$

Assuming that the noise of the feedback system can be neglected, the feedback thus changes the damping of the system without adding fluctuations. This changed damping leads to a changed effective quality factor  $Q_{\text{eff}} = \omega_o/[\Gamma + g]$  and a changed effective temperature  $T_{\text{eff}} = T_o\Gamma/[\Gamma + g]$ , where  $T_o$  is the temperature of the oscillator's environment.[45] A positive  $g$  lowers both  $Q$  and  $T$  by the same factor.

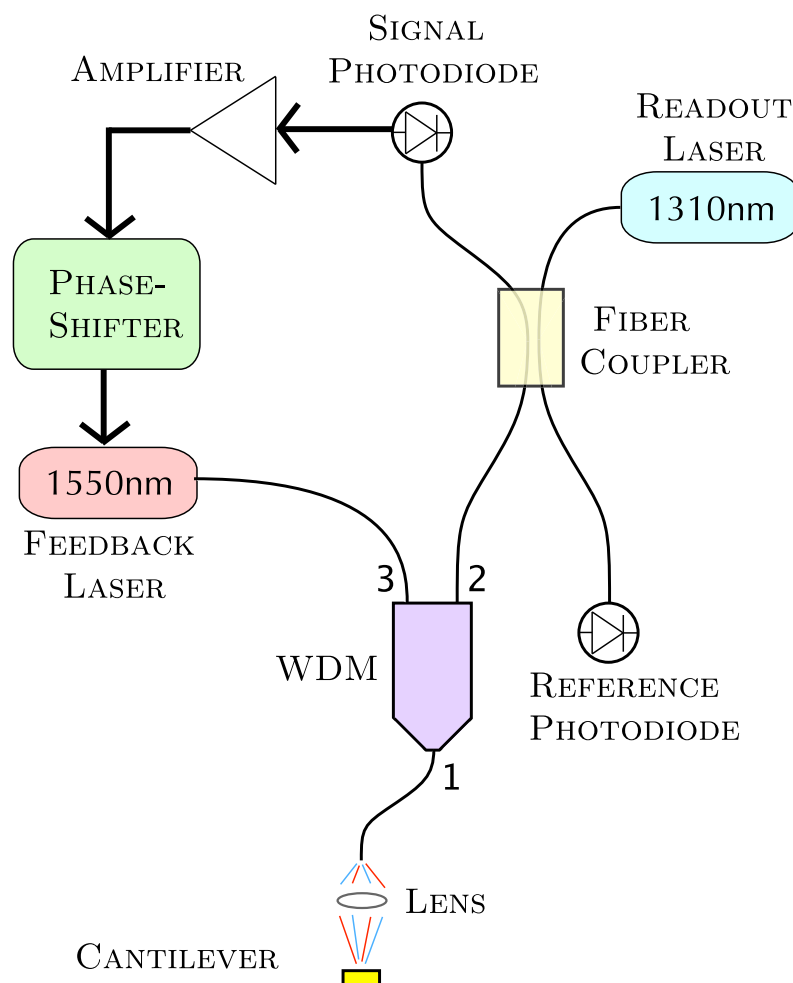


Figure 3.23: Diagram of the radiation pressure damping system; see text for details. The wave division multiplexer (WDM) allows 1550 nm light to pass only between ports 1 and 3, and allows 1310 nm light to pass only between ports 1 and 2.

The apparatus used for demonstrating feedback cooling of a cantilever with radiation pressure is depicted in figure 3.23. It consists of a modified fiber-optic interferometer of a type first proposed by Rugar *et al.*, [35] and discussed at greater length in section 3.6.3. A 0.5 mW 1310 nm distributed-feedback diode laser (PD-LD PL13U0.51FAB-T-1-01) injects light into a single-mode optical fiber (Thorlabs 1060XP). The light travels through a standard 99/1 fiber coupler and into the “blue” arm of a cascaded wave division multiplexer ( $2\times$  JDSU FFW-4C6P1103), then exits

the fiber through a flat cleave and is focused by an aspheric lens (Lightpath 350450C) onto a gold mass on a microcantilever. The reflected light from the cantilever interferes with the reflected light from the cleaved end of the fiber, resulting in a reflected power that depends periodically on the cantilever's position. The reflected power is converted to a current by a photodiode, and then to a voltage by a transimpedance amplifier. This voltage is phase-shifted by a custom-built analog circuit and used to modulate the power of a 1.5 mW 1550 nm diode laser (Thorlabs S1FC1550). Because photon momentum can only apply force in one direction, it is necessary to add a constant offset to the power so that the force modulation can be of either sign. The light from the 1550 nm laser is added to the fiber by coupling through the "red" arm of the wave division multiplexer (WDM); it then follows the same optical path as the 1310 nm laser, and is focused onto the cantilever by the same optics. The width of the focal spot is about 10  $\mu\text{m}$ : much smaller than the width of the cantilever crossbar. This small spot makes it easy to align the lens so that all the light from the laser hits the cantilever. In practice, alignment is achieved by temporarily replacing the 1550 nm laser with a visible laser and observing the focused spot on the cantilever through a microscope. The WDM prevents backscattered 1550 nm light from getting to the readout photodiode; its attenuation factor is measured to be greater than 50 000.

The large mass attached to the cantilever for the purpose of measuring mass-dependent forces is not, of course, essential for radiation pressure damping. It is, however, convenient, not only because it provides a good reflecting surface, but also because it pushes the thermal time constant up to several seconds (see appendix B). This long thermal time constant virtually eliminates photothermal effects and Knudsen forces[46] at the resonant frequency. The intrinsic quality factor  $Q_o$  of the cantilever is  $\sim 12\,000$  at  $10^{-6}$  torr and  $300^\circ\text{K}$ , and, as mentioned earlier, it can be as high as 80 000 at  $5^\circ\text{K}$ .

The radiation force exerted on a perfectly reflecting surface by a light beam of power  $\mathbf{P}$  is  $F_{\text{rad}} = 2\mathbf{P}/c$ , where  $c$  is the speed of light. To measure the force applied by radiation pressure, the power of the laser was sinusoidally modulated and the cantilever displacement was recorded as a function of the amplitude of this modulation.

Figure 3.24 shows the results of such an experiment. The laser power was modulated at the cantilever's resonant frequency  $f_o \simeq 350$  Hz so that the motion would be amplified by a factor of  $Q_{\text{eff}}$ , which was maintained at a value of 2700 using feedback. Photothermal forces on the cantilever are not only too slow to have measurable effects at this frequency, but also happened to be of opposite sign from radiation pressure in this case. The sign and magnitude of the results are consistent with what would be expected from actuation due only to radiation pressure. The inferred spring constant is slightly smaller than expected; this is due to the fact that the laser was focused at a point farther out along the cantilever than the center of the gold mass. The measured value of  $k$  will have a strong dependence on the exact position of the laser spot on the cantilever; [47] this position would need to be well characterized for a  $k$ -measurement using this technique to be accurate. Still, since the applied force depends only upon easily measurable quantities (cantilever reflectivity and optical power), this method could furnish one useful solution to the much-discussed problem of accurately measuring the spring constant of a microcantilever. The same experiment can also be performed at a frequency below  $\omega_o$ , in which case the (known) applied force divided by the (measured) amplitude of motion directly gives the spring constant  $k$  of the cantilever without requiring knowledge of  $Q$ .

The factor by which  $T$  and  $Q$  are reduced by feedback is proportional to the gain factor  $g$  defined earlier. The maximum value of  $g$  that can be attained using a laser with a maximum rms power modulation amplitude  $\langle \mathbf{P}_{\text{mod}} \rangle$  is

$$g = \frac{2\langle \mathbf{P}_{\text{mod}} \rangle \omega_o}{ck\langle x \rangle} = \frac{2\langle \mathbf{P}_{\text{mod}} \rangle \omega_o}{c\sqrt{kk_B T_o}}, \quad (3.4)$$

where we have used the equipartition theorem to write the root-mean-square cantilever position  $\langle x \rangle$  in terms of temperature  $T_o$ . It should be noted that at low temperatures, because the position fluctuations are smaller, less laser power is needed to achieve a given  $g$  (this is true only if the vibrations of the cantilever are dominated by thermal noise). For the damping experiment described here, which was done at room temperature using a maximum  $\langle \mathbf{P}_{\text{mod}} \rangle$  of 2  $\mu\text{W}$ , the maximum value of  $g$  was 4.0  $s^{-1}$ , corresponding to a possible reduction in  $Q$  and  $T$  by a factor of  $\sim 20$ .

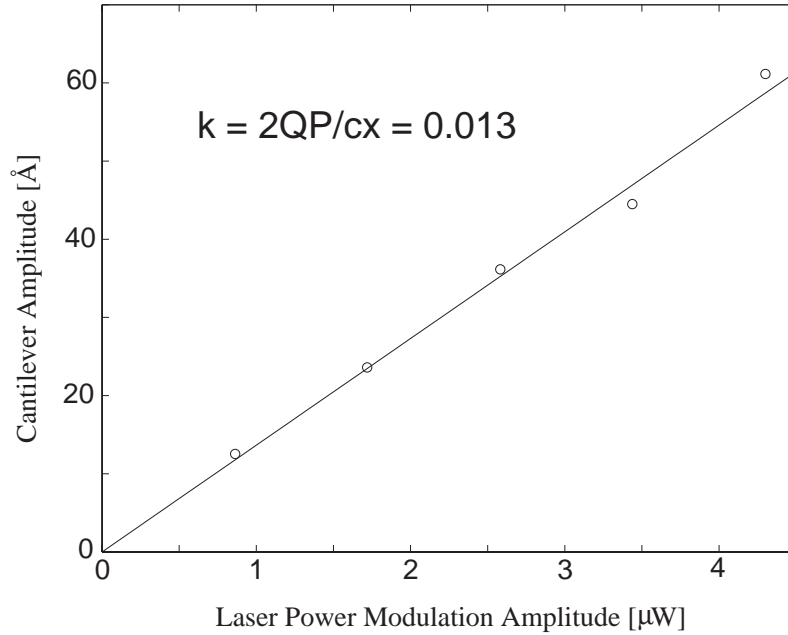


Figure 3.24: Cantilever displacement versus laser power (AC measurement). The solid line is a fit to the data that indicates a spring constant of 0.013.

Results of the feedback-modification of  $Q$  and  $T$  are presented in figure 3.25, which shows the broadening and flattening of the thermally excited resonance peak with increasing feedback gain. The individual spectra were each fitted with a Lorentzian function to extract the value of  $Q_{\text{eff}}$ . The effective temperature  $T_{\text{eff}}$  was determined by integration of the power spectral density. Analysis of the lower-leftmost curve shows that the effective temperature of the cantilever was reduced to 18°K, and its quality factor was reduced to  $\sim 700$ . The measured variation of  $Q_{\text{eff}}$  and  $T_{\text{eff}}$  with gain is shown in the inset of figure 3.25, along with the theoretical prediction. The agreement with theory at lower gains is excellent. At higher gains, the performance of the feedback system becomes less ideal; this effect seems to be due to the increased importance of amplifier noise, in both the position detection and feedback amplifiers. The maximum reduction factor achievable using this technique will likely be limited either by noise in the feedback amplifier or by cantilever heating due to the damping laser.

The technique discussed above is a simple and robust method for controlling the

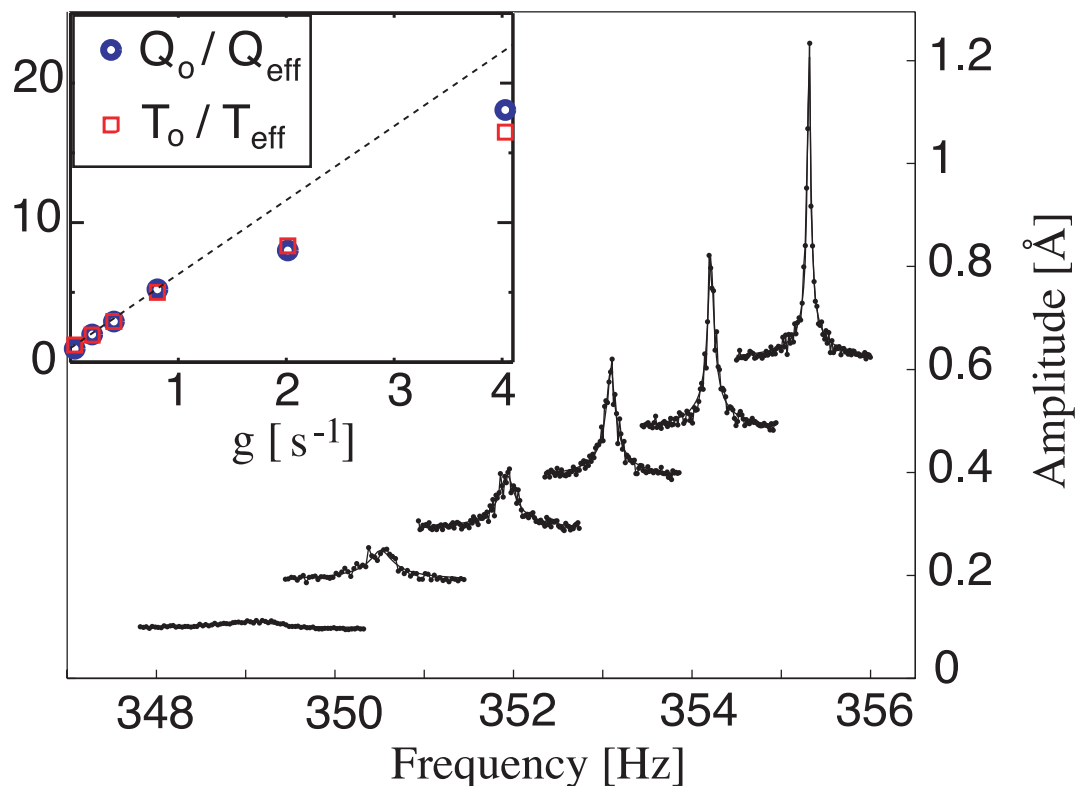


Figure 3.25: Cantilever displacement spectra taken at different feedback gains. Gain increases from upper right to lower left. Peaks have been offset in  $x$  and  $y$  for clarity. Inset:  $Q_o/Q_{\text{eff}}$  (circles) and  $T_o/T_{\text{eff}}$  (squares) versus gain factor  $g$ , for the same data. The dashed line is the theoretical prediction.

effective quality factor and temperature of a cantilever using the radiation pressure of a laser. Using this method, we have demonstrated a reduction in both  $T_{\text{eff}}$  and  $Q_{\text{eff}}$  by a factor of more than 15. This reduction is enough to make resonant excitation of a cantilever with the gas bearing rotor possible—the “problem” of high intrinsic  $Q$  is thus solved, without sacrificing force sensitivity.

## 3.7 Force Detection

The force detection system has two physical parts, both discussed earlier in this chapter: the cantilever interferometer and the optical encoder. Signals from both instruments are sampled simultaneously by the data acquisition system and analyzed to determine the force between the masses.

### 3.7.1 Data Acquisition

The signals from the interferometer and the encoder are simultaneously sampled and stored at 10 KHz using a PC-based DAQ system. The system uses a National Instruments DAQ card to convert analog voltages from the instruments into digital waveforms. These waveforms are manipulated and displayed by a custom-made program running in the MATLAB scripting environment. The program (lyrically titled “DataTaker3”) handles several different aspects of the experiment. It determines the rotor frequency, runs the PID loop to control that frequency, and outputs the necessary commands to the mass flow controllers. That feedback loop is described in more detail in section 3.3.5 and illustrated in figure 3.8. Besides the two main data streams from the interferometer and the encoder, the DataTaker3 program also separately records and displays the temperatures of the gas bearing, the inner vacuum can, and the interferometer’s laser, the mean peak value of the encoder signal (a measure of the rotor’s  $z$ -position), and the DC level of the interferometer voltage. A screenshot of the user interface of DataTaker3 can be seen in figure 3.9. After the real-time analysis and display are complete, all these signals are recorded to disk in a compressed MATLAB-readable format for later processing.

The recorded encoder signal can then be used to bin the recorder interferometer signal and perform a boxcar average over many cycles. The signal from any force on the test mass that is *not* coherent in phase and frequency with the density modulation underneath it will be averaged out by this process. This averaging procedure, which we used to good effect in our previous gravity experiment [3], is similar to a lock-in-based measurement, and has the same main advantage: excellent rejection of thermal noise and other spurious non-phase-coherent signals. The binning and averaging

procedure is described in more detail in section 4.1.1. Finite-element calculations are performed to determine the predicted force signal for Newtonian interactions and for an array of Yukawa-parameterized non-Newtonian interactions. The observed force signal is then compared with these predicted force signals to place limits on possible deviations from Newtonian gravity.

# Chapter 4

## Data Analysis

In this chapter, we will first discuss some of the techniques used to extract a measured force from the signals acquired by the data acquisition system.

### 4.1 Data Analysis

#### 4.1.1 Averaging procedure

There are two main data streams in the experiment: the interferometer waveform and the encoder waveform. The goal of the averaging procedure is to extract correlations between these two data streams, which represent the test mass position versus time and the drive mass position versus time, respectively. This could in principle be done nearly real-time, while the experiment is running, but it is likely that this would require a second computer (see appendix E for discussion of this and other suggested upgrades). In practice, the somewhat time-consuming averaging analysis has been performed the morning after each long experimental run. This limits the ability of the experimenter to make adjustments to the experimental parameters to minimize the noise.

Both data streams are recorded simultaneously by the data acquisition system and saved to disk in files that are around 60 seconds in length, along with various other measurements of system parameters like temperatures and flow rates. The

data analysis software loads the two main waveforms from each saved data file, breaks them up into smaller chunks, and processes each chunk to extract position-versus-time curves for the test mass and drive mass. The drive mass waveform for each chunk is subjected to a zero-crossing analysis that determines the rotational frequency of the drive mass, and thus the frequency at which the cantilever would be excited by any real force from the drive mass. The test mass waveform for each chunk is then fourier transformed, and the amplitude and relative phase of the cantilever's oscillations *at that excited frequency* are determined. As in a lock-in type measurement, the phase information is crucial, since it enables good noise rejection; the procedure of measuring the relative phases of the signals is discussed at length in the next section.

This entire averaging procedure is very similar to the procedure we developed for use in the Frogland experiment. In that experiment, several different averaging techniques were tried out, but they all ended up being essentially equivalent to one another. The one we have implemented here is the least computationally intensive approach, due to the fact that it makes use of MATLAB's implementation of the miraculous Cooley-Tukey FFT Algorithm [48] instead of more intuitive but laborious boxcar averaging procedures.

One important parameter of such an analysis is the length of the chunks into which the data is divided before the FFT is performed. We chose, in general, to use chunk sizes that corresponded to about three coherence times of the damped cantilever (or about 15 seconds)—this length was small enough to give us many chunks and thus good number statistics, but still large enough so that each chunk was statistically independent.

Any random-phase correlations between the drive mass and test mass positions will be averaged out by this process, and their amplitude will in the usual way decrease as the inverse root of the averaging time. Any correlation between the positions that is constant in phase (and is thus not suppressed by the phase-correlated averaging process) presumably represents the influence of a real force coupling the drive mass rotation to the test mass oscillation—this is the sort of coupling that the experiment is designed to detect or constrain. The trickiest part of this procedure, oddly enough, is the determination of the relative phase between the drive mass and the test mass;

that is the subject of the next section.

### 4.1.2 Phase determination

An important feature of this apparatus is that it has the ability to determine not only the amplitude but also the phase of a measured force between the drive mass and the test mass. This capability is very useful— it allows us to distinguish between attractive and repulsive forces, and to identify the presence of certain magnetic forces that appear at other phases (on which more later). In order to determine the phase of any measured force, the fixed relative phase between the encoder pattern and the mass pattern must be known. The two patterns must therefore be aligned carefully, and the resulting relative phase must be well-measured. The alignment setup and

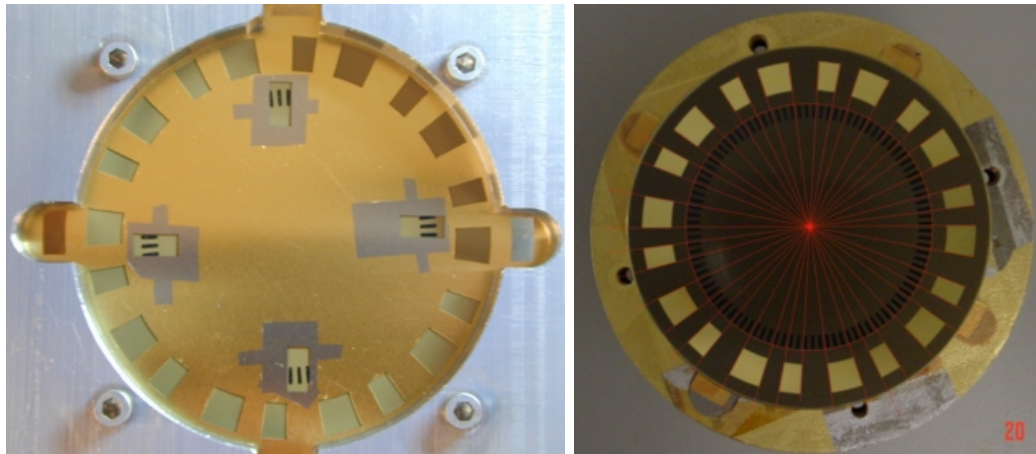


Figure 4.1: **Left:** The shadowmask and holder used to align the encoder pattern with the mass pattern. **Right:** The resulting alignment on the same drive mass. Red lines are added to the photograph in order to assist in measurement of relative phase.

measurement are shown in figure 4.1. In order to align the two patterns to each other, a custom-made shadowmask-clamp assembly (figure 4.1, Left) is used to fix the drive mass in such a way that the mass pattern is aligned with the windows in the mask that will produce the encoder pattern. Titanium and Gold are then deposited through that shadowmask to form the encoder pattern; continuous rotation of the drive mass during deposition is employed to ensure rotational symmetry of the

metal distribution. After deposition of the encoder pattern but *before* deposition of the opaque gold shield layer visible in figure 3.12, the drive mass is photographed so that the phase alignment between the two patterns can be measured and confirmed (figure 4.1, Right).

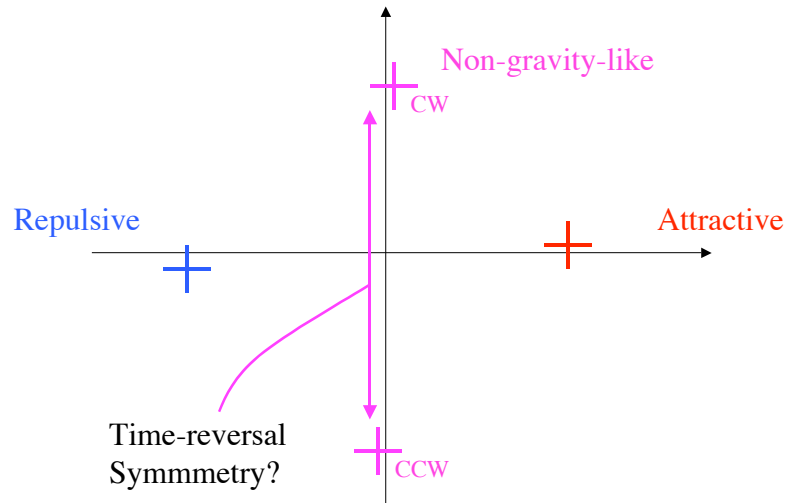


Figure 4.2: A simple illustration of the meaning of the axes on a typical data plot produced by the analysis described in this chapter. The positive real axis corresponds to a purely attractive force, and so on. Time-reversal symmetry breaking will result in different measured forces for CW and CCW runs under otherwise identical experimental conditions.

Once the relative phase between the encoder pattern and the mass pattern is known, a series of transformations can be applied to the encoder waveform and the cantilever displacement waveform to determine the phase of the measured force relative to the phase that would be expected from an attractive mass-dependent force like Newtonian gravity. The phase alignment between the mass pattern and encoder pattern depicted in figure 4.1 is used to derive from the encoder waveform (figure 4.3, blue) the force as a function of time that would be put on the cantilever by an attractive, mass-dependent interaction (figure 4.3, red). That force is then Fourier

transformed and put through the complex mechanical transfer function of the cantilever, which in frequency space is of the form

$$G(f) = \frac{f_o^2/k}{(f_o^2 - f^2) + i(ff_o/Q)}, \quad (4.1)$$

where  $f$  is frequency,  $k$  is the spring constant of the cantilever,  $f_o$  is the resonant frequency of the cantilever,  $Q$  is the quality factor of the cantilever, and  $i$  is  $\sqrt{-1}$ .  $Q$  and  $f_o$  are determined by real-time Lorentzian fitting of the cantilever's resonance peak. After being put through this function, the force signal is inverse-Fourier-transformed to yield the cantilever displacement versus time that would be expected from a purely attractive force (figure 4.3, black). The phase of this signal represents the phase expected from an attractive force. The cantilever displacement measured by the interferometer is then itself Fourier transformed, and the component at the excitation frequency is recorded. This component has both an amplitude and a phase. The amplitude represents the amplitude of the measured force at the excitation frequency for this data file. The phase can be compared to the attractive-force phase that was determined earlier. This comparison determines whether the measured signal is attractive, repulsive, or somewhere in between.

The end result of this analysis procedure for each chunk of data is one point on the complex plane, representing the amplitude and phase (relative to Newtonian gravity) of the measured force. For a graphical explanation of the meaning of the axes, see figure 4.2. When many chunks of data are taken in a row, they form a distribution on the plane like that visible in figure 6.3. The mean and standard deviation (divided by the square root of the number of points) of that distribution are then the measured force and the statistical error for that particular run.

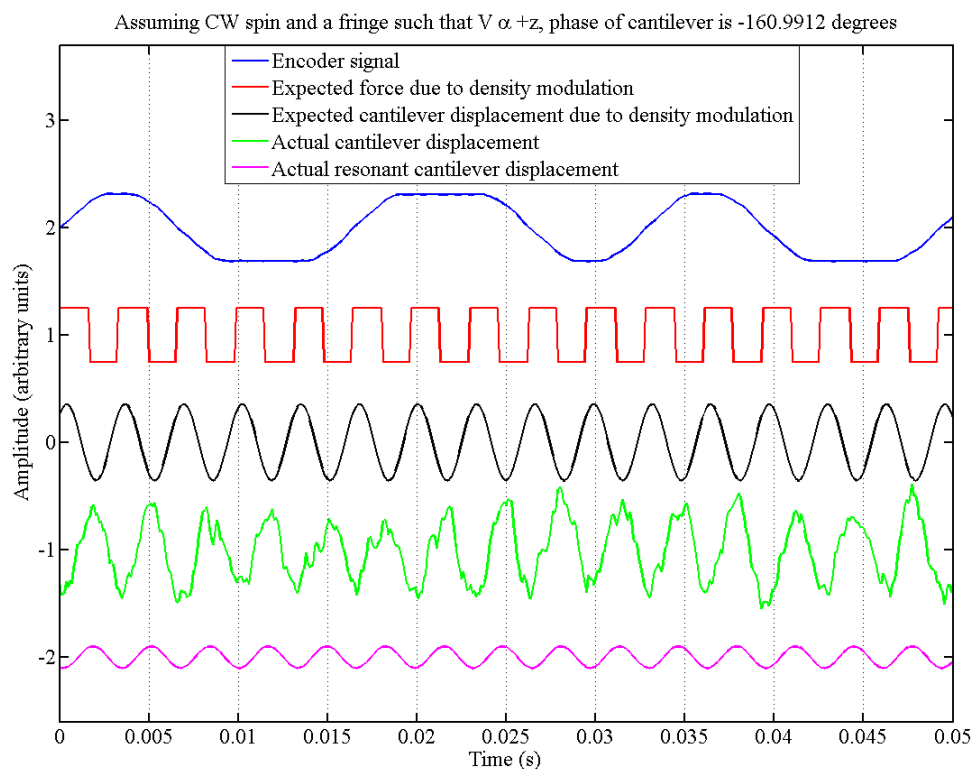


Figure 4.3: A plot of the steps used to determine the phase of the measured force, relative to the phase expected from an attractive mass-dependent force. The blue line is the signal from the optical encoder. The red line (calculated from the blue line and a knowledge of the relative phase of the two patterns on the drive mass) is the density modulation passing under the cantilever. The black line is that density modulation put through the complex mechanical transfer function of the cantilever, and thus represents the expected cantilever displacement due to an attractive mass-dependent force. The green line is the measured cantilever displacement. The pink line is the on-resonance Fourier component of 15 seconds of measured cantilever displacement data. The phase difference between the black line and the pink line thus represents the phase of the measured force relative to that of an attractive force. The first four traces are arbitrarily normalized; the last trace is in the same units as the fourth, to show the effect of 15 seconds of averaging. This graph represents the data from one randomly-chosen 15-second file; results from many such files (with, in general, a wide range of measured phases) are averaged together to provide a meaningful force measurement.

# Chapter 5

## Uncertainties, Backgrounds, and Noise

In this chapter we will discuss experimental uncertainties and mention various possible sources of background forces and experimental noise. We will then show data that help elucidate their relative magnitudes. Currently the sensitivity of the experiment is limited by vibrational noise.

### 5.1 Experimental Uncertainties

#### 5.1.1 Uncertainties in mass separation distance

One of the most important experimental parameters in any Yukawa force measurement is the separation distance between the masses. In this experiment, that distance is the sum of nine smaller distances, eight of which are fixed by construction. The ninth is the distance between the top of the drive mass and the bottom of the cantilever wafer, which is variable. Table 5.1 presents a summary of the estimated uncertainties in each component of the total drive mass to test mass separation.

The distances in table 5.1 were measured in several different ways. The shield thickness, cantilever thickness, and cantilever-shield separation were fixed during fabrication of the cantilever wafer and measured using ellipsometry. The cantilever-shield

Distance	Value ( $\mu\text{m}$ )	Error ( $\mu\text{m}$ )
Thickness of planarization epoxy	0.5	0.5
Thickness of gold shield layer on drive mass	0.4	0.1
Distance between rotor and wafer	10–20	2
Thickness of gold shield layer on wafer	0.4	0.1
Thickness of silicon nitride shield	4	0.2
Distance between shield and cantilever	14	0.1
Droop of cantilever	-4	1
Thickness of cantilever	0.33	0.01
Cantilever-test mass separation	0	1
Total (for 15 $\mu\text{m}$ rotor-wafer separation)	30.6	2.5

Table 5.1: Table of estimated uncertainties in the determination of the face-to-face separation distance between drive mass and test mass. The cantilever droop is negative because it decreases the distance between the masses. Errors are added in quadrature.

separation was also confirmed optically. The thickness of the two gold layers was measured by a crystal rate monitor during deposition. The droop of the cantilever in the earth’s gravitational field is easily calculated and was confirmed optically. The cantilever-test mass separation was measured optically. The thickness of the planarization epoxy layer was calculated [31] and confirmed with an Alphastep profilometer. Our method for measurement of the variable distance between the drive mass and the cantilever wafer is described in section 3.3.4 and depicted in figure 3.7.

### 5.1.2 Uncertainties in the force calibration

The force on the test mass is inferred from the interferometer voltage using the following relation:

$$F = \frac{k \lambda}{2\pi Q V_{\text{pp}}} V_{\text{intf}},$$

were  $F$  is force,  $k$  is the cantilever spring constant,  $\lambda$  is the wavelength of the laser,  $Q$  is the cantilever’s quality factor,  $V_{\text{pp}}$  is the fringe height (after the preamplifier), and  $V_{\text{intf}}$  is the measured interferometer voltage. Table 5.2 presents typical values and uncertainties for these parameters.

Quantity	Typical Value	Error
Quality factor $Q$ (during feedback)	5000	10%
Spring constant $k$ (N/m)	0.04	15%
Laser wavelength $\lambda$ (nm)	1310	0.1%
Fringe height $V_{pp}$ (V)	0.72	5%
Interferometer voltage $V_{intf}$ (V)	varies	2%
Total error		19%

Table 5.2: Table of estimated uncertainties in the voltage-to-force calibration. Percent errors are added in quadrature.

### 5.1.3 Uncertainties in the mass dimensions and densities

Any Cavendish-type measurement depends upon knowledge of the density and dimensions of both drive mass and test mass. Typical values and uncertainties for those parameters are presented in table 5.3.

Quantity	Typical Value	Error
Test mass density ( $\text{kg}/\text{m}^3$ )	19300	3%
Drive mass differential density ( $\text{kg}/\text{m}^3$ )	6200	3%
Test mass width ( $\mu\text{m}$ )	100	3%
Test mass length ( $\mu\text{m}$ )	400	3%
Total test mass depth ( $\mu\text{m}$ )	40	15%
Drive mass depth ( $\mu\text{m}$ )	1000	10%

Table 5.3: Table of estimated uncertainties in important properties of the drive mass and test mass. Drive mass width and length are not presented because they do not have an important effect on the ultimate determination of the force (the area of overlap between the two masses is determined by the much smaller test mass area).

### 5.1.4 Uncertainties in the determination of $\alpha$

Bounds in  $\alpha$ - $\lambda$  space on non-Newtonian interactions are derived from the measured force by calculating the value of  $\alpha$  that would produce that force at each  $\lambda$ , given the experimental geometry. Errors in this procedure can be estimated using an approximate expression for the Yukawa force between two parallel plates, which our

experimental geometry closely resembles. That expression is

$$F_{\text{yukawa}} = 2\pi G \alpha \rho_{\text{dm}} \rho_{\text{tm}} A \lambda^2 e^{-d/\lambda} (1 - e^{-t_{\text{tm}}/\lambda})(1 - e^{-t_{\text{dm}}/\lambda}),$$

where  $\alpha$  is the strength of the Yukawa force,  $\lambda$  is its range,  $F_{\text{yukawa}}$  is the force,  $G$  is Newton's constant,  $\rho_{\text{dm}}$  and  $\rho_{\text{tm}}$  are the densities of the drive mass and test mass respectively,  $A$  is the overlapping area of the plates,  $d$  is the face-to-face separation between them, and  $t_{\text{tm}}$  and  $t_{\text{dm}}$  are the thicknesses of the test mass and drive mass, respectively. Uncertainties in  $d$ ,  $F$ , and the mass dimensions and densities are discussed above in tables 5.1, 5.2, and 5.3. Those errors can be propagated through the equation above to calculate the uncertainty in the calculation of  $\alpha$  for different values of  $\lambda$ . The results are shown in table 5.4.

$\lambda$ ( $\mu\text{m}$ )	Error in $\alpha$ (%)
1000	25.4
300	24.4
100	23.5
30	22.2
10	28.3
3	74.4

Table 5.4: Table of estimated uncertainties in the calculation of  $\alpha$  for several different values of  $\lambda$ .

## 5.2 Sources of Background Forces

Because of the extreme weakness of Newtonian gravity, the amplitudes of most of the possible background forces in this experiment are normally much larger than the signals the experiment is designed to detect. This circumstance forced us to work to eliminate several different kinds of background forces. Most non-magnetic forces are eliminated either “by construction” or using the phase-sensitivity of the lock-in-type measurement. Magnetic forces are trickier, and will be discussed separately in section 5.2.2.

### 5.2.1 Non-magnetic forces

The main candidates for background forces, Casimir and electrostatic interactions, are eliminated “by construction.” As discussed in chapter 3, the two separate layers of gold shielding between test mass and drive mass should entirely eliminate Casimir forces and should greatly reduce electrostatic forces at the period of the mass pattern. In addition, our use of a phase-sensitive AC “lock-in” type measurement offers good protection against backgrounds that are uncorrelated with the density modulation in the drive mass (e.g. from random charges distributed on the drive mass surface). Corrugation in the drive mass, however, could lead to a spurious force by causing pressure variations that move the shield at a constant phase with respect to the moving mass pattern. The danger represented by such corrugations is the reason that the construction of the drive mass must be done with such care (and was one of the most difficult parts of the experiment). Other gravitational interactions (e.g. the earth’s gravity or the changing mass of lake Lagunita) are completely eliminated by the AC lock-in-type measurement since they are not at all phase-correlated with the drive mass pattern. The most important possible source of background forces is probably magnetic interactions, which are discussed in detail below.

### 5.2.2 Magnetic forces

In the presence of a static magnetic field  $B_o$  (possibly due to the earth’s field or to trapped flux in the lead bag), a drive mass with magnetic susceptibility variation corresponding to the density variation can produce a spurious force. This force would be particularly large in the case of a superconducting drive mass, since one would then expect a very large susceptibility difference between the dense (superconducting) and light (normal) regions. See figure 3.14 for evidence of superconductivity in the brass drive mass, and figure 5.1 for an illustration of the proposed situation. As the gold test mass passes through the varying magnetic field, it experiences a time-dependent magnetic flux, which causes a non-curl-free electric field due to Faraday’s law. This field causes circulating eddy currents in the test mass. These eddy currents in turn couple to the magnetic field, resulting in a force on the test mass. The phase of

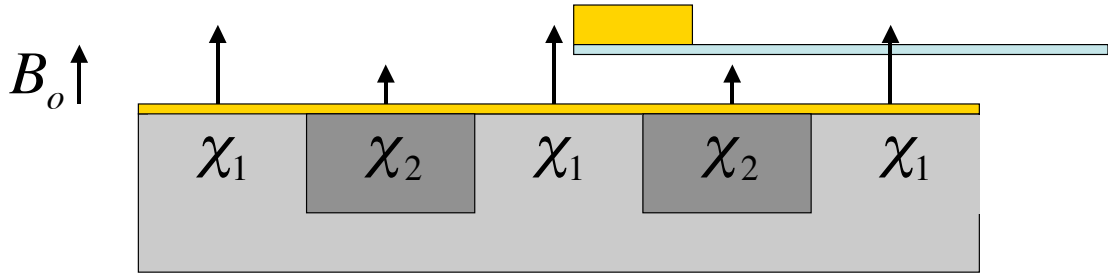


Figure 5.1: A schematic representation of a possible magnetic coupling mechanism that could lead to spurious forces. See text for explanation.

that force relative to gravity depends somewhat on the details of the coupling, but in general one would expect to see it show up at a phase of  $\pm\pi/2$  since it depends on the rate of change of the magnetic field, which should be greatest at the edges of the bars in the drive mass pattern. A back-of-the-envelope calculation for the amplitude of the force follows.

Faraday's law states that

$$\vec{\nabla} \times \vec{E} = \frac{d\vec{B}}{dt} \approx \frac{\vec{B}_o}{1\text{msec}},$$

where  $B_o$  is the approximate amplitude of the applied magnetic field, which should be similar to the field variance between light and dense regions for a superconducting drive mass. 1 millisecond is the approximate time it takes for the test mass to traverse the boundary between light and dense regions. The voltage due to that electric field is

$$V = \oint \vec{E} \cdot d\vec{l} = \oint_S (\vec{\nabla} \times \vec{E}) \cdot d\vec{A} \approx \frac{|B_o|}{1 \text{ msec}} \cdot 4 \times 10^{-8} \text{ m}^2,$$

where the area of the test mass has been taken to be  $4 \times 10^{-8}$  square meters. The current due to this voltage is just  $I = V/R$ , with  $R$ , the resistance of the test mass to circulating currents, equal to approximately  $10^{-4} \Omega$  (data on the low-temperature electrical resistivity of gold are taken from reference [49]). This current gives the test

mass a temporary magnetic moment  $\vec{m} = I \cdot A$ , where  $A$  is again the area of the test mass ( $4 \times 10^{-8} \text{ m}^2$ ). The force that the magnetic field exerts on the test-mass-bearing cantilever as a result of this magnetic moment has two terms:

$$F = \frac{\vec{m} \times \vec{B}_o}{L_{\text{cant}}} + \vec{\nabla}(\vec{m} \cdot \vec{B}_o),$$

where  $B_o$  is the same magnetic field as before. The first term represents a torque which the cantilever converts into an apparent force, and the second term represents a direct force on the test mass. The two terms, though geometry-dependent, are generically of similar size for this system (because the length of the cantilever is comparable to the distance over which the field presumably varies rapidly). The size of the force is thus approximately

$$F \approx \frac{I \cdot 4 \times 10^{-8} \text{ m}^2 \cdot |B_o|}{10^{-4} \text{ m}} \approx \frac{|B_o|^2 \cdot 10^4 \text{ } \Omega^{-1} \cdot (4 \times 10^{-8} \text{ m}^2)^2}{10^{-3} \text{ s} \cdot 10^{-4} \text{ m}}.$$

According to this calculation, forces of 10 femtoNewtons could be produced by a field of about 80 milliGauss. Of course, this calculation is very rough, but it indicates the potential for measurable eddy-current coupling in the system. It is important to note that the above analysis assumes the maximum possible susceptibility difference—if the drive mass is not superconducting, this force will be very substantially reduced.

### Time-reversal symmetry breaking

Interactions that are due to a magnetic field, including those discussed above, generically violate time-reversal symmetry. In the context of this experiment, time-reversal symmetry breaking occurs when the phase and amplitude of the measured force are different for clockwise and counter-clockwise runs. The phase can be confusing to keep track of properly for the two different spins, but the usual cinematic analogy for time-reversal symmetry is a useful guide. The right way to think of it is to imagine painting a small pink dot on one of the trenches or anti-trenches of the drive mass at the point of (measured) maximum downward force. When the movie is run backwards (i.e. the spin is reversed), if the pink dot is no longer at the point of maximum

downward force, then time-reversal symmetry has been broken.

Magnetic forces are not the only ones that break time-reversal symmetry—viscous forces due to the bearing gas can as well. Density-dependent forces like Newtonian gravity or Yukawa forces coupling to mass will not break time-reversal symmetry, since the point of maximum force will always be above the dense part of the drive mass pattern. This fact suggests a “Hall-type” measurement, wherein one measures the force with CW and CCW spin and then adds the results, canceling undesirable time-reversal symmetry breaking terms. The results of just such a measurement are plotted in figure 6.5.

## 5.3 Sources of Noise

### 5.3.1 Thermal noise

The ultimate limitation on the sensitivity of this experiment is expected to be thermal noise. Expressed as a lower limit on the detectable force, the thermal noise limit is

$$F_{\text{detectable}} = \sqrt{\frac{4kk_{\text{B}}Tb}{Q\omega_o}},$$

where  $k$  is the spring constant of the cantilever,  $k_{\text{B}}$  is Boltzmann’s constant,  $T$  is the temperature,  $b$  is the bandwidth,  $Q$  is the cantilever’s quality factor, and  $\omega_o$  is its frequency. What this means in practical terms is that a thermal-noise-limited measurement with this apparatus would be (barely) able to resolve Newtonian gravity with a (very achievable) averaging time of 8 hours. If no anomalous force were detected in such a run, the resulting alpha-lambda bounds from the measurement would be at least two orders of magnitude stronger than current limits at length scales near  $10 \mu\text{m}$ . However, the sensitivity of the experiment is not currently limited by thermal noise, due to the relatively high levels of vibrational noise.

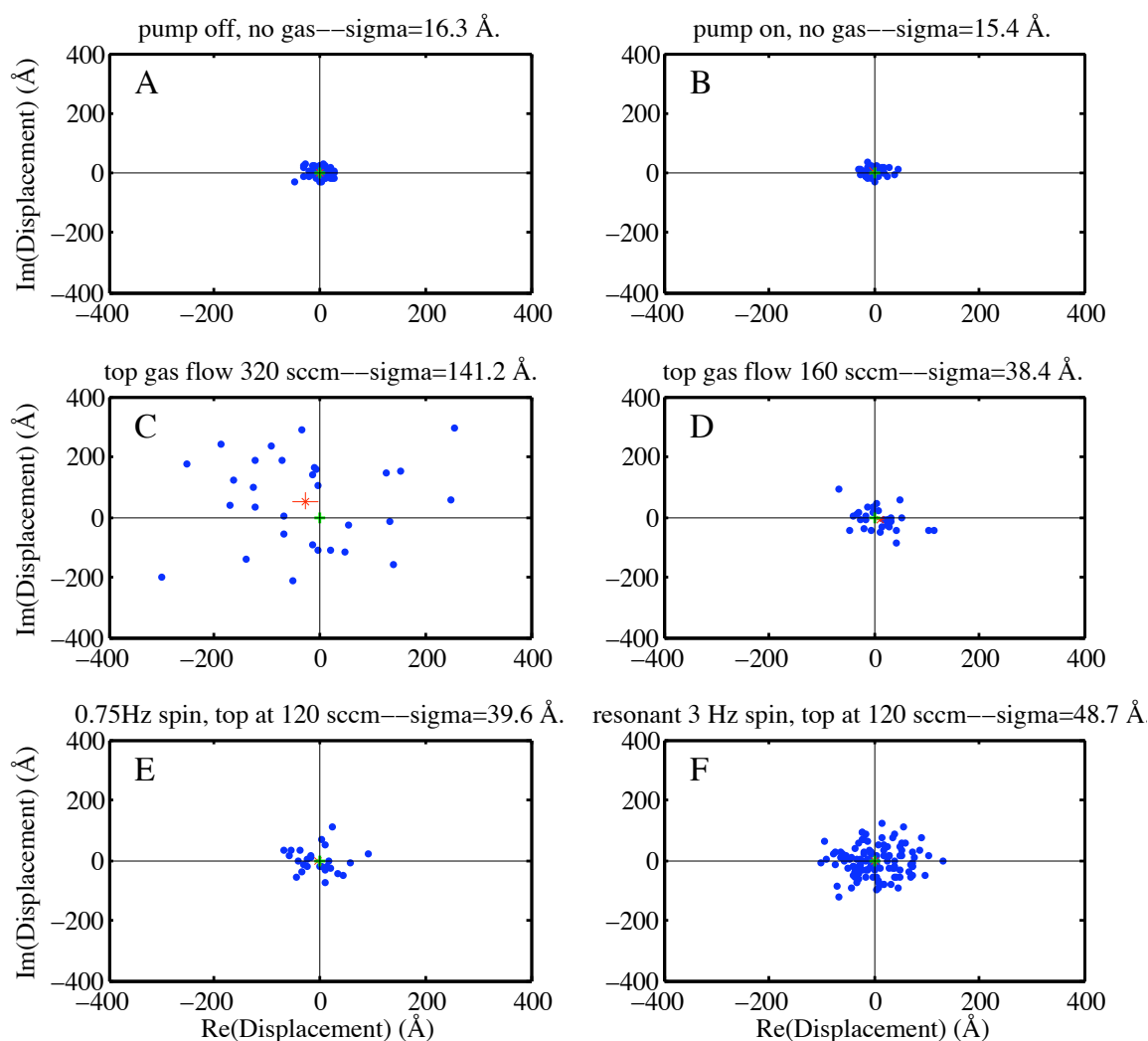


Figure 5.2: Noise data from runs under different conditions, showing the effect of pump vibration and gas flow. Cantilever amplitudes are in Angstroms. **A:** Pump off, no gas flowing —  $\sigma = 16\text{\AA}$ . **B:** Pump on, no gas flowing —  $\sigma = 15\text{\AA}$ . **C:** Top gas flow 320 sccm —  $\sigma = 141\text{\AA}$ . **D:** Top gas flow 160 sccm —  $\sigma = 38\text{\AA}$ . **E:** Spinning at 0.75 Hz, top flow 120 sccm —  $\sigma = 40\text{\AA}$ . **F:** Spinning at 3 Hz, top flow 120 sccm —  $\sigma = 48\text{\AA}$ .

### 5.3.2 Vibrational noise

Vibrational noise (random mechanical or acoustic excitation of the cantilever) is currently the factor that limits the force sensitivity of the experiment. There are several

possible sources of this vibrational noise, which we will itemize here.

- Vibrational noise from the liquid nitrogen boiloff in the jacket. Nitrogen bubbles produce more vibrational noise than helium bubbles, and an approximate correlation has been observed between the level of LN2 in the jacket and the noise level on the cantilever. Use of the jacket is not really optional for this dewar, especially if long averaging times are desirable, so the way to get around this problem is either to purchase a new dewar or to add some in-probe vibration isolation (see appendix E).
- Acoustic noise from the room in which the experiment is housed. The room (Varian 012) which holds the expensive hole which holds the dewar which holds the experiment is extremely loud. The loudness is mainly due to a large radon scrubber mounted in the ceiling of the East end of the room, which has very poor acoustic insulation and produces a constant roar. Additional in-room acoustic noise sources include the HEPA filter fans of the clean hood (also very loud) and the experimenter, who is relatively quiet most of the time. This last source was able to provide direct evidence of the susceptibility of the cantilever to acoustic noise—coughs and handclaps have immediate and obvious effects on the interferometer signal that measures the displacement of the cantilever. Even more striking is the excitation that occurs if a small computer speaker is fed a sinusoidal signal at the cantilever’s resonant frequency; near-apocalyptic excitation levels are easily produced by very low-volume signals. In order to minimize the effects of acoustic noise from the room, both the HEPA filters and the radon scrubber were turned off for many of the best experimental runs. Rudimentary shielding was also provided with acoustic foam around the dewar. In the future, a less noisy environment, an acoustically shielded room, or at least heavy curtains could help improve the force sensitivity of the experiment. Figure 5.2A shows a distribution of measured cantilever displacements when the cantilever is excited only by acoustic noise and nitrogen boiloff; the displacements measured in this plot are well above the level of thermal noise.
- Vibrational noise from the pump. A large mechanical pump must be attached

to the probe in order to quickly remove the exhaust gas from the gas bearing. We use a Welch belt-drive 1397, which is an excellent but very heavy pump that produces large-amplitude vibrations. In order to avoid having these vibrations coupled to the cantilevers, we made a pump-line isolator by submerging a flexible bellows in a bucket of wet concrete, allowing it to cure, and suspending the bucket from a large spring. Resonant frequencies of this system are around 1 Hz. Figure 5.2B shows that this vibration isolation system works well, in that the measured cantilever excitation does not increase when the pump is turned on.

- Vibrational noise from the gas flow in the bearing. The amplitude of this noise source is expected to depend strongly on bearing flow parameters and temperature, and should be minimal for laminar flow. Optimization of the flows and temperature have indeed been shown to strongly reduce the noise— see figures 5.2C, 5.2D, and 5.3 for examples of this. Poorly chosen flow rates can cause substantial excitation of the cantilever, particularly in the top bearing inlet. This circumstance is not unexpected, since any non-laminar flow from the top inlet will directly apply random pressure fluctuations to the shield membrane 10  $\mu\text{m}$  below the cantilever.
- Vibrational noise from the rotor's spin. Mechanical noise due to the spin of the drive mass might be expected to excite the cantilever as well. This effect does not currently appear to be a large problem— figures 5.2D and 5.2E show little additional excitation of the cantilever as the rotor is spun. Additionally, spinning the rotor right at the optimal frequency ( $100 \times$  less than the cantilever's resonant frequency) does not seem to apply any additional force noise to the cantilever, as shown in figure 5.2F.

The data plotted in figure 5.2 show the relative amplitude of the various forms of vibrational noise discussed above, and point to a future need for acoustic isolation, a liquid-nitrogen-free (i.e. superinsulated) dewar, and possibly some in-probe vibration isolation. These upgrades are discussed further in appendix E.

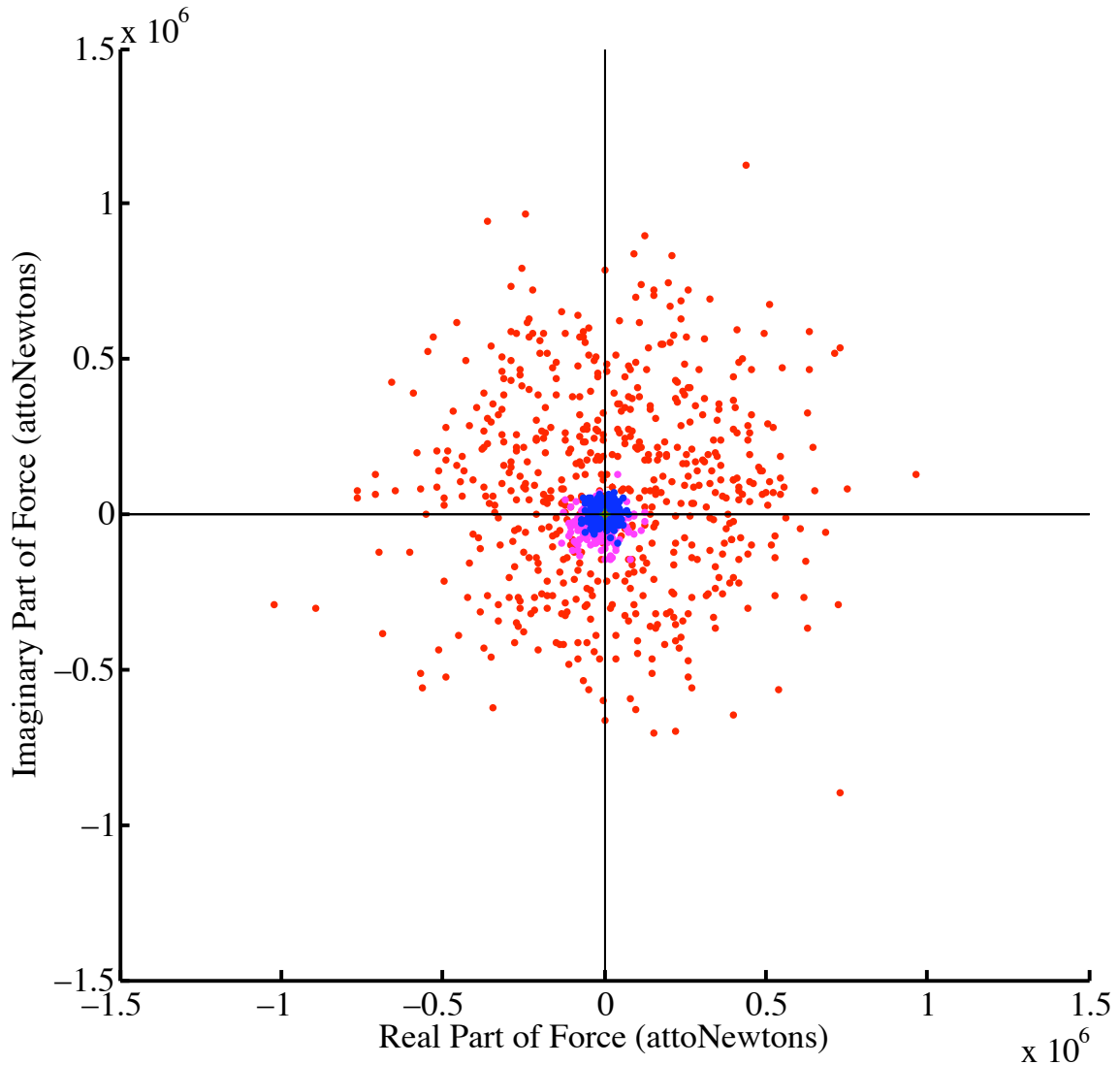


Figure 5.3: Scatter in the mean measured forces is plotted here for three different runs. Red points are from the October 14 run, pink points are from the October 17 run, and blue points are from the November 29 run. The obvious improvement in experimental noise is largely due to optimization of bearing flow parameters and temperature.

### 5.3.3 Other noise sources

The experiment in principle contains many sources of noise apart from thermal and vibrational noise, such as Johnson noise in the  $10\text{ M}\Omega$  feedback resistor of the photodiode amplifier, shot noise in the interferometer, and digitization-induced noise in

the data acquisition card. However, in general these sources are all expected to put less stringent limits on the sensitivity than thermal noise, and are certainly all much smaller than the current levels of vibrational noise. For thorough treatments of these and other noise sources in the Frogland experiment, see references [20] and [8]. Here, we omit to discuss them in detail since they are not important for the current results and are not expected to limit the sensitivity of the apparatus in the future.

# Chapter 6

## Results

This chapter presents the first few batches of data produced by the apparatus. Since the first run of this experiment, optimization of various experimental parameters has yielded dramatic improvements in noise performance. There have been three long cooldowns since the apparatus was constructed (along with a few runs that were aborted due to cryogenic or other problems). As in the Frogland experiment, one cooldown can last as long as several months. The results of those three main runs are discussed in order below. Details of the dates and some parameters of each individual run are in appendix F.

### 6.1 Zeroth Cooldown

No gravity data were taken in the earliest (“zeroth”) cooldown in 2005. The reason was that in that cooldown, the first attempted on the new apparatus, the experiment did not include the capabilities of cantilever  $Q$ -control or computerized feedback on the bearing gas flows. As illustrated in figure 3.22, the surprisingly high  $Q$  of the cantilever observed in that first test cooldown did not allow us to operate the bearing on resonance for any significant period of time. This observation made clear the need for feedback control of both the cantilever quality factor and the drive mass rotational frequency. Apart from the lack of gravity-related data, this cooldown was a success in that most major parts of the experiment functioned as intended.

The drive-mass-bearing rotor, the cantilever wafer, the cryopumped cantilever cavity, continuous (rather than chopped) flow control of the cold gas bearing, and the entire “standoff” fiber interferometer were all new systems on their maiden voyages, and they all worked surprisingly well at low temperatures.

## 6.2 First Cooldown

After the “zeroth” cooldown, we spent some time making the improvements that would allow us to take real data. When the cantilever feedback cooling and the computerized flow control were successfully implemented, we started another cooldown in October of 2006. This run of the experiment was the first in which we were able to excite the cantilever at resonance for long periods of time; in other words, it was the first run that produced useful gravity data. All data from this first run were taken in the month of October. Figure 6.1 presents some instructive results from this cooldown and the next cooldown on one plot. One important thing to note is that the phase of the first two listed October runs is only known modulo  $\pi$  because the experimenter omitted to record the sign of the interferometer fringe. Figure 6.1 is a good representation of our early exploration of experimental phase space which was the main content of the October cooldown. That figure makes it clear that the first four runs (all in October) have larger statistical error bars and larger mean amplitudes than all later runs. This disparity is very likely to be due to two experimental problems that were corrected after the October runs: incorrect flow parameters, and a non-negligible magnetic field. Both are discussed below.

We were running the experiment for the first time in October, and were initially unaware of the optimal operational parameters (especially gas flow rates). The helium flow to the top inlet of the gas bearing was initially set to 320 sccm, a value which it turns out is much too high for good operation, and which probably produces turbulent flow across the top surface of the drive mass. Statistical errors went down steeply as we lowered the gas flow in the top and bottom inlets of the bearing, as can be seen from the later runs plotted there.

Another factor contributing to the smoother more stable flow in later runs was the



thermal coupling between the bearing exhaust and the helium bath— attempts to heat the bearing during this cooldown boiled a lot of helium without achieving any significant temperature rise.

Helium flow rates and temperatures were not the only experimental parameters that required tweaking. The probable cause of the large mean forces measured in the October run (as distinct from the large statistical errors) was the fact that the  $\mu$ -metal shield around the dewar was not degaussed before the run. This omission would produce a non-negligible magnetic field in the interior of the dewar, especially since the shield had not been degaussed in more than a decade, during which time it had been moved (and probably banged around) at least once. As discussed in section 5.2.2, this field would be particularly likely to cause spurious measured forces when the experiment was operated at base temperature with a brass drive mass, as it was during all the October runs. The reason for this is that the brass masses contain superconducting inclusions that would certainly be below  $T_c$  at 4.2 °K, drastically boosting the susceptibility of the dense parts of the drive mass pattern. The amplitude of eddy-current type forces should scale quadratically with the field, but the exact value of the magnetic field inside the dewar before degaussing the mu-metal is unknown. However, the back-of-the-envelope calculation (in section 5.2.2) of the amplitude of the expected magnetic force confirms the plausibility of the hypothesis that the large spurious forces in the October runs were due to magnetic interactions. Stronger support for this hypothesis, of course, comes from the fact that the spurious forces were greatly decreased for all runs in the next cooldown, after the mu-metal had been degaussed.

### 6.3 Second cooldown

In between the first and second data-producing cooldowns, we made several improvements. First, we degaussed the mu-metal shield. We also worked to solve the problem with high pressure in the OVC that was preventing heating of the bearing. No leak was found at room temperature, so we set up a turbopump running through a second vibrationally isolated pumping line to bail out the OVC at low temperatures.

Finally, the mass flow controllers for the clockwise and counter-clockwise gas lines were replaced with new controllers that had lower minimum flow rates. These new controllers allowed us to operate the bearing in a more salubrious gas flow regime. These improvements to the apparatus resulted in significantly improved data from the November/December cooldown, as detailed below.

### **Runs of November 19 and 22**

The runs of November 19 and 22, shown in figure 6.2, were taken after degaussing but without heating the bearing. The spurious force observed in the October runs was reduced by nearly an order of magnitude, providing strong indirect evidence that the spurious force was magnetic in origin. The CW (November 19) and CCW (November 22) runs exhibit the generally observed pattern of time-reversal symmetry breaking, in which the imaginary part of the force is positive for CCW runs and negative for CW runs. However, the mean of these two runs is still skewed away from the y-axis, indicating that an attractive force is observed for both senses of rotation. A force that was purely antisymmetric under time reversal would average to zero over the two spin directions. In order to try to destroy superconductivity in the brass drive mass, we next tried heating the gas flowing into the bearing.

### **Runs of November 17 and November 23**

Making use of the new ability to heat the bearing gas flow, we took a CW run and a CCW run at temperatures above the  $T_c$  of lead (at 8.4 °K and 9.6 °K respectively). The resulting measured forces (shown as the Nov 17 and Nov 23 data points in figure 6.2) are more nearly symmetric around zero than the cold runs. Therefore, this initial heating of the bearing, while it did not eliminate the measured imaginary component of the force, did result in a more nearly time-reversal-antisymmetric force.

The temperature that was recorded for each run (and that served as the control variable for the temperature feedback loop) was measured by the CGR thermometer suspended just outside the exhaust port through which the majority of the spinup

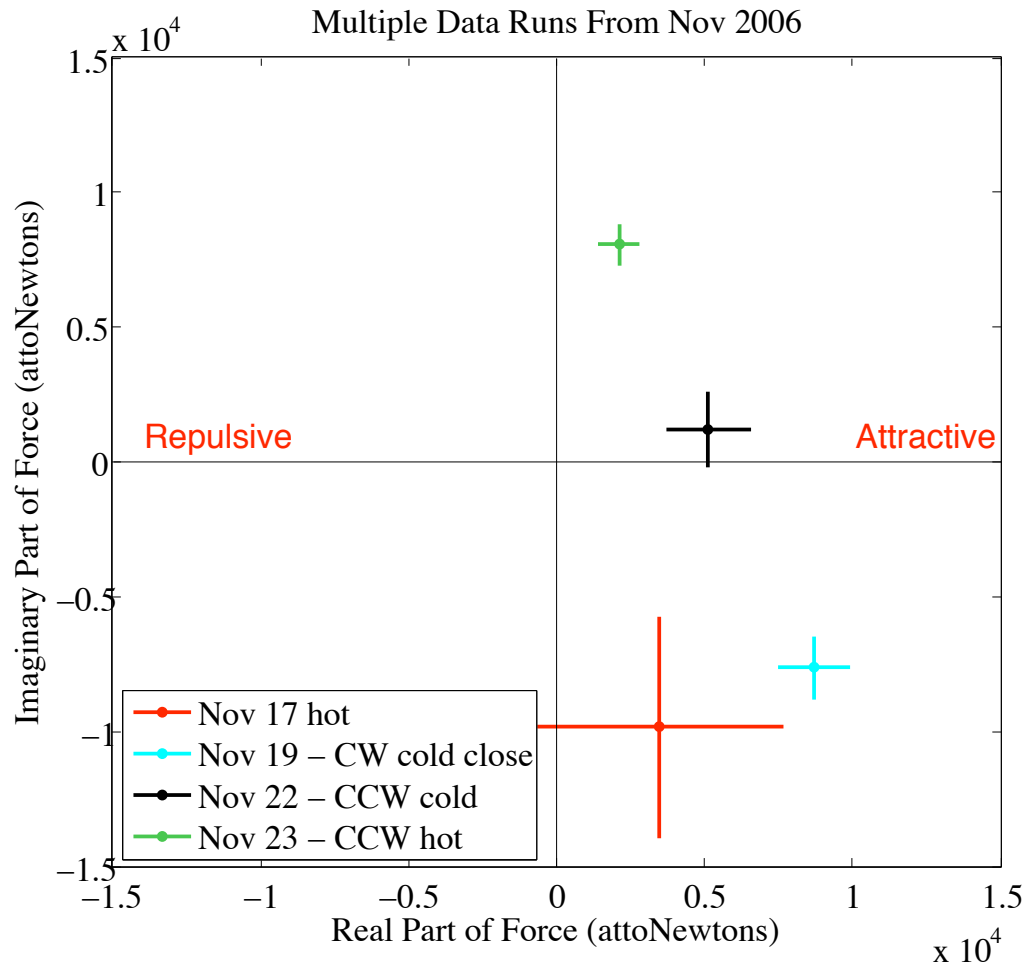


Figure 6.2: Data from multiple runs taken during the November cooldown. Note that the two heated runs are fairly consistent with a purely time-reversal-antisymmetric force, while the two cold runs have a mean well distinguished from zero. Error bars represent one-sigma statistical errors.

flows passes. The installed thermometer is visible in the photo on the right of figure 3.10. What this means is that the temperature being measured is essentially the temperature of the spin flows themselves, not necessarily the temperature of the top inlet or of the metallic drive mass itself. The possibility that the lead in the drive mass was not actually driven above its critical temperature is thus difficult to discount, given the possible existence of large temperature gradients in the bearing. A

fairly easy cure for this problem would be to put the thermometer in the exhaust of the top gas inlet; it would thus measure the temperature of the gas with the most direct thermal connection to the drive mass. This upgrade would probably also require a new monolithic drive mass spacer washer to channel the exhaust flow, as detailed in appendix E. In any case, despite this possible ambiguity regarding the real drive mass temperature, the gas heating does show signs of improving the flow characteristics. The run of November 23, the second heated run, had lower statistical error bars than any of the previous runs taken at base temperature.

Our first attempt to heat the bearing during the November runs (which occurred on the 17th) caused extremely rapid liquid helium boiloff which resulted in increased vibrational excitation of the cantilever. The maximum averaging time of that run was also limited by the need to replenish the boiled-off helium. Those two effects are responsible for the larger statistical error bars on the Nov 17 point in figure 6.2. After that run, we learned how to perform the heating more efficiently, and achieved the correspondingly lower statistical error bars visible on the Nov 23 run. In general, the heating procedure added some extra “knobs” to the apparatus, which required some optimization. To this end, we took several heated runs under different conditions. After some experimentation we arrived at a set of parameters that produced the smoothest run taken to date; that run is discussed in the next section.

### **Run of November 29**

The data from a single long run (that of November 29<sup>th</sup>) are plotted in figure 6.3. The bearing was heated to 8.4 °K during this clockwise run. The points are color-coded to indicate the time at which they were taken, and the data were analyzed to determine if there was a drift in the mean force over the course of the run. Figure 6.4 shows the mean force with statistical error bars for the same run as figure 6.3. The measured force is consistent with zero at 2-sigma level.

The data plotted in figures 6.3 and 6.4 are promising, in that measurable spurious forces have been eliminated. It seems that the experimental parameters used for that run are close to optimal, given the current level of vibrational noise. However, it is difficult to draw firm conclusions regarding this optimization from many runs spaced

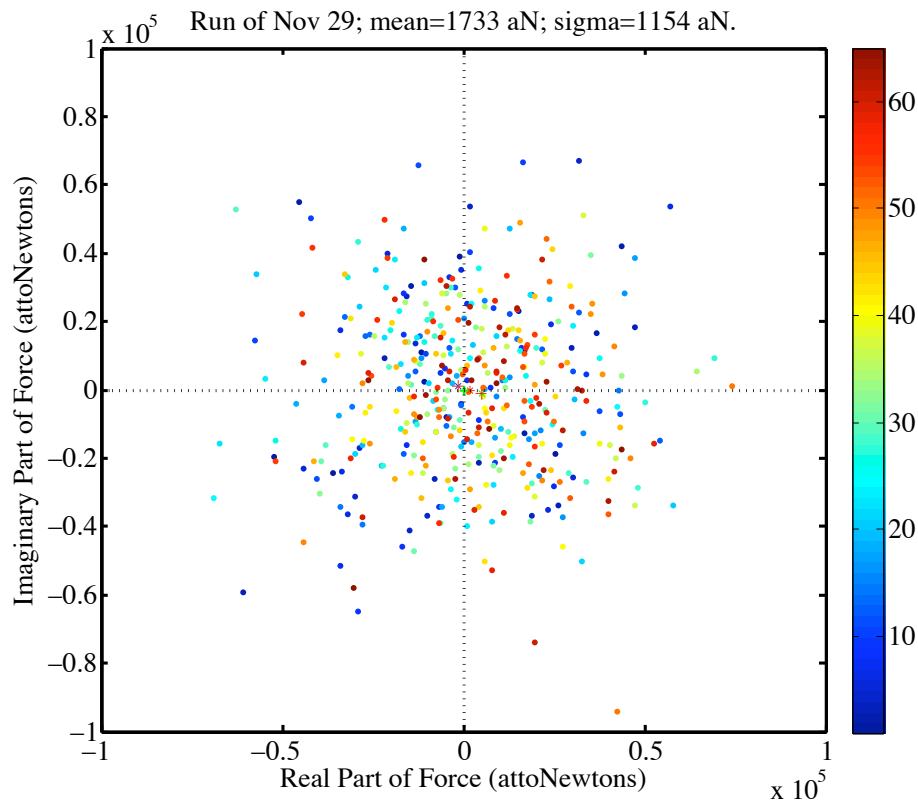


Figure 6.3: Mean measured force signals from a single run from November 29th. Each point represents 15 seconds of data. The colors of the points correspond to the order in which they were taken— higher on the color bar is earlier in the run. The mean measured force for this run is consistent with zero at the  $2\text{-}\sigma$  level.

out over a long period of time. To reduce the effects of possible drifts and run-to-run variation in temperature, magnetization, and flow, we took one set of data that varied two important parameters in one day of continuous data-taking. Those data are described in the next section.

### Runs of December 7th

In order to help elucidate the effects of different bearing flow parameters and further test the time-reversal symmetry of the spurious force, four sets of data were taken in one day (December 7<sup>th</sup> 2006). These data were taken with the drive mass rotating

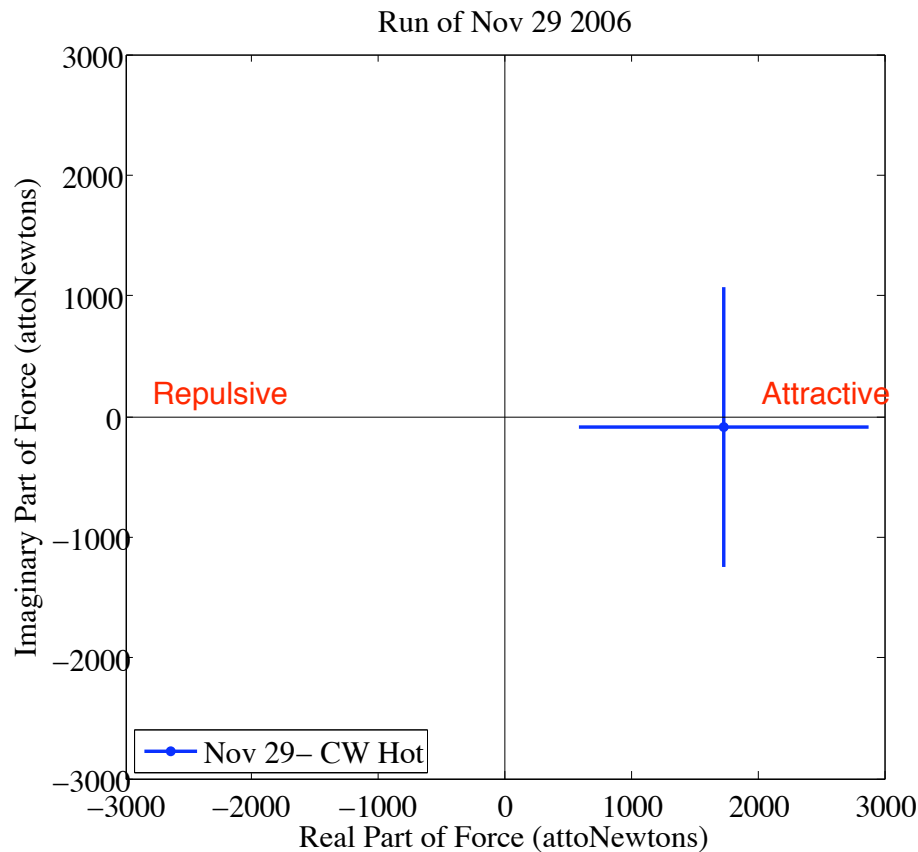


Figure 6.4: Mean and standard deviation of the data from the run of November 29th. Error bars are one-sigma statistical. The mean measured force for this run is consistent with zero at the  $2\text{-}\sigma$  level.

both clockwise and counter-clockwise for each of two different values of flow in the bottom gas inlet (56 and 80 sccm He). The flow in the top gas inlet was held at 40 sccm He for all four sets, and the bearing exhaust temperature was held at 9 °K. The two different flow settings resulted in two different equilibrium  $z$ -positions for the rotor: 18  $\mu\text{m}$  and 13  $\mu\text{m}$  below the top, respectively (see figure 3.7 for another example and an explanation of this effect). The results of these runs are shown in figure 6.5. As before, only the mean force for each run is plotted, along with one-sigma statistical error bars. Also shown are the average of the CW and CCW runs for each value of the bottom gas flow. This sort of averaging should cancel out effects

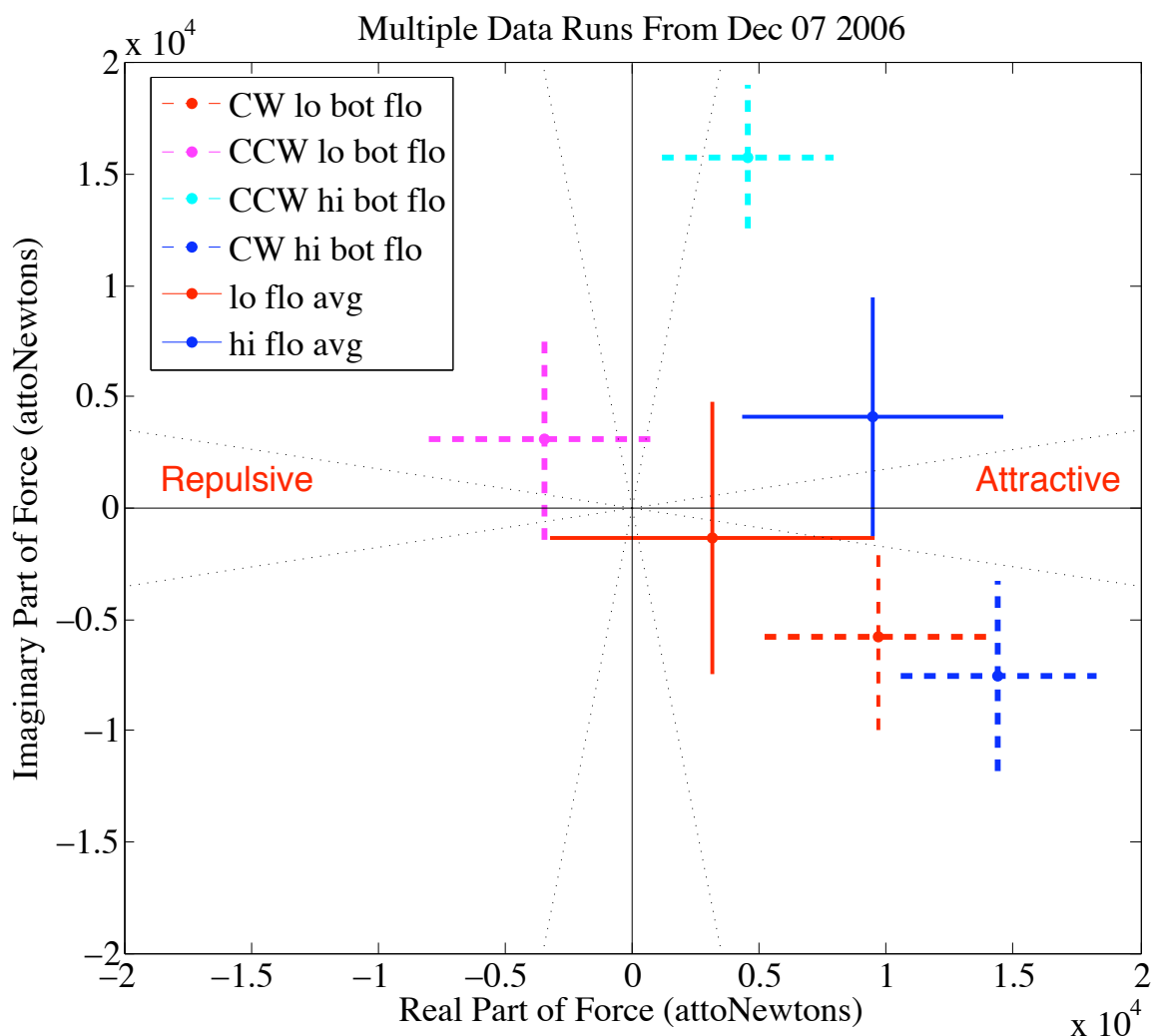


Figure 6.5: Mean measured force signals from four runs: CW and CCW rotation for each of two different flows in the bottom gas inlet. The “hi flo” measurements were taken with 80 sccm flow in the bottom inlet, and the rotor 13  $\mu\text{m}$  from the lid. The “lo flo” measurements were taken with 56 sccm flow in the bottom inlet, and the rotor 18  $\mu\text{m}$  from the lid. Averages of the two different rotation senses for each flow value are also plotted. Error bars represent one-sigma statistical errors.

which violate time-reversal symmetry (see section 5.2.2 for more details).

The data, as in earlier runs, show a clear effect from reversing the sense of rotation.

The imaginary part of the measured force (corresponding to a phase  $90^\circ$  from that of Newtonian gravity) switches sign between the CW and CCW runs. In fact, for the “lo flo” (lower  $z$ -position, farther mass-to-mass distance) runs, the CW and CCW measurements are symmetric around the origin, within the one-sigma statistical error. The mean force of the two “hi-flo” runs seems to be slightly displaced in the direction of attractive force, although it is in fact also consistent with zero, this time at the *two-sigma* level. The statistical errors for these runs are large because they did not last very long; each of the four runs represents only about 45 minutes of data. The short length was due to the time constraints imposed by the need to take four heated runs on one “tank” of helium. These data give a blueprint for further exploration of experimental phase space, and further suggest the presence of a time-reversal-symmetry breaking effect, possibly due to magnetism or disturbances in the flow.

### 6.3.1 General properties of data

Although the experimental parameters were varied fairly widely in the name of optimization, the data observed so far show a few generally invariant properties. The most obvious of these is the preponderance of positive real parts— every data run that had a well-defined phase had a real part greater than zero. Thus, the measured force, when phase-correlated with the mass pattern, was always attractive. This effect was not always statistically significant, however.

The other property that nearly all the experimental runs have shared is some level of time-reversal symmetry breaking. The imaginary component of the measured force tended to be positive for counter-clockwise runs and negative for clockwise runs. This difference *was* generally statistically significant.

## 6.4 Limits on non-Newtonian interactions

The best runs performed so far using this apparatus (i.e. the ones with the lowest averaged vibrational noise) were the runs of November 23 and November 29. To extract a limit from the November 23 run, we make use of the phase-sensitive nature

of the experiment by projecting the mean measured force onto the real axis. This operation does not significantly affect the limit from the November 29 run, since the mean measured force was almost entirely real. In any case, the limits obtained from the two runs are very similar. The resulting bounds on non-Newtonian interactions are plotted in  $\alpha - \lambda$  space in figure 6.6. Limits on both attractive (blue line) and repulsive (pink line) forces have been plotted. The presence of two bounds is a departure from tradition; typically the  $\alpha$  on  $\alpha - \lambda$  plots represents the absolute value of  $\alpha$ . The point of plotting the pink line is to show that, since the mean measured force is attractive, the range of negative alphas ruled out at the 2-sigma level is greater than that of positive alphas. The limits on attractive forces that can be extracted from the first runs of this experiment are equal to the best existing limits at five-micron length scales. The limits on repulsive forces, as mentioned above, are better. As shown in figure 6.6, the ultimate thermal-noise-limited sensitivity of this experiment would be substantially better than any limit achieved so far.

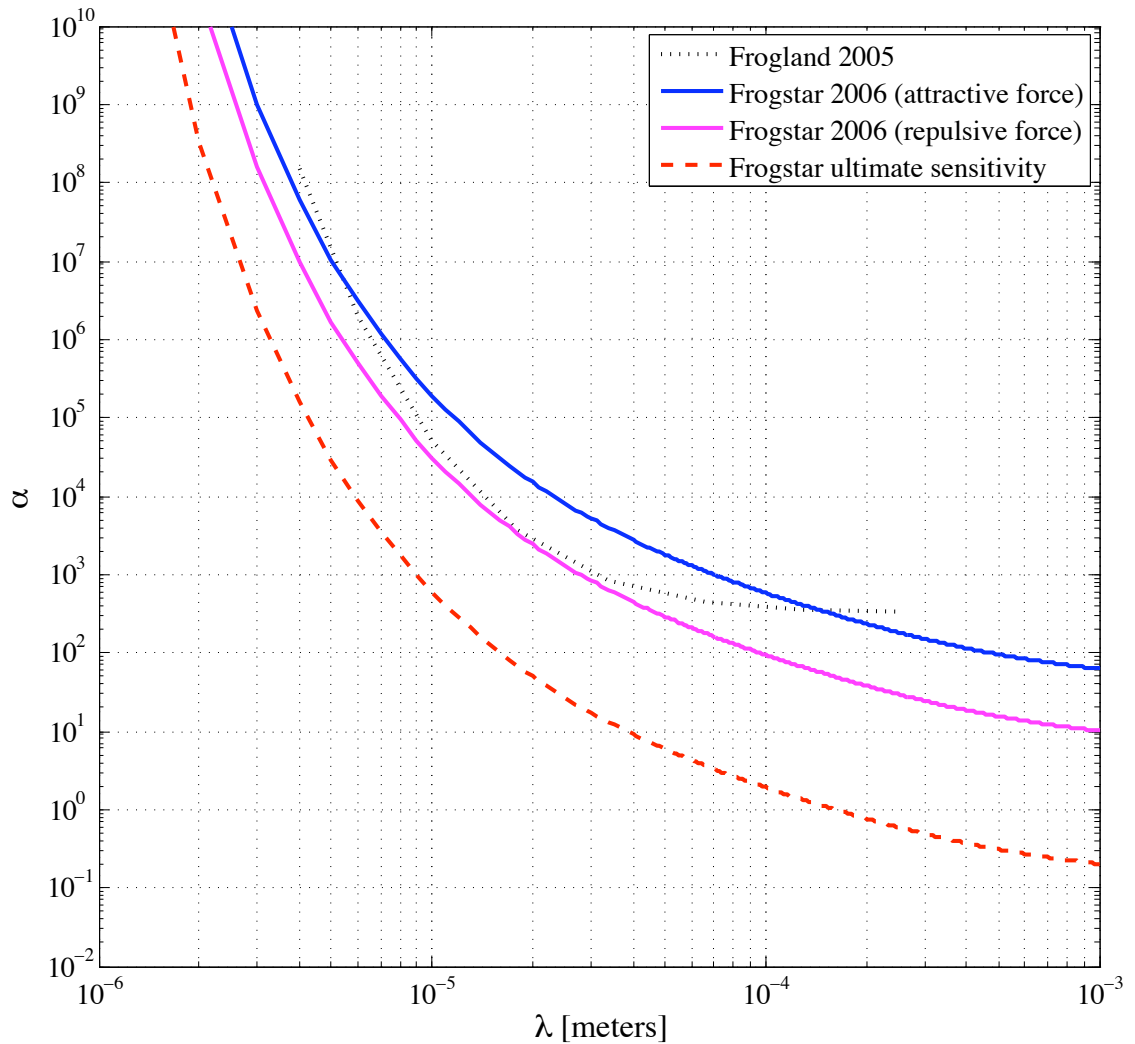


Figure 6.6: The bounds on non-Newtonian interactions extracted from the first data taken with this experiment. Bounds on attractive interactions are represented by the solid blue line, bounds on repulsive interactions by the solid pink line. Each line represents the mean measured force with experimental uncertainties and a two-sigma statistical error. The data from reference [19] (dotted line) are plotted for reference. The bounds that would be achieved by thermal-noise-limited operation of this apparatus are shown as a dashed line.

# Chapter 7

## Conclusions

We have designed, constructed, tested, and successfully run a new apparatus for detecting or constraining deviations from Newtonian gravity at small length scales.

There are many technical challenges associated with measuring gravitational interactions at short distances. To overcome these challenges we have developed several techniques that could prove to be useful in other areas. In particular, we feel that the idea of using radiation pressure to cool a micromachined cantilever, the combination of encapsulated MEMS sensors with an integrated cryopump, the use of a macroscopic gas bearing as a general-purpose low-temperature motor, the methods of simple and precise fabrication of “intermediate-scale” metallic structures, and some of the arcane techniques of dimensionally stable planarization could find wider application.

The first experimental runs of the apparatus produced the limits on non-Newtonian interactions shown in figure 6.6. The force sensitivity is currently limited by vibrational noise. Figure 6.6 also shows the excellent ultimate thermal-noise-limited sensitivity of this apparatus. Because the probe has not yet been operated at the limit of its sensitivity, any further work along the lines discussed in appendix E should produce even better results.

# Appendix A

## Other Experimental Approaches

In this appendix we list some of the experimental approaches to the problem of drive mass actuation that we considered when thinking about the initial design of the experiment. A major goal was to improve upon the limited range of motion of the piezoelectric bimorph in the Frogland experiment. This goal was important because a larger range of motion would allow the use of larger area drive masses and test masses, which would greatly increase the expected force from any mass-dependent interaction.

- **Capacitance-driven reed.** A modification of the design of the Frogland experiment. The idea was to use a geometry similar to that of the Frogland experiment, but to give the drive mass a larger range of travel at low temperatures by using a capacitively-driven reed instead of a piezo as the actuator. This scheme would have been the easiest to implement, since it is essentially an upgrade to Frogland, but it offered more limited improvements than some of the others.
- **Ballistic mercury.** This somewhat farfetched idea involved shooting drops of mercury out of a nozzle electrostatically in a vacuum, and aiming them so that they passed near a mass-loaded cantilever, exerting a force on it. It seems likely to be plagued by spurious electrostatic forces.
- **Microfluidic mercury.** Mercury is again used as the drive mass in this scheme,

but this time the drops of liquid metal are alternated with drops of a less-dense liquid and pumped through a microfluidic channel underneath the cantilever. This idea is cheap and relatively easy, but requires the drive mass to be at room temperature. I think it is the most promising of the ideas that we did not use— one can easily imagine incorporating good vibration isolation and a good vacuum for the cantilevers in such a scheme. The disadvantage of the room-temperature drive mass could be overcome by long averaging times (enabled by the simpler non-cryogenic apparatus) or possibly by mounting the cantilever on a cold finger in a vacuum (this would add substantial complexity, though).

- **Motor-driven disc.** A low-temperature electric motor is used to rotate a disc containing a pattern of alternating densities. The cantilever can be mounted either facing the rim of the disc (“rimfire” style) or the flat of the disc (“record player” style). We investigated this possibility fairly extensively before we came upon the:
- **Gas-bearing-driven disc.** In this setup, the disc-shaped drive mass is actuated and supported by flows of helium gas. It eliminates electrical interference from the motor, solves the problem of making good low-temperature bearings, and has the very important advantage of being self-aligning. This scheme is the one we used, of course. There was initially some thought of using Frogland cantilevers and test masses in this scheme, but we ended up deciding to make new ones in order to take full advantage of the enhanced force signal from larger area masses.

# Appendix B

## Thermal Analysis of the Cantilevers

This appendix presents a simple analysis of possible thermal issues involving the cantilevers used for force detection in this experiment.

### **Room-temperature thermal characteristics of the cantilevers**

While the experiment is running, both a 1310nm laser (used for interferometric position readout) a 1550nm laser (used for the radiation pressure  $Q$ -damping discussed in section 3.6.5) shine light on the cantilever. The power of the “damping laser” can be electronically modulated from the “off” state to a few mW at speeds up to several KHz. This modulation puts a time-varying force on the cantilever, due to the momentum of the laser photons. While testing this setup, we noticed some odd effects at intermediate pressures– the force exerted by the laser seemed to be enhanced at ambient gas pressures of a few Torr, compared with the force at atmospheric pressure or high vacuum. A possible explanation for this phenomenon is some kind of “radiometer” effect or Knudsen force, where thermal gradients affect the local gas pressure and thus cause the gas to exert a net force on the cantilever. It was also observed that the resonant frequency of the cantilever was shifted slightly by the application of an unmodulated (DC) light beam from the damping laser. There are

a few possible reasons for this effect, but the most likely is that the slight temperature rise of the cantilever under laser illumination is asymmetrically stressing the two cantilever legs, resulting in a slight modification of the effective spring constant. Neither of these effects are directly worrisome, but to make sure that thermal effects cannot interfere with the measurement of mass-dependent forces, a quick analysis of the transient thermal behavior of the cantilever under laser illumination seemed like a good idea.

First, a definition of the variables we will use:

Symbol	Value	Units	Definition
$T_{\Delta}$	Variable	$^{\circ}\text{K}$	Temperature rise of center of test mass
$t$	Variable	s	Time since laser switched on
$\mathbf{P}$	$2.5 \times 10^{-5}$	W	Power absorbed from the laser
$m$	$3 \times 10^{-8}$	Kg	Mass of the test mass
$\kappa$	30	W/m $^{\circ}\text{K}$	Thermal conductivity of $\text{Si}_3\text{N}_4$ cantilever
$c$	132	J/Kg $^{\circ}\text{K}$	Specific heat of gold test mass
$A$	$6 \times 10^{-11}$	$\text{m}^2$	Cross-sectional area of cantilever legs
$l$	$1.3 \times 10^{-4}$	m	Length of cantilever legs

Table B.1: Definitions of units used in calculations of cantilever thermal properties.

We assume that the infrared reflectivity of the test mass is 97.5%, meaning that it absorbs 2.5% of the  $\sim 1\text{mW}$  output of the laser. We also assume that the test mass is always at a single temperature, and that all thermal gradients occur in the cantilever legs. This assumption is clearly quite a good one, due to the high thermal conductivity of gold and the constrained geometry of the cantilever legs; it is also validated by our numerical analysis. The calculations are performed for a  $400 \mu\text{m}$  cantilever with a test mass that is  $40 \mu\text{m}$  thick—this is a little thicker than our usual masses, but the settling time should scale linearly with thickness, and the final temperature gradient should be largely unaffected by it.

Under those assumptions, the heat flowing into the test mass minus the heat flowing out of the test mass must equal the heat capacity times the rate of change of its temperature:

$$\dot{Q}_{\text{in}} - \dot{Q}_{\text{out}} = cm \frac{dT_{\Delta}}{dt}. \quad (\text{B.1})$$

Since the rate heat flowing in is just the laser power absorbed, and the heat flowing out is conducted along the length of the cantilever legs to a reservoir held at  $300^\circ\text{K}$ , this can be rewritten as:

$$\mathbf{P} - \kappa \frac{A}{l} T_\Delta = cm \frac{dT_\Delta}{dt}. \quad (\text{B.2})$$

This linear differential equation for  $T_\Delta$  can be easily integrated to give the time-dependent solution:

$$T_\Delta(t) = \frac{\mathbf{P}l}{\kappa A} \left(1 - e^{-\frac{\kappa A}{cm}t}\right). \quad (\text{B.3})$$

This expression is plotted in Figure B.1, along with the results of a finite-element ANSYS simulation. The agreement between the two is excellent: the thermal settling time of the test mass is about a second, and its temperature goes up by a little less than 2 degrees under full-power (1 mW) illumination from the 1550nm laser.<sup>1</sup> This close agreement between numerical and analytic results is cause for confidence in the results of any more complicated thermal modeling of the cantilever system that might be required.

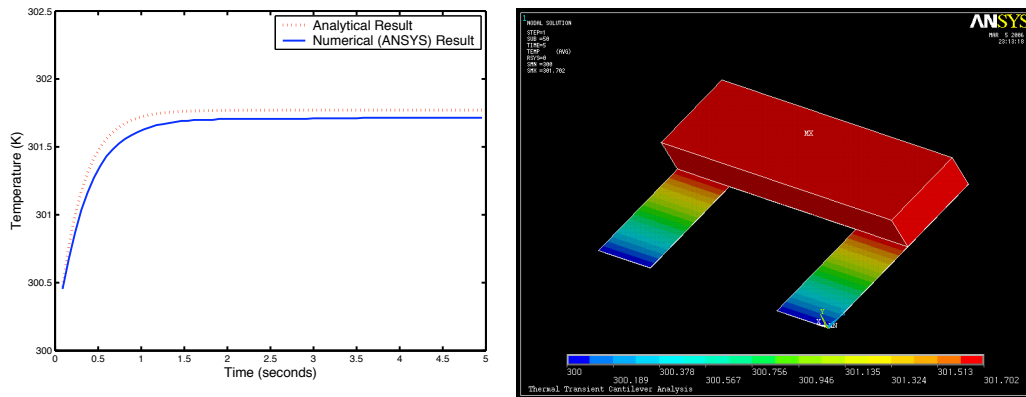


Figure B.1: Left: Transient thermal response of the test mass to laser illumination. The dotted red line is the analytic result derived in the text, and the solid blue line is the result of an ANSYS finite-element calculation. Right: the final temperature profile of the cantilever, from the ANSYS simulation.

<sup>1</sup>The power necessary for effective radiation pressure damping of thermal noise is actually much smaller than 1 mW if the cantilever-fiber alignment is good; typically only a few  $\mu\text{W}$  of 1550nm light are required.

These results do not fully explain the observed “radiometer” effect, since they indicate that the opposite sides of the test mass are at nearly the same temperature at all times. Also, the symmetry of the calculation prevents treatment of the slight photothermal modification of the spring constant that is generally observed. Both these problems can be dealt with by considering in more detail the manner in which the test mass is attached to the cantilever. This attachment (detailed in section 3.5.2) is done by applying a small bead of Torr-Seal epoxy to the end of the cantilever with a micrometer-actuated probe tip, and gently resting the test mass on top of it. The resulting glue layer is of course not perfectly symmetric, and in a vacuum it is this epoxy layer that is responsible for conducting heat from the test mass into the cantilever. It is thus easy to imagine how a temperature imbalance between the top of the test mass and the bottom of the cantilever might arise, and also how the temperature distribution along the cantilever legs might itself not be perfectly symmetric. As a qualitative illustration of this, figure B.2 shows the results of an ANSYS calculation of the temperature distribution along the bottom of a cantilever whose test mass is attached by a small round dot of epoxy instead of a perfect rectangular layer.

Apart from the qualitative plausibility arguments for explanations of observed effects given above, this quick analysis has two important results:

1. The thermal time constant of the system of cantilever and test mass in vacuum is several seconds— much too long for thermal forces to play an important role at typical cantilever frequencies of  $\sim 350$  Hz.
2. The total temperature rise of the cantilever under full-power illumination from the 1550nm laser is only 2 °K— since typically a hundred times less power than this is needed for damping, the temperature rise of the cantilever due to laser light absorption is not a significant source of error or thermal noise for the experiment.

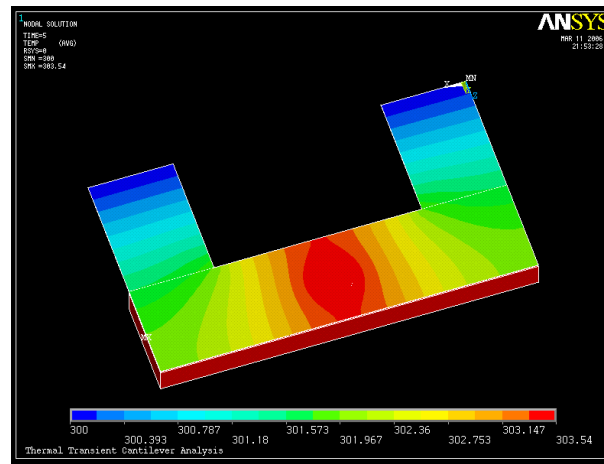


Figure B.2: Results of an ANSYS calculation of the final temperature profile along the bottom of a cantilever with the test mass attached by a small round dot of epoxy. In this case, the average temperature of the top of the test mass and the bottom of the cantilever are clearly different, and it is easy to see how asymmetric gradients in the cantilever legs might arise.

### Low-temperature thermal characteristics of the cantilevers

The results above were obtained assuming values of heat capacity and thermal conductivity that are valid at room temperature, since this analysis was initially done in support of the room-temperature radiation pressure damping experiment [39]. Since the actual gravity experiment is performed at liquid helium temperature, the low-temperature thermal behavior of the cantilevers is also relevant. Both the heat capacity of gold and the thermal conductivity of silicon nitride decrease substantially when the materials are cooled to 4.2 °K. The heat capacity of gold is reduced by a factor of  $\sim 750$  [50, 51], and the thermal conductivity of the nitride goes down by about a factor of 50 [52] (the exact number is somewhat dependent on details of the fabrication processing). This means that the thermal time constant does decrease, but only by a factor of  $\sim 15$ . Thus, the time scale of thermal forces remains well separated from the period of the cantilever's resonance: even at low temperatures we can be confident that photothermal forces do not have significant AC effects at 350 Hz.

However, the temperature rise of the cantilever under illumination is inversely proportional to the thermal conductivity of the silicon nitride. Assuming constant power, this means that the cantilever's temperature rise will be a factor of  $\sim 50$  higher at 4 °K than at 300 °K. We did not initially expect this to be a problem, for two reasons. The first is that very low power is needed to damp the thermal oscillations of the cantilever at room temperature, so the initial temperature rise is more than 50 times less than the maximum convenient value. The second reason is that since thermal oscillations have lower amplitude at low temperature, about eight times less power is actually needed for the feedback cooling at 4 °K than at 300 °K (see equation 3.4). In the current incarnation of the experiment, though, the cantilever is excited above thermal noise by external vibrational and acoustic noise. This means that the 1500nm laser must be run at higher power to achieve a given damping, and also that the power will not scale down with temperature. In the data runs reported in this dissertation, we typically ran the damping laser at an average power of 250  $\mu$ W, which according to the above analysis would correspond to a temperature rise of about 20 °K. This is higher than we would like, but because of the dominance of vibrational noise over thermal noise it did not currently have an effect on our force sensitivity. In the future, as the vibrational noise in the system is reduced, the necessary optical power of the feedback cooling system will be correspondingly reduced, making it unlikely that heating of the cantilever by the damping laser will ever be a limiting factor for this experiment.

# Appendix C

## Care and Feeding of the Probe

This appendix lists, in no particular order, a few important technical details and tips regarding the storage, assembly, and disassembly of the probe. It will probably only be of interest to possible future operators of the experiment.

- Assembly of all the different parts of the probe is complicated and time-consuming. An idea of what is entailed can be gotten from three pictures in this dissertation. The fully disassembled gas bearing appears in figure 3.4. A partially assembled probe (without lid or cantilever wafer) can be seen in figure 3.10. And the fully-assembled probe, ready to be cooled down, is depicted in figure 3.2.
- For disassembly or maintenance, the probe is raised out of the dewar with the 600-lb CM Shopstar hoist, and translated along the track in the ceiling into the miniature cleanroom (aka clean hood). This translation procedure is tricky; great care must be taken to avoid breaking off the fiber where it exits the feedthrough at the top of the probe. The clean hood is indeed necessary, and must be operated continuously when the probe is in it in order to keep the bearing free of dust. However, when the experiment is running, the hood should be sealed up and turned off, since its fans produce quite a lot of vibration at frequencies very near the cantilever resonance.
- Annular kapton shims are placed in series with the drive-mass-spacer washers

under the bearing lid to add clearance for the rotor in the bearing cavity. One-mil and half-mil kapton shims have been made; in general, one should use the thinnest shims that still allow the bearing to rotate freely. The drive-mass-spacer washers, made from the same material as the drive mass, should all be the same known thickness; if they are thinner than the drive mass itself then extra kapton shims can be added.

- The crude homemade spring washers between the lid and the teflon nuts are designed to ensure constant and even downward pressure on the lid; I never was really sure whether or not they helped, but I'm fairly sure they don't hurt anything. The teflon washers contract a lot when cooled, so they will grip the threaded quartz rods tightly at low temperature.
- Due to a fabrication error, the etched patterns on the cantilever wafers are slightly off-center (the cantilever trenches and the holes still have the proper orientation and concentricity, but the edge of the wafer is not concentric with the pattern). The only problem this causes is that the cantilever wafers, as fabricated, do not fit into the probe because of contact with one of the bearing support rods. The best way to understand the problem is to just try and insert a wafer and see where it hits. The problematic edge of the wafer is 90° clockwise of the hole that serves as the encoder feedthrough. The solution is to sand down that edge of the cantilever wafer until it fits. Fairly coarse sandpaper should be used so that this doesn't take too long, but of course great care must be exercised to avoid cracking the wafer. I like to hold the wafer above the sandpaper and move it back and forth in a direction parallel to the intersection of the plane of the wafer with the plane of the sandpaper. The sandpaper should always be wet to avoid airborne dust, and the edge of the wafer should be carefully cleaned after the sanding is complete, for the same reason.
- I, along with previous operators of this gas bearing, have found that proper cleaning of the rotor and housing will greatly increase the chances of successful operation. The procedure we used was handed down from the Cabrera group. It consists of immersing both the rotor and the housing in acetone and then

in isopropanol, for several minutes each, with minimum delay time between the solvents to avoid the formation of dried-acetone spots. Immediately upon being removed from the isopropanol, all parts should be blown until dry with a clean heat gun (i.e. one that has never been outside the clean hood) set to blow not-very-hot air. This procedure is easy to implement for the rotor, which came with a convenient glass dunking tool. The cleaning of the housing is more tricky, since it requires using the hoist to raise and lower the whole probe into and out of an enormous beaker of solvent. I tend to have a headache for two or three days after the cleaning procedure, due either to stress or (more likely) to sustained acetone inhalation.

- Insertion and removal of the rotor into and out of the housing is done using a homemade vacuum chuck. This is just a clean shop-vac (again, this means one which has never been out of the clean hood) with a brass nozzle made from a kwik-flange connector attached to the end. The nozzle should be gently brought in contact with the drive mass and then the shop-vac turned on. The vacuum is more than sufficient to lift and move the whole rotor. When it has been placed in the right spot, the vacuum can be turned off and the suction will gradually cease.
- The drive mass is attached to the rotor with a dot of Stycast 1266. One feature of this epoxy is that it softens at elevated temperatures, becoming really gummy around 90°C. Therefore, removal of the drive mass from the rotor can be easily and non-destructively accomplished by heating the rotor or drive mass with a heat gun or hotplate, and gently twisting the two pieces with respect to one another. If the drive mass itself contains Stycast 1266 and is likely to be reused, care should be taken to avoid softening that too much. In that case, perhaps the bottom part of the rotor could be heated in a  $\sim 70^\circ\text{C}$  bath of water with a large heat sink resting on the drive mass to keep it relatively cool.
- A substantial practical difficulty of the first design of this probe can be seen by the sharp-eyed in figure 3.2. The four legs of the stainless-steel fiber holder (which contains the fiber and the lens for the interferometer) protrude through

holes in the bearing lid and are glued to the surface of the cantilever wafer. This means that the bearing lid is topologically “captured” and cannot be removed more than a few millimeters from the cantilever wafer. Even more annoyingly, it means that visual alignment of the interferometer’s laser spot to the 100-micron-wide test mass must be performed with the bearing lid in place, inside the probe. This is a task just short of impossible; I have only done it once, and it took rather a lot of time and effort. To avoid having to do it again, and in an effort to make the experiment more modular, I made a much smaller stainless steel fiber holder with legs that rested directly on the glass lid of the cantilever trench. Since the entire holder fits within a single hole on the bearing lid (the legs no longer need to go through separate holes), the lid is no longer “captured” and need not be in place for the alignment. This greatly simplifies the experimental procedure. The simplification may come at some cost, however, since the three data points I have taken seem to indicate that the old (larger) fiber holder design was more robust against thermal misalignments during the cooldown process. This statement is based on the ratio between the DC fringe height at room temperature and at helium temperature, assuming that any reductions in the fringe height are due to thermally-induced misalignment of the interferometer beam.

# Appendix D

## Cryogenic Setup

The experiment is designed to take place at liquid helium temperatures. The initial motivation for running at low temperatures was to reduce thermal noise and thus enhance force sensitivity. Currently, the force sensitivity is limited by vibrational noise rather than thermal noise (this is expected to change when the upgrades discussed in appendix E are implemented), but even so there are important reasons to cool down the experiment. The two most important of these reasons are turbulence in the gas bearing and cantilever quality factor. The flow of helium gas in *all* parts of the gas bearing is turbulent at room temperature [22]; when the experiment is operated close to the boiling point of helium, the flow is laminar everywhere except for the spin-up channels.<sup>1</sup> Laminarity is important because turbulent flow beneath the cantilever shield membrane can be a major source of vibrational noise. The second reason for cryogenic operation is that the cantilever quality factor is only high when the microfabricated cryopump discussed in section 3.6.4 is operational. At room temperature, viscous damping from gas in the sealed cantilever cavity limits the  $Q$  to 10 or less— this severely limits the achievable force sensitivity, and even makes unambiguous detection of the cantilever resonance difficult. There is not a simple way to maintain the tiny cantilever cavity at a very low pressure without using the integrated cryopump, since its immediate environment must be at a relatively high

---

<sup>1</sup>The flow must be non-laminar in the spin-up channels in order to exert the torque necessary to spin the bearing.

pressure due to the exhaust from the gas bearing.

So there are several important reasons for cryogenic operation of the experiment. This appendix discusses the cryogenic apparatus used to cool the probe, and gives some useful numbers and tips for its operation. It will thus be of interest mainly to future users of the experiment, especially if a new dewar is not ordered immediately. Other readers, if they are not entirely imaginary, may wish to skip ahead to the exciting References section.

The dewar used to cool the probe has a liquid nitrogen jacket, a leaky thermal vacuum, and a straight-bore liquid helium space (i.e. no belly). When the probe is cold, the nitrogen jacket runs out entirely in about 36 hours and should be refilled daily—just hook up a nitrogen dewar to the inlet port and wait until liquid comes out the exhaust port. The time this takes will depend on how quickly you are transferring nitrogen; I try to adjust the flow so as to keep the shriek of exhausting nitrogen gas just below the level where it's annoyingly loud. If the nitrogen in the jacket is allowed to run out, the helium boiloff rate will increase markedly. The most unwelcome feature of the nitrogen jacket (besides the mechanical vibrations it produces) is the fact that it is dangerously susceptible to being underpressured. This can occur just after a helium transfer, when upper parts of the dewar are being efficiently cooled by the helium. This cooling can condense some of the nitrogen boiloff and cause the pressure in the nitrogen jacket to drop below atmospheric pressure. This is a problem because it will result in air being sucked into the nitrogen space and freezing in the inlet. There are only two narrow inlets to the jacket space, and it is easy for one or both of them to become plugged with cryodeposits after a relatively short time of being underpressured. Obviously, this is a dangerous situation.<sup>2</sup> The way to avoid it is to keep the jacket constantly overpressured with helium gas whenever underpressures might occur—this is definitely worth the cylinder or two of gas that you will expend on it each week.<sup>3</sup> If you do experience an ice-blocked jacket port, don't panic, but don't go home either. You will need to melt the ice before you can safely leave. You

---

<sup>2</sup>To see why, fill a plastic coke bottle halfway with LN2, tightly seal the lid, and wait 2 minutes. You can use the downtime to look up the relative tensile strengths of plastic and stainless steel.

<sup>3</sup>Even if the regulator is adjusted to a value less than the OPV setpoint, the gas runs out quickly once the LN2 overpressures again.

should **NOT** try to chip the ice out with a screwdriver or similar implement. The ice will be frozen just inside the very delicate bellows that pierce the thermal vacuum and lead into the jacket space. It is apparently not difficult to punch through the side of the bellows while trying to chip out the ice; this would vent the thermal vacuum to air and result in larger and more exciting problems. The right way to melt the ice is to push on it with a hot resistor attached to the end of a wire, while simultaneously blowing room-temperature helium gas directly onto the ice through a narrow tube. This sort of iceblock event happened to me twice in my last few months,<sup>4</sup> so all the necessary equipment including an appropriate resistor-wand and power supply should be lying around near the dewar.

The leaky vacuum jacket on this dewar should be pumped within an inch of its life before every cooldown. If it is not, the air inside it will make an excellent thermal contact between the liquid helium in the bath and the liquid nitrogen in the jacket. This will result in extremely rapid helium boiloff. If the pressure in the vacuum jacket is high (which it will be if it has sat idle for a while), the best procedure is to flush it with nitrogen and pump it down with the Welch 1397 mechanical pump a few times to get rid of as much helium as possible, then to turbopump it for several days. *Important:* the turbopump should be left pumping on this space during the initial cooldown. This is because the fiberglass (G-10?) wall of the liquid helium space seems to be very susceptible to helium leakage down to a certain temperature between 300°K and 4°K. So during the initial cooldown, which is done with a trickle of liquid helium rather than nitrogen, the turbo must bail out all the helium that leaks into the thermal vacuum space. Once the fiberglass gets cold enough, it forms a good barrier to the helium; at that point, the turbo can and should be valved off and disconnected.

The straight-bore liquid helium space can be precooled without liquid nitrogen fairly easily, using a very slow transfer of helium into the liquid space, as long as the above cautions regarding pumping are observed. The helium space currently contains a lead bag that was initially inflated while superconducting in order to

---

<sup>4</sup>To quote one of our nation's great political philosophers: "Fool me once, shame on — shame on you. Fool me — you can't get fooled again."

achieve extremely low flux density. The bag should be removed from the apparatus as soon as possible—it is more likely to produce systematic errors than to offer useful magnetic shielding. Regular transfers of liquid helium into the dewar are relatively straightforward. The exhaust port is connected via a ping-pong-ball meter to the exhaust grille of the room, so that the transfer speed can be monitored. Of course, the level meter provides an even better gauge. I typically set the meter to take a reading every six seconds, and try to maintain the transfer speed in such a way that the reading goes up a tenth of an inch every six seconds (or, put more simply, an inch a minute). At this speed, normal transfers take less than half an hour in total. One thing to watch out for if the lead bag is still in place (which it shouldn't be) is the inevitable pause in the level meter reading as the helium level crests the top of the bag and spends a few minutes filling its interior.

The temperature of the probe is monitored in two places. A CGR thermometer suspended in the exhaust of the gas bearing measures the temperature of the spin flows, and an ordinary carbon resistor embedded in the top of the inner vacuum can (IVC) measures the temperature of that can.

When fully inserted, the top of the outer vacuum can (OVC) is about 41 inches above the bottom of the dewar's liquid helium space. The part of the liquid space that lies below this level holds about 50 liters of helium (roughly 1.3 liters per vertical inch). Above that level, the diameter of the probe decreases to 4 inches. The part of the liquid space between the top of the OVC and the bottom of the first baffle (which is about 65 inches off the bottom) holds about 40 liters of helium, or 1.66 liters per vertical inch. Filling helium above the baffle is probably not worthwhile, so a level of 65 inches above the bottom is considered completely full. The level meter is 60 inches long. This is not quite long enough to measure the entire range of possible levels, but the meter can be raised in its Wilson-seal feedthrough off the bottom of the liquid space so that a maximum reading corresponds roughly to a completely full dewar. Boiloff rates vary somewhat, and can be drastically increased by a combination of excessive exchange gas pressure and operation of the bearing gas line heaters (see next paragraph). When the bearing is not being operated, the dewar tends to boil off roughly 7 liters of helium per day. When the bearing is being constantly operated

without heaters or with heaters that are very well decoupled from the bath, this rate goes up by a factor between 2 and 4. When the bearing is operated with heaters that are well coupled to the bath, it can boil off ten liters in an hour or more.

Currently there seems to be a low-temperature leak into the exchange gas space (the space between the IVC and the OVC). This leak can cause the OVC pressure to creep up by several tens of mtorr per day, and makes it very difficult to heat the bearing without boiling off lots of helium. This is annoying, because heating the bearing can improve the noise and can help reject possible spurious forces from a superconducting brass drive mass (see section 3.4.3). One way to get around this problem is to have a turbopump constantly bailing the OVC space during a measurement run. To avoid vibration problems, the turbo's pumping line must pass through a cement-filled vibration isolator before reaching the dewar. This does keep the pressure down to manageable levels and allows heating of the bearing; however, the OVC leak should be located and fixed for maximally efficient operation.

The entire dewar is currently suspended on spring-feet for vibration isolation. I have not characterized the effect this has on the cantilever noise, so it may or may not be a useful feature. In any case, the feet are relatively easy to add or remove.

# Appendix E

## Future Work

This appendix presents a brief listing of possible future improvements to the apparatus. Again, this is mainly for the delectation of any future users of the experiment that might happen upon these pages.

- **Dewar without liquid nitrogen jacket** — The purchase of a new dewar would substantially reduce the possible sources of mechanical vibration that can excite the cantilever. Also, the old dewar has some problems (mentioned in appendix D) which can inhibit experimental efficiency.
- **In-probe vibration isolation** — It should be relatively simple to add some springs to the bearing support rods. This would help insulate the cantilevers from vibrations in the rest of the probe. Alternatively or additionally, the bearing support platform could be braced against the inner vacuum can with springs to reduce the amplitude of possible pendular vibrations.
- **Insert tungsten drive mass** — A tungsten drive mass, carefully planarized with indium antimonide, would offer a greater density contrast than the brass drive mass currently in the apparatus. A tungsten mass has already been fabricated and filled with InSb. It awaits final planarization with epoxy and deposition of the shield layer and encoder pattern.
- **Acoustically shielded room** — Again, the most important goal currently is

to get rid of unwanted vibrations, especially around 300 Hz. Good acoustic shielding is a very important part of this goal. If an acoustic room cannot be built, solid acoustic curtains hung from the ceiling might do the job.

- **Anchored cantilever wafer** — It is possible that a step as simple as gluing the cantilever wafer to the gas bearing lid at several points would drastically reduce the part of the vibrational noise that is due to shaking of the cantilever wafer by the exhausting bearing gas. The idea would be that the lid, being much thicker and heavier than the wafer, could help anchor it against vibrations. This would have to be done in a way that would take account of the very different thermal expansions of the two pieces— they could, for example, be attached with indium solder (difficult) or short pillars of GE varnish (easy but probably less effective as an anchor). Alternatively, a single large spot of epoxy placed near the cantilever trench might have the desired effect without causing any differential thermal strain.
- **Stiffened shield membrane** — The shield membrane below the cantilevers might benefit from being stiffened against drum-like vibrations. One possible way to achieve this would be to glue a 400  $\mu\text{m}$  test mass to the shield in such a way so as not to disturb the working cantilever. The cryogenic suitability of this idea would need to be tested, of course.
- **New spacer washer** — Replacement of the current four small spacer washers with a single large spacer washer that completely encircles the drive mass could also help stabilize the cantilever wafer against vibration. In addition, this would constrain the exhaust flow from the top inlet of the gas bearing to be farther from the wafer, perhaps minimizing any excitation due to turbulence in that flow.
- **Multiple optical fibers** — If we ever have to re-thread the optical fiber from the teflon feedthrough down to the bearing, it would be easy to put in more than one. Those teflon feedthroughs [53] apparently work just fine with more than one hole drilled in them (discrete rotational symmetry should probably

be maintained, though). Multiple fibers would have several advantages, from better reliability to a possible increase in experimental sensitivity.

- **Thermometer in exhaust of top inlet** — The thermometer currently in the bearing exhaust more directly measures the temperature of the rotor than the temperature of the drive mass. The drive mass temperature is of course a more experimentally relevant parameter, especially if the drive mass superconducts at 7 °K. This would be easy to fix.
- **Real-time data analysis** — With the addition of a second computer running MATLAB and some kind of shared disk or RAID storage, it should be relatively easy to process the data from an experiment immediately, and extract force measurements while the experiment is running. I have done this in a clunky way using my laptop; very little extra programming would be required. This would make the experiment substantially more efficient, and would radically improve the ability of the operator to optimize the experimental parameters for minimum noise. This would, I think, help a lot with the next item:
- **Further exploration of experimental phase space** — Perhaps most important is the need to do further exploration of the parameters of the bearing operation. In a fairly short amount of time I was able to get much better vibration noise performance out of the bearing by tweaking the flow rates. This is important because the sensitivity of the experiment is currently limited by thermal noise. It is very likely that further successful optimizations of bearing parameters await the next experimenter.

# Appendix F

## Catalog of Data Files

This appendix consists of a catalog of the most important data files taken during the preliminary runs of this experiment. Data files were all named in the same way: the date followed by the time (in 24-hr format) that the file was saved (e.g. “07-Dec-2006 15.10.35”). All files are stored in folders named after the date (e.g. “07-Dec-2006”). We have taken about 23GB of data in total. It is all stored on the Frogstar computer; I have also kept a backup copy on a portable hard drive.

Each experimental run began by establishing a set of conditions (temperature, bearing flows, etc.) and starting to spin the drive mass so as to modulate the gravitational force at the resonant frequency of the cantilever. Data were in general taken and saved to disk during this initial spin-up phase; often these initial data files were less than 60 seconds in length. When the drive mass frequency first became resonant (i.e. exactly  $100\times$  less than the cantilever frequency) we would set the data file length to 60 seconds, note the name of the first file saved, and record that as the “start file” for that experimental run. When the run was complete, we would note the name of the last on-resonance file and record that as the “end file” for the run. For experimental runs taken during the night, these would sometimes be in two separate directories since they were taken on different calendar days. The analysis software takes in the names of these two files, loads the data from all files in between, and returns the phase and magnitude of the measured force as described in section 4.1.1. In general, some of the in-between files will be off-resonance; the data from these runs

are of course not counted in the analysis. The tables below list the start file and end file for all the most important data runs, along with a brief comment regarding the nature of the data. The first table contains noise runs, while the second one contains on-resonance data runs.

One important parameter mentioned in the second table is the “fringe direction.” This variable is recorded as either  $\uparrow\uparrow$  or  $\uparrow\downarrow$ , depending on whether a rising interferometer voltage indicates a rising  $z$ -position or a falling  $z$ -position, respectively (the positive  $z$  axis is defined to point away from the center of the earth). This parameter is of critical importance, since it changes the sign of the measured force. Due to operator error, this parameter was unrecorded for the first two data runs, so the results from those runs could be off by  $\pi$  in phase (equivalent to a sign error).

Most of the runs listed in these two tables are discussed in the text of chapter 4. They are presented here mainly for reference, and to render more comprehensible the large amount of stored data from this experiment.

Start & End Files	Comments
08-Oct-2006 15.32.28 → 08-Oct-2006 17.09.56	No spin, cantilever feedback on, pump off, AC on.
10-Oct-2006 21.27.16 → 10-Oct-2006 23.26.43	No spin, cantilever FB off, pump off, AC on.
11-Oct-2006 09.24.20 → 11-Oct-2006 10.36.44	No spin, cantilever FB off, pump off, AC on.
11-Oct-2006 18.18.48 → 11-Oct-2006 18.38.27	No spin, cantilever FB off, pump on, AC on.
11-Oct-2006 20.19.08 → 11-Oct-2006 21.16.20	0.6 Hz spin, cantilever FB off, pump on, AC on.
11-Oct-2006 21.28.37 → 11-Oct-2006 21.35.10	Top gas flow only, cantilever FB off, pump on, AC on.
12-Oct-2006 09.23.45 → 12-Oct-2006 10.41.39	No spin, cantilever FB off, pump off, AC off.
12-Oct-2006 11.13.39 → 12-Oct-2006 12.36.59	No spin, cantilever FB off, pump off, AC on.
16-Oct-2006 21.07.57 → 16-Oct-2006 22.03.58	No spin, cantilever FB on, pump off, AC on, 20-hr-old LN2 jacket.
16-Oct-2006 22.14.33 → 16-Oct-2006 22.59.22	No spin, cantilever FB on, pump on, AC on, 20-hr-old LN2 jacket.
16-Oct-2006 23.09.05 → 16-Oct-2006 23.40.28	Top gas flow at 320 sccm, FB on, pump on, AC on, 20-hr-old LN2.
16-Oct-2006 23.45.15 → 17-Oct-2006 00.17.59	Top gas flow at 160 sccm, FB on, pump on, AC on, 20-hr-old LN2.
17-Oct-2006 01.05.28 → 17-Oct-2006 01.34.03	0.75 Hz spin, FB on, AC on. Top flow 120 sccm.
24-Oct-2006 20.07.17 → 24-Oct-2006 21.19.50	2.95 Hz spin, FB on, AC on. Top flow 88 sccm. LN2 full.

Table F.1: Catalog of important noise data files taken during the preliminary runs of the experiment. The bearing was not operated on resonance for any of these files.

Start & End Files	Comments
14-Oct-2006 23.45.44 → 15-Oct-2006 03.09.14	CW spin. Measured $z$ -distance is 13 $\mu\text{m}$ . Top flow 360 sccm, bottom flow 320 sccm. First data!
17-Oct-2006 03.03.22 → 17-Oct-2006 05.19.37	CW spin. Top/bottom flow 120/200 sccm.
24-Oct-2006 00.07.52 → 24-Oct-2006 04.24.15	CW spin, fringe direction $\uparrow\uparrow$ . Top/bottom flow 88/160 sccm.
29-Oct-2006 16.49.40 → 29-Oct-2006 17.43.14	CCW spin, $\uparrow\uparrow$ . Top/bottom flow 120/160 sccm.
17-Nov-2006 23.37.59 → 18-Nov-2006 01.10.45	CW spin, $\uparrow\downarrow$ . Top/bot flow 80/144 sccm. Bearing heated to 8.4°K. Fast boiloff. Spin feedback losing lock frequently.
19-Nov-2006 16.03.19 → 19-Nov-2006 21.52.48	CW spin, $\uparrow\uparrow$ . Top/bot flow 96/192 sccm. Bearing at 4.2°K. Measured $z$ -distance is 6 $\mu\text{m}$ (very small).
22-Nov-2006 22.28.56 → 23-Nov-2006 01.14.33	CCW spin, $\uparrow\uparrow$ . Top/bot flow 60/192 sccm. Bearing at 4.2°K.
23-Nov-2006 02.54.25 → 23-Nov-2006 05.37.55	CCW spin, $\uparrow\uparrow$ . Top/bot flow 32/72 sccm. Bearing heated to 9.6°K. Turbo bailing OVC to keep boiloff reasonable. Thanksgiving day.
25-Nov-2006 21.01.27 → 25-Nov-2006 23.05.20	CW spin, $\uparrow\uparrow$ . Top/bot flow 22/36 sccm. Bearing heated to 15°K. Turbo bailing OVC.
29-Nov-2006 21.17.04 → 29-Nov-2006 23.43.48	CW spin, $\uparrow\uparrow$ . Top/bot flow 34/50 sccm. Bearing at 8.4°K. Turbo bailing OVC. Very nice smooth run.
04-Dec-2006 23.31.31 → 05-Dec-2006 02.36.45	CW spin, $\uparrow\uparrow$ . Top/bot flow 34/96 sccm. Bearing at 8.4°K. Turbo bailing OVC. $z$ -distance measured to be 19 $\mu\text{m}$ .
07-Dec-2006 16.49.01 → 07-Dec-2006 17.39.01	CW spin, $\uparrow\uparrow$ . Top/bot flow: 40/56 sccm. Bearing at 9°K. Bailing OVC. $z$ -distance is 18 $\mu\text{m}$ .
07-Dec-2006 18.06.27 → 07-Dec-2006 19.01.15	CCW spin, $\uparrow\uparrow$ . Top/bot flow: 40/56 sccm. Bearing at 9°K. Bailing OVC. $z$ -distance is 18 $\mu\text{m}$ .
07-Dec-2006 19.06.00 → 07-Dec-2006 19.51.46	CCW spin, $\uparrow\uparrow$ . Top/bot flows: 40/80 sccm. Bearing at 9°K. Bailing OVC. $z$ -distance is 13 $\mu\text{m}$ .
07-Dec-2006 20.20.51 → 07-Dec-2006 21.06.18	CW spin, $\uparrow\uparrow$ . Top/bot flows: 40/80 sccm. Bearing at 9°K. Bailing OVC. $z$ -distance is 13 $\mu\text{m}$ .

Table F.2: Catalog of important data files taken during the preliminary runs of the experiment with the bearing spinning at  $0.01\times$  the cantilever's resonant frequency.

# Bibliography

- [1] N. Arkani-Hamed, S. Dimopoulos, and G. Dvali, “The hierarchy problem and new dimensions at a millimeter,” *Phys. Lett. B*, vol. 429, p. 263, 1998.
- [2] N. Arkani-Hamed, S. Dimopoulos, and G. Dvali, “Phenomenology, astrophysics, and cosmology of theories with submillimeter dimensions and tev scale quantum gravity,” *Phys. Rev. D*, vol. 59, p. 086004, 1999.
- [3] J. Chiaverini, S. Smullin, A. Geraci, D. Weld, and A. Kapitulnik, “New experimental constraints on non-Newtonian forces below 100  $\mu\text{m}$ ,” *Phys. Rev. Lett.*, vol. 90, no. 15, 2003.
- [4] S. Beane, “On the importance of testing gravity at distances less than 1cm,” *Gen. Rel. Grav.*, vol. 29, p. 945, 1997.
- [5] R. Sundrum, “Towards an effective particle-string resolution of the cosmological constant problem,” *J. High Energy Phys.*, 1999.
- [6] E. G. Adelberger, B. R. Heckel, and A. E. Nelson, “Tests of the gravitational inverse-square law,” *Annu. Rev. Nucl. Part. Sci.*, vol. 53, Jul 2003, hep-ph/0307284.
- [7] D. B. Kaplan and M. B. Wise, “Couplings of a light dilaton and violations of the equivalence principle,” *J. High Energy Phys.*, vol. 08, p. 037, 2000.
- [8] S. J. Smullin, *A test of Newtonian gravity at the 25 micron length scale*. PhD thesis, Stanford University, 2005.

- [9] C. D. Hoyle, D. J. Kapner, B. R. Heckel, E. G. Adelberger, J. H. Gundlach, U. Schmidt, and H. E. Swanson, “Submillimeter tests of the gravitational inverse-square law,” *Phys. Rev. D*, vol. 70, p. 042004, 2004.
- [10] J. C. Long, H. W. Chan, A. B. Churnside, E. A. Gulbis, M. C. M. Varney, and J. C. Price, “Upper limits to submillimetre-range forces from extra space-time dimensions,” *Nature*, vol. 421, p. 922, 2003.
- [11] R. S. Decca, D. Lopez, H. Chan, E. Fischbach, D. Krause, and C. Jamell, “Constraining new forces in the casimir regime using the isoelectronic technique,” *Phys. Rev. Lett.*, Jun 2005, hep-ph/0502025.
- [12] M. Bordag, B. Geyer, G. L. Klimchitskaya, and V. M. Mostepanenko, “Constraints for hypothetical interactions from a recent demonstration of the Casimir force and some possible improvements,” *Phys. Rev. D*, vol. 58, p. 075003, 1998.
- [13] H. Cavendish, “Experiments to determine the density of the earth,” *Philos. Trans. R. Soc. London*, vol. 88, p. 469, 1798.
- [14] T. W. Murphy, E. G. Adelberger, J. D. Strasburg, C. W. Stubbs, and K. Nordtvedt, “Testing gravity via next-generation lunar laser-ranging,” *Nuc. Phys. B - Proceedings Supplements*, vol. 134, pp. 155–162, September 2004.
- [15] J. K. Hoskins, R. D. Newman, R. Spero, and J. Schultz, “Experimental tests of the gravitational inverse-square law for mass separations from 2 to 105 cm,” *Phys. Rev. D*, vol. 32, pp. 3084–3095, 1985.
- [16] V. P. Mitrofanov and O. I. Ponomareva, “Experimental check of the law of gravitation at small distances (in russian),” *JETP*, vol. 94, pp. 16–22, 1988.
- [17] S. K. Lamoreaux, “Demonstration of the Casimir force in the 0.6 to 6  $\mu\text{m}$  range,” *Phys. Rev. Lett.*, vol. 78, p. 5, 1997.
- [18] U. Mohideen and A. Roy, “Precision measurement of the casimir force from 0.1 to 0.9  $\mu\text{m}$ ,” *Phys. Rev. Lett.*, vol. 81, p. 4549, 1998.

- [19] S. J. Smullin, A. A. Geraci, D. M. Weld, J. Chiaverini, S. Holmes, and A. Kapitulnik, “Constraints on yukawa-typ deviations from newtonian gravity at 20 microns,” *Phys. Rev. D*, vol. 72, p. 122001, 2005.
- [20] J. Chiaverini, *Small force detection using microcantilevers: Search for sub-millimeter-range deviation from Newtonian gravity*. PhD thesis, Stanford University, 2002.
- [21] S. Dimopoulos and A. A. Geraci, “Probing submicron forces by interferometry of Bose-Einstein condensed atoms,” *Phys. Rev. D*, vol. 68, p. 124021, 2003.
- [22] S. B. Felch, *A precise determination of  $h/m_e$  using a rotating, superconducting ring*. PhD thesis, Stanford University, 1985.
- [23] J. Tate, *A precise determination of the mass of a cooper pair of electrons in superconducting niobium*. PhD thesis, Stanford University, 1988.
- [24] S. B. Felch, J. Tate, B. Cabrera, and J. T. Anderson, “Precise determination of  $h/m_e$  using a rotating, superconducting ring,” *Phys. Rev. B*, vol. 31, no. 11, pp. 7006–7011, 1985.
- [25] J. Tate, B. Cabrera, S. B. Felch, and J. T. Anderson, “Precise determination of the cooper-pair mass,” *Phys. Rev. Lett.*, vol. 62, pp. 845–848, 1989.
- [26] J. Tate, S. B. Felch, and B. Cabrera, “Determination of the cooper-pair mass in niobium,” *Phys. Rev. B*, vol. 42, pp. 7885–7893, 1990.
- [27] A. Shimamoto and K. Tanaka, “Geometrical analysis of an optical fiber bundle displacement sensor,” *Appl. Opt.*, vol. 35, pp. 6767–6774, Dec. 1996.
- [28] W. O. Hamilton, D. B. Greene, and D. E. Davidson, “Thermal expansion of epoxies between 2 and 300 °k,” *Rev. Sci. Instr.*, vol. 39, no. 5, pp. 645–648, 1968.
- [29] R. J. Corruccini and J. J. Gniewek, “Thermal expansion of technical solids at low temperatures.” National Bureau of Standards, Monograph 29, 1961.

- [30] H. B. G. Casimir, "On the attraction between two perfectly conducting plates," *Proc. K. Ned. Adak. Wet.*, vol. 51, p. 793, 1948.
- [31] J. G. Siekman, "On the ultimate thickness of an epoxy resin bond layer," *J. Phys. D.*, vol. 13, pp. 893–6, 1980.
- [32] S. Smullin, A. Geraci, D. Weld, and A. Kapitulnik, "Testing gravity at short distances," in *SLAC Summer Institute on Particle Physics*, Aug 2004.
- [33] N. V. Mandich, "Pulse and pulse-reverse electroplating," *Metal Finishing*, vol. 97, no. 1, pp. 375–380, 1999.
- [34] R. Maboudian and R. T. Howe, "Critical review: Adhesion in surface micromachined structures," *J. Vac. Sci. Technol. B*, vol. 15, pp. 1–20, 1997.
- [35] D. Rugar, H. J. Mamin, and P. Guethner, "Improved fiber-optic interferometer for atomic force microscopy," *Appl. Phys. Lett.*, vol. 55, no. 25, p. 2588, 1989.
- [36] K. Yasumura, *Energy Dissipation Mechanisms in Microcantilever Oscillators with Applications to the Detection of Small Forces*. PhD thesis, Stanford University, 2000.
- [37] C. C. Liu, Y. K. Lin, M. P. Houn, and Y. H. Wang, "The microstructure investigation of flip-chip laser diode bonding on silicon substrate by using indium-gold solder," *IEEE Trans. On Components and Packaging Technologies*, vol. 26, no. 3, pp. 635–642, 2003.
- [38] J. P. Hobson, "Cryopumping," *J. Vac. Sci. Technol.*, vol. 10, no. 1, pp. 73–79, 1973.
- [39] D. M. Weld and A. Kapitulnik, "Feedback control and characterization of a microcantilever using optical radiation pressure," *App. Phys. Lett.*, vol. 89, no. 164102, 2006.
- [40] J. Tamayo, A. D. L. Humphris, and M. J. Miles, "Piconewton regime dynamic force microscopy in liquid," *Appl. Phys. Lett.*, vol. 77, no. 4, p. 582, 2000.

- [41] J. Mertz, O. Marti, and J. Mlynek, "Regulation of a microcantilever response by force feedback," *Appl. Phys. Lett.*, vol. 62, p. 2344, 1993.
- [42] T. Aoki, M. Hiroshima, K. Kitamura, M. Tokunaga, and T. Yanagida, "Non-contact scanning probe microscopy with sub-piconewton force sensitivity," *Ultramicroscopy*, vol. 70, p. 45, 1997.
- [43] O. Marti, A. Ruf, M. Hipp, H. Bielefeldt, J. Colchero, and J. Mlynek, "Mechanical and thermal effects of laser irradiation on force microscope cantilevers," *Ultramicroscopy*, vol. 42-44, p. 345, 1992.
- [44] F. L. Degertekin, B. Hadimioglu, T. Sulchek, and C. F. Quate, "Actuation and characterization of atomic force microscope cantilevers in fluid by acoustic radiation pressure," *Appl. Phys. Lett.*, vol. 78, no. 11, p. 1628, 2001.
- [45] P. F. Cohadon, A. Heidmann, and M. Pinard, "Cooling of a mirror by radiation pressure," *Phys. Rev. Lett.*, vol. 83, no. 16, p. 3174, 1999.
- [46] A. Passian and A. Wig, "Knudsen forces on microcantilevers," *J. Appl. Phys.*, vol. 92, no. 10, p. 6326, 2002.
- [47] J. E. Sader, I. Larson, P. Mulvaney, and L. White, "Method for the calibration of atomic force microscope cantilevers," *Rev. Sci. Instrum.*, vol. 66, p. 3789, 1995.
- [48] J. W. Cooley and J. W. Tukey, "An algorithm for the machine computation of the complex fourier series," *Mathematics of Computation*, vol. 19, pp. 297-301, 1965.
- [49] R. A. Matula, "Electrical resistivity of copper, gold, palladium, and silver," *J. Phys. Chem. Ref. Data*, vol. 8, no. 4, pp. 1147-1298, 1979.
- [50] T. Geballe and W. Giaque, "The heat capacity and entropy of gold from 15 to 300°k," *J. Amer. Chem. Soc.*, vol. 74, p. 2368, 1952.
- [51] D. Martin, "Specific heats of copper, silver and gold below 30 °k," *Phys. Rev.*, vol. 141, no. 2, p. 576, 1966.

- [52] B. Zink and F. Hellmann, "Specific heat and thermal conductivity of low-stress amorphous  $\text{Si}_3\text{N}_4$  membranes," *Sol. State Comm.*, vol. 129, pp. 199–204, 2004.
- [53] E. R. I. Abraham and E. A. Cornell, "Teflon feedthrough for coupling optical fibers into ultrahigh vacuum systems," *Applied Optics*, vol. 37, no. 10, pp. 1762–1763, 1998.